
Validation Methods for Industrial Machine Learning Problems

Trabajo Fin de Grado

Grado en Ingeniería Aeroespacial

Escuela Técnica Superior de Ingeniería
Aeronáutica y del Espacio

Universidad Politécnica de Madrid



Autor: Pablo Yeste Blesa

Tutor académico: Javier de Vicente Buendía

Marzo 2024

Resumen.

Las matrices de transición de estado constituyen una herramienta muy útil para el análisis de movimiento relativo entre vehículos espaciales. El hecho de ser formas lineales y además de soluciones semianalíticas se plasma en las siguientes ventajas:

- a. Dan lugar a un coste computacional razonable, sin comprometer en exceso la precisión numérica.
- b. Su carácter analítico permite extraer conclusiones interesantes sobre el funcionamiento del sistema.

Los modelos linealizados generalmente permiten obtener mejores resultados mediante una mejor modelización del sistema. En el caso de la dinámica espacial relativa, el análisis y la implementación de perturbaciones son vitales, al ser la parte normalmente despreciada y más difícil de modelar del problema. Uno de los efectos más comúnmente analizados en el caso de órbitas terrestres es el campo gravitatorio no esférico, debido esencialmente a ser el más relevante en magnitud en órbitas bajas. La expansión del potencial gravitatorio en armónicos esféricos permite obtener una aproximación ciertamente precisa del mismo, aunque, en función de cómo se aborde, su manejo analítico puede resultar altamente complejo.

Este trabajo trata de proporcionar una visión general sobre la dinámica relativa linealizada entre vehículos espaciales, analizando modelos progresivamente más complejos y precisos, así como introduciendo teorías de perturbaciones – cuyo uso último es la construcción de modelos para dinámica relativa. El concepto de seguridad orbital también es abordado, debido a su vital importancia en el movimiento relativo en cercanía (p.ej., vuelo en formación, *rendez-vous*...).

Abstract.

State Transition Matrices are a very useful and widely used tool for the analysis of linearised spacecraft relative motion. Their closed-form and linear characters bear two main advantages:

- a. A quite good computational cost is achieved, without compromising accuracy more than desired.
- b. Highly insightful knowledge about the dynamics of the system is obtained.

Linearised models return better outcomes the truer-to-life they are. With this in mind, the analysis and implementation of perturbations play an important role, as it is one of the main ways to achieve high accuracy. Earth's non-spherical gravity field is by far the most usually analysed perturbation in Earth orbits, as it has generally the biggest effect (in value). The way in which this perturbation is approached allows for a better or worse reliability of the results.

This thesis intends to provide an outlook on linearised relative motion, evaluating increasingly more complex motion models, and also analysing perturbation theories, whose ulterior use is relative motion. Orbit safety is also recurrently tackled, due to the vital role it plays in close-proximity relative motion.

Contents

Resumen.	iii
Abstract.	v
Nomenclature	ix
Introduction.	xix
1 The Validation Loop	1
1.1 Introduction	1
1.1.1 Case of study	1
1.1.2 Applicability	2
1.1.3 Overview	5
1.2 Train-test split	7
1.2.1 Preliminaries	7
1.2.2 Validation loop for the train-test split	8
1.3 Global error quantification	20
1.4 Distributed error quantification.	22
1.5 Distributed error quantification: conditioning the error distribution on the input space	34
1.5.1 Visualization of error as a function of categorical (discrete) input variables	35
1.5.2 Bias detection and quantification (1D)	37
1.5.3 Bias detection and quantification (2D)	41
1.5.4 Visualization of error as a function of numerical (continuous) input variables	43
1.5.5 Bias detection and quantification	43
1.6 Distributed error quantification: conditioning the error distribution on the output space	48
1.7 Uncertainty model	56
1.7.1 Global uncertainty model based on $P(E)$	57
1.7.2 Local uncertainty model based on $P(E \mathbf{Y})$	59
1.7.3 Local uncertainty model based on $P(E \mathbf{X})$	62

1.7.4	Full uncertainty model (FUM)	67
1.8	Las movidas de Rodrigo	72
1.8.1	Concept: System dynamics.	72
1.8.2	Applications of STMs in celestial mechanics.	74
2	Conclusions and research outlook.	79
A	Absolute and relative orbital element sets.	81
A.1	Introduction.	81
A.2	Absolute element sets.	82
A.2.1	Workflow for transformations between absolute element sets.	82
A.2.2	Element sets.	82
A.3	Relative sets.	86
A.3.1	Workflow for transformations between ROEs.	87
A.3.2	Element sets.	89

Nomenclature

Acronyms

BF	Body-Fixed frame
CR3BP	Circular Restricted Three Body Problem
CW	Clohessy-Wiltshire
ECEF	Earth-Centered Earth-Fixed frame
ECI	Earth-Centered Inertial frame
GA	Gim-Alfriend
HCW	Hill/Clohessy-Wiltshire
Hi-Fi	High-Fidelity
ICs	Initial Conditions
IP	In-plane
IVP	Initial Value Problem
KOE	Keplerian OEs vector
LEO	Low Earth Orbit
LVLH	Local-Vertical, Local-Horizontal frame
MOD	Mean-of-Date frame
NSG	Non-spherical gravity
ODE	Ordinary Differential Equation
OEs	Orbital Elements
OOP	Out-of-plane
PBF	Pseudo-Body-Fixed frame
RTN	Radial-Transverse-Normal frame
SRP	Solar Radiation Pressure
STM	State Transition Matrix
TOD	True-of-Date frame
YA	Yamanaka-Ankersen

General

μ	Gravitational parameter of a celestial body	$\left[\frac{m^3}{s^2} \right]$
\underline{a}_i	Acceleration on body i	$\left[\frac{m}{s^2} \right]$
\underline{F}_i	Force on body i	[N]
a_e	Equatorial radius of a celestial body	[m]
m_i	Mass of body i	[kg]
Mathematics		
$\Delta\bullet$	Variation or increment of a quantity	
$\delta\bullet$	Relative quantity (deputy's minus chief's value)	
Λ	Real or complex eigenvalue matrix	
\mathbb{I}	Identity matrix	
$\Phi(t, t_0)$	State Transition Matrix	
J	Jordan form	
V	Real or complex eigenvector matrix	
\mathbf{A}	System's matrix of a system of ODEs	
f	Dynamics function of a system	
$\underline{u}, \underline{y}$	State vector of a system of ODEs	
Orbital elements		
λ	Mean argument of latitude	[rad]
Ω	Right Ascension of Ascending Node	[rad], [deg]
ω	Argument of periapsis	[rad], [deg]
θ	True anomaly	[rad], [deg]
a	Semimajor axis	[m]
E	Eccentric anomaly	[rad]
e	Eccentricity	[---]
F	Eccentric argument of latitude	[rad]
i	Inclination	[rad], [deg]
M	Mean anomaly	[rad]

u	True argument of latitude	$[rad], [deg]$	Subindices
Perturbations			
\overline{OE}	Mean orbital element vector	\bullet_0	Variable at $t = t_0$
\underline{OE}	Osculating orbital element vector	\bullet_C	Variable from the chief spacecraft
ε	Small parameter	\bullet_D	Variable from the deputy spacecraft
H	Hamiltonian of the system	$[- - -]$	
K	Modified Hamiltonian of the system	$ _i$	Expressed in frame i
Useful expressions			
p_i, P_i	Generalized momentum (original or transformed)	$\eta = \sqrt{1 - e^2}$	$[- - -]$
q_i, Q_i	Generalized coordinate (original or transformed)	ϕ, λ	Geodetic latitude and longitude $[rad], [deg]$
R	Disturbing function	$\rho = 1 + e \cos \theta$	$[- - -]$
S, W	Generating function of the transformation	h	Orbit altitude or orbit momentum $[m]$ or $\left[\frac{m^2}{s} \right]$

List of Figures

1.1	Surrogate model pipeline	2
1.2	Smallest cube enclosing a set of 20 randomly generated points in a 3-dimensional euclidean space.	5
1.3	Convex hull enclosing the set of Figure 1.2. The convex hull's volume is always smaller than or equal to the volume of the hypercube.	5
1.4	Validation pipeline	6
1.5	Location of the train-test split assessment in the overall validation pipeline . . .	7
1.6	Input [numeric] variables distributions double histogram. Only the first four input variables have been plotted.	17
1.7	Input categorical variables distributions double histograms	18
1.8	Output variables distributions double histograms	18
1.9	Requirements of the geometrical analysis	19
1.10	Scatter plot of ground true (x axis) against predicted values (y axis) of output variable "RF Net Tension", with the correspondent R^2 coefficient. In this case, $R^2 = 1,000$ indicates a perfect fit of predicted to ground true values. Mismatches due to underestimating failure risk are labelled in red, while those due to overestimating failure risk are labelled in blue. Similar graphs can be computed for every pair $\{y_j, \hat{y}_j\}$ of features in the output variables $\mathbf{Y} = \{y_1, y_2, \dots, y_m\}$. Plots for the rest of the six output variables of MS-S18 show analogous results.	21
1.11	Location of ?? in the validation pipeline.	22
1.12	Double histogram depicting ground true values and model's predictions for the six output variables of MS-18.	24
1.13	Empirical residue distribution sampled from the test set, for each of the six output variables of MS-S18. x -axis limits have been truncated to $\mu \pm 3\sigma$, where the most part of the error lies. Histograms have been appropriately binned for a correct visualization.	26
1.14	Cumulative error distributions corresponding to the PDFs showed (as binned histograms) in Figure 1.13.	26

1.15 Graphical comparison of the p-values resulting from the K-S test for the MS-18 data.	28
1.16 (Binned) histograms depicting the distribution of the variable $z = \gamma + \sinh \frac{e-\xi}{\lambda}$, where $e \sim JohnsonSU(\gamma, \delta, \xi, \lambda)$ is the sampled residue. It can be shown that z converges to a normal distribution[26].	28
1.17 Box diagram showing the relative position of section 1.5 in the complete validation pipeline.	34
1.18 Box and whisker plots depicting the residue conditioned to two different categorical variables. Figure 1.18(a): "Frame". Figure 1.18(b): "Stringer". Clearly, outliers can be appreciated in both cases ("Fr69-Fr70" in Figure 1.18(a), and various stringers in Figure 1.18(b)).	36
1.19 Quantification of linear trend for input categorical variables "Stringer" (left) and "Frame" (right). Variables have been numerically encoded following a logical order (<i>e.g.</i> in the right image, six integers in the x axis represent the six possible values of variable Frame). The residue of output variable "RF Net Tension" has been plotted against the categorical variable (y axis). In this case, no linear trend is appreciated in neither of the two input variables (no bias present).	41
1.20 Scatter plots of residue against a particular numerical input variable. Left: Input var. FU.0420.26. A linear trend is appreciated, suggesting the model makes worse predictions as input load "FU.0420.26" is larger. Right: input var. FU.0420.25. No linear trend is appreciated, although severe heteroscedasticity can be observed. Note the vertical bar arrangement, showing particular input loads for which dispersion is unusually large. In view of the former results, the engineer may decide to investigate the underlying causes both for the linear trend in the left and for heteroscedasticity on the right. With the information, model and data boosting may be performed. More training data could be decided to be sampled in the range of [20000, 60000] of FU.0420.26, for instance, and some regularization technique could be tried for the loss function in order to penalise inputs triggering high variance observed in the right.	43
1.21 Relative position of section 1.6 in the complete validation pipeline.	48

1.22 Goodness of fit of the error distribution (test set previously filtered) to some parametrised distributions. The test is performed individually for the output variables (Reserve Factors) displayed on top of each image. The goodness of fit is assessed with a 1-variable K-S test. The test set is filtered using the x axis, rejecting every point whose output \hat{y} is larger than x . If the p-value resulting from the K-S test in the filtered test set is greater than 0.05, the vertical slice at position x is labelled green (red if $p\text{-value} < 0.05$, grey if less than a threshold number of points –namely, 30– are present in the filtered test set).	50
1.23 Line plot of the p -value from the true-predicted distributions under a 2 sample K-S test. Distribution similarity is rejected if p -value < 0.05	52
1.24 Violin plots showing the absolute value residue for every bin.	53
1.25 Sliced-bar with p-values from the binned error under a K-S test to assess the goodness of fit to several parametrised distributions.	54
1.26 Global Uncertainty Model: error coverage. The coverage is higher than 95% for both output variables –for convenience just two output variables are depicted– what means the calibration criteria is successfully met.	59
1.27 Local Uncertainty Model based on $P(E \mathbf{Y})$: Scatter plot of the residue as a function of the predicted output \hat{y} , for output variables "RF Pure Compression" and "RF Shear Panel Failure".	60
1.28 Local Uncertainty Model based on $P(E \mathbf{Y})$: Violin plots of the residue, for binned output variables "RF Pure Compression" and "RF Shear Panel Failure".	60
1.29 LOUM coverage in the validation set. For both output variables coverage is above the minimum 95% threshold.	62
1.30 LIUM: Scatter plot of the residue of "RF Forced Crippling" as a function of the input x (left: x is "FU.0410.16". Right: x is "FU.0410.24").	63
1.31 Violin plots showing the residue of output variable "RF Forced Crippling". (a): Numerical inputs (binned). (b) and (c): categorical inputs.	64
1.32 LIUM coverage on the evaluation set. Residue of the output variable "RF Forced Crippling". The grey area represents the uncertainty CI calculated by the LIUM for the corresponding bin.	66

1.33 Conceptual visualization of FUM as a conservative merge between GUM (whose bootstrap interval [P2.5,P97.5] is represented by the two straight horizontal lines), LOUM and LIUM (whose bootstrap intervals [P2.5,P97.5] are represented indistinctively by the red and blue curves).	68
1.34 Covariance ellipsoid evolution along a radial hop.	76
A.1 Workflow for transforming between two arbitrary absolute element sets.	82
A.2 Frame rotation from inertial to perifocal frame.	83
A.3 Workflow for transforming any relative set into KOE.	88
A.4 Workflow for transforming RKOE into any other set.	89
A.5 Relative eccentricity & inclination vectors.	90

List of Tables

1.1	Output of algorithm 1	12
1.2	Voxel reference table	12
1.3	Points outside voxel hypercube	14
1.4	<code>reqs_results_table</code> . The first and the last requirements compare absolute figures of points at some isolation level with the overall number of points. Whereas the second and third requirements compare the difference in number of points between two consecutive levels with the total number of points.	14
1.5	P-values of the input variables. The test performed is a 2-sample Kolmogorov-Smirnov or a 2-sample χ^2 test, depending on the data being numerical (first 19 rows) or categorical ("dp", "Frame" and "Stringer").	16
1.6	P-values of the output variables distributions	17
1.7	Resulting p -values from the 2-sample K-S test of goodness of fit between ground true (\mathbf{Y}) and predicted ($\hat{\mathbf{Y}}$) distributions. The null hypothesis H_0 that both distributions conform is rejected if the p -value is smaller than 0.05.	25
1.8	P-values of the K-S test comparing the empirical sample of $P(e)$ to the theoretical distributions indicated in each column. The null hypothesis H_0 (the empirical distribution has been sampled from the one figuring in a given column) is rejected when $p - \text{value} < 0.05$	27
1.9	Outlier detection taking $e \sim JohnsonSU$ as H_0 . N.B. for this table the usual requirements for classifying a point as an outlier ($z \in \sigma \pm 3\mu$ for the z-score and significance $1 - a \geq 95\%$ for the gESD) have been softened here for illustration purposes to $z \in \sigma \pm 1.2\mu$ and $a = 0.45$ for both tests, respectively.	29
1.10	Summary of bootstrapped error statistics. For the median, the Wilson-score[29] is used for computing the confidence interval.	32
1.11	Bootstrapped percentiles (1 st , 5 th , 10 th , 90 th , 95 th and 99 th) of the residue distribution, calculated with a 95% confidence interval using Wilson-score.	33

1.12 P-values results from the one-way ANOVA test. The red labelled cells show that variable "dp" shows bias for the residual distribution of "RF Net Tension", as well as variable "Frame" for the residual distribution of "RF Forced Crippling" and variable "Stringer" for the residual distributions of "RF Net Tension" and "RF Pure Compression". For the rest of the table, p-values greater than 0.05 indicate that H_0 cannot be rejected with a statistical confidence of at least 95%.	38
1.13 Z-score results for biased categorical variables. One table is generated for each pair biased categorical input variable-output variable.	39
1.14 2D bias quantification: Results from mean and variance z-score tests on biased Stringer-Frame input pairs (bias detection has been performed through 1-way ANOVA). For the input value combinations showed in the columns, either mean or variance (or both) show bias (weak: $z\text{-score} < 3$. Strong: $z\text{-score} > 3$). For the combination of Frame Fr67-Fr69 and Stringer Str07, there are not enough test points to compute the z -score variance test.	42
1.15 Bias detection and quantification on numerical input variables (the results for just five input variables are shown here – in columns–): P-value (statistical significance of the hypothesis that the variable is biased), Pearson coefficient, and slope of the best linear fit are shown in the first three rows. The last row shows the message "Biased" in case the p -value > 0.05 , "NO" otherwise. Data from this table corresponds to residue of the output variable "RF Column Buckling". Analogous tables exist for the rest of the output variables.	44
1.16 1-way ANOVA test results (p-values) for binned numerical input variables. For the output variable "RF Forced Crippling", bias is found in the input variables "FU.0420.25" and "FU.0430.25". Similarly, for the output variable "RF Net Tension", bias is found in the input variable "FU.0430.15".	45
1.17 Bias quantification in binned FU.0430.15 input variable. Columns represents bins showing bias. The same quantification methods employed for categorical variables (z -score for mean and variance outlier detection) have been used.	46
1.18 Summary of binned input variables bias quantification after binning the numerical variables and performing one-way ANOVA and z -score tests to every bin.	46

1.19 Binnarization of the test set. The test set has been divided into ten bins according to output values. Extremes of the six intervals –one for each Reserve Factor– defining the bins are shown below.	51
1.20 Global Uncertainty Model: Confidence Interval (mean and extremes) for output variables "RF Forced Crippling" (left) and "RF Column Buckling" (right). Header showing $[y_{min}, y_{max}]$ in the calibration set.	58
1.21 Global Uncertainty Model. The six confidence intervals (bootstrapped) defining the GUM alongside their coverage –in the calibration set– are showed.	58
1.22 Local Output Uncertainty Model: Bootstrapped CIs for each of the ten bins into which the output variable "RF Forced Crippling" has been binned. The mean of each CI is also given, as well as the bin extrema $[\hat{y}_{min}, \hat{y}_{max}]$ for every bin (in the first row).	61
1.23 LOUM coverage. Coverage in the validation set is displayed in the first row, whereas the coverage bootstrapped CIs are displayed in the second row.	62
1.24 LIUM: Bootstrapped CIs for binned input variable "FU.0430.26" (bins' extrema displayed as column names). Residue corresponds to output variable "RF Shear Panel Failure".	65
1.25 LIUM: Bootstrapped CIs for categorical input variable "dp" (possible values that the variable can take are displayed as column names). Residue corresponds to "RF Shear Panel Failure" output variable.	65
1.26 Output of algorithm 1: <code>reqs_results</code> table	70
1.27 Voxel reference table. Lorem ipsum dolor sit amet, consectetur adipisciing elit.	71

Introduction.

In recent years, artificial neural networks^[1] have become ubiquitous across industries, fundamentally reshaping operations and decision-making processes. Their integration into various sectors has heralded a new era of innovation and efficiency. From optimizing flight trajectories^[2] to enhancing predictive maintenance^[3–5], artificial neural networks have emerged as indispensable tools, enabling organizations to unlock insights and drive transformative outcomes. As the aerospace sector embraces this technological revolution, the adoption of neural networks underscores a strategic imperative to harness the power of machine learning in pursuit of greater precision, reliability, and safety. Particularly in this industry, where precision, reliability, and safety are paramount, the integration of ML models presents both tremendous opportunities and formidable challenges. As the demand for advanced predictive analytics and automation escalates, so too does the necessity for rigorous statistical validation methodologies. The burgeoning reliance on ML algorithms for critical decision-making processes necessitates a paradigm shift towards comprehensive validation pipelines. Amidst this transformation, air-safety authorities have intensified their demands for stringent validation and verification processes to ensure the safety and reliability of ML-driven systems deployed within aerospace environments. Yet, industry leaders have only recently begun to confront the complexities of certifying ML models, prompting the initiation of discussions around the development of guidelines and a roadmap for design assurance, especially concerning network-related technologies. This pressing need underscores the imperative for collaborative efforts within the industry to establish robust validation frameworks that not only meet regulatory standards but also address the evolving challenges posed by ML integration.

The aerospace industry stands at a critical juncture as it navigates the integration of machine learning (ML) models into its operational framework. While ML offers unprecedented opportunities for enhancing efficiency and performance, its adoption raises significant concerns regarding safety and reliability, particularly in an industry where even the slightest error can have catastrophic consequences. In response to these concerns, air-safety authorities have intensified their demands for stringent validation and verification processes to ensure that ML

algorithms meet the rigorous standards necessary for certification. However, the complexity of ML systems poses unique challenges for traditional certification approaches, prompting industry leaders to confront a pressing need for comprehensive guidelines and a roadmap. Until recently, the discourse around design assurance for network-related technologies in the aerospace sector has been limited. Recognizing the urgency of the situation, industry stakeholders have begun to collaborate in earnest to develop frameworks that address the intricacies of certifying ML-driven systems. This collective effort aims not only to comply with regulatory mandates but also to instill confidence among stakeholders by establishing robust validation protocols that account for the dynamic nature of ML algorithms and their interactions within aerospace environments. As such, the aerospace industry finds itself at the forefront of shaping the future of certification and safety standards for ML applications, with the imperative to strike a delicate balance between innovation and risk mitigation.

Spacecraft relative motion is an essential part of distributed space systems analysis. It focuses on the dynamics of two or more vehicles, whose relative position (and generally attitude) should be controlled or at least monitored. Rendez-vous operations, formation flying and satellite constellations are three examples of relative motion, all of them being present in contemporary and past missions. Its relevance cannot be underestimated, and its complexity leads to the currently non-existent quorum on its modelling. However, it is quite widely accepted that linear models using State Transition Matrices (*i.e.* STMs onwards) provides a comforting balance between accuracy and computational cost. One could think that, given the huge computational resources that most people have access to, computational efficiency should not even be a concern. Be that as it may, satellites on-board computers have limited resources, both computational and energy-related. Any reduction in any activity is greatly welcomed, and that naturally includes the GNC computation. That is the reason why this thesis focuses on the review, analysis and implementation of STM models of relative motion.

A bottom-up approach to this topic is herewith followed, starting from the simplest relative motion model (HCW), building up complexity with elliptic models (YA) and finally reaching state-of-the-art perturbed models. With respect to perturbations, non-spherical gravity arises as the main concern, due to its prevailing effect over the other sources - third bodies and drag among others - for the Earth-centered orbits (excluding very low LEO orbits or very high orbits, like GEO).

Chapter 1 provides a brief description of the roots of this thesis. Relative motion and

its main branches are firstly described, to then continue with STMs and its applications.

Chapter ?? starts with the development of the equations of relative motion, eventually reaching Hill equations, which model the linearised equations for circular unperturbed reference orbits. Several approaches to its solution are detailed, performing then a small trade-off analysis between them. Finally, orbit safety is presented, to be then applied to the circular, unperturbed case.

Chapter ?? looks for extending the analysis to elliptic (still unperturbed) reference orbits. The state-of-the-art Yamanaka-Ankersen model is developed and tested against a High-Fidelity propagator. To end this chapter, the safe orbit theory is also extended to this elliptic case, through the usage of an analogue set of relative orbital elements and a slightly different relative reference frame.

Chapter ?? tackles the analysis of propagation theory. A brief analysis of averaging methods is discussed, including Von Zeipel's and Lie series' approach. Afterwards, the spotlight is turned on the non-spherical gravity field modelling. The classical Brouwer's theory is first briefed, to then move on to probably the main topic of the thesis: Kaula's theory, which tries to develop a general approach to the spherical harmonic description of the gravity field.

After this theoretical analysis, **chapter ??** moves back to the relative motion field, considering perturbations in this case. An implementation of Brouwer's theory is drafted through Gim-Alfriend STM, after which a survey of the state of the art of perturbed relative motion is presented. To conclude, perturbed orbit safety is simply sketched out.

The pure content of the thesis is then followed by a set of appendices to provide some background in certain relevant topics, if that is required or desired by the reader.

Appendix A provides a comprehensive review and description of the main orbital element sets.

In a somewhat parallel fashion, **appendix ??** focuses on the reference systems used or mentioned throughout the thesis, as well as the transformations between them and from/to orbital elements.

The variational formulation of the spacecraft equations of motion is introduced in **appendix ??**, providing context for some subjects of perturbation theory.

Appendix ?? is devoted to the software approach and structure of the developed content during the thesis.

Finally, **appendix ??** contains several relevant topics that are not big enough to be in-

cluded in an individual appendix, and do not fully fit into the existing ones.

The goal of this thesis is then to provide an educated outlook on the linearised formulation of spacecraft relative motion, building up complexity as it unfolds, eventually reaching state-of-the-art models which are actually used in operational missions. Due to the structure of this field, this finds a niche in the manipulation and understanding of perturbations; as a result of which a considerable part of the thesis is devoted to it. The validation and trade-off evaluation of said models is naturally an essential part of this work as well. However, this thesis is not a result-based work: it is rather a knowledge, analysis-based project, which should be kept in mind along its reading.

The Validation Loop

1.1 Introduction²

1.1.1 Case of study

For illustration of the proposed validation loop, a case of study has been used alongside the theoretical rationale of the loop to generate explanatory figures and tables, demonstrating the loop's effectiveness in real operations.

The case of study is an application of neural networks (NN) in aircraft stress engineering. For typical aircraft fuselage panel design, the dominant form of stiffened post buckling failure under shear loading is forced crippling[6]. This occurs when the shear buckles in the panel skin force the attached stiffener flanges to deform out-of-plane. There are other failure modes related to buckling, tension, and compression.

The aim of the NN model is to predict Reserve Factors (RF) that quantify failure likelihood for regions of the aircraft subject to different loads happening in flight maneuvers (vid. Figure 1.1). The possible failure modes are Forced Crippling, Column Buckling, In Plane, Net Tension, Pure Compression, and Shear Panel Failure.

Input data consists of 26 features (loads applied to a specific region of the aircraft and different maneuver specs). Output data consists of 6 reserve factors that quantify the stress failure likelihood (RF_1 , RF_2 , RF_3 , RF_4 , RF_5 , and RF_6), where $RF_i \in [0, 5]$, where 0 means extreme risk and 5 means risk extremely low (in a logarithmic scale).

This study prioritizes assessing the efficacy of the developed validation tool, not optimizing the neural network model itself. Therefore, the specific architecture and additional features of the NN are intentionally treated as a black box. Our focus remains solely on its inputs –the 26 aforementioned features– and its outputs –the 6 reserve factors representing 6 distinct failure modes–. This simplification allows us to isolate and evaluate the performance of the validation tool without introducing confounding variables related to the specific neural network design.

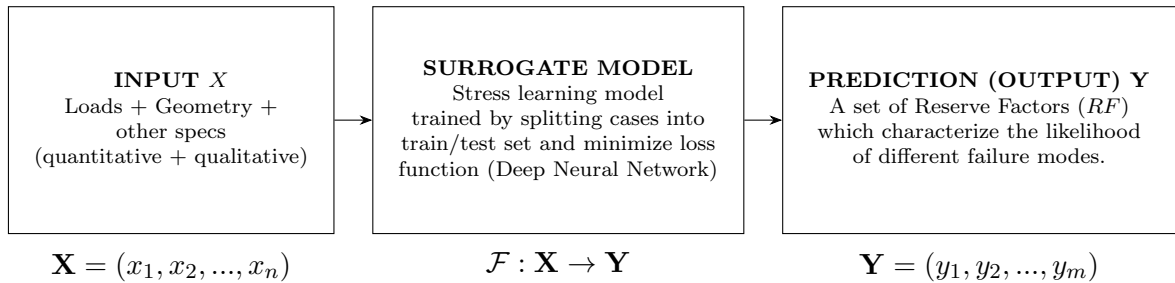


Figure 1.1: Surrogate model pipeline

1.1.2 Applicability

The applicability region can be intuitively defined as the set of the input and output values for which the model's prediction can be trusted. Applicability region is a refined idea of the *Operational Design Domain* of a model.

For a model F to be applicable to a certain new point x :

- x needs to be inside the *input* applicability region of F .
- The prediction $Y = F(x)$ needs to be inside the *output* applicability region of F .

Knowing whether a new point is either inside or outside applicability is a binary decision problem which can be addressed *a priori* (filtering) or be learned *a posteriori* (model boosting). In other words, the binary classification can be addressed from an unsupervised (geometric) learning approach, or a supervised learning approach:

A. Supervised applicability classifiers

Supervised applicability classifiers are based on exogenous criteria. Examples of them include:

- **Operational design domains.** Based on engineer/scientist expertise, only certain combinations and range of features make physical sense. These combinations are used to define a (geometrical) applicability region.
- **Error-filtered convex hull.** Initially the whole set under testing is in applicability range. After filtering those test cases whose prediction error exceeds a tolerance, the applicability region is defined as the convex hull of the remaining subset. The convex hull can be simply defined as the smallest convex set containing the data[7] (vid. [Figure 1.3](#)).

- **Error-labelled classifiers.** Initially a whole subset of the dataset (namely, the test set) is in applicability range. After labelling those test cases whose prediction error exceeds a tolerance as outside applicability, different binary classifiers are trained on the full dataset.

B. Unsupervised applicability classifiers

On the other hand, geometrical applicability classifiers are based on the premise of NN interpolation capabilities. It has been widely discussed (see *e.g.* [8–10]) that NN’s performance relies on their interpolation capabilities, and that no extrapolation capabilities outside their applicability region should be assumed.

Subsequently, from a geometrical approach to the applicability classification problem, we shall define the input applicability region as the geometrical region in the input space where the model is known to work in interpolating regime.

There are plenty of definitions for the interpolating region of a given dataset. Some authors define it as the smallest hypercube enclosing the data[11] (vid. Figure 1.2) although this may seriously challenge interpolation due to isolated points falling into the interpolation region under this definition. Many authors (see v. gr. [12, 13]) define the interpolation region as the *convex hull* of the training data, *i.e.* :

Definition 1. [14] *Standard interpolation occurs for a sample \mathbf{x} whenever this sample belongs to the convex hull of a set of samples $\mathbf{X} \triangleq \{\mathbf{x}_1, \dots, \mathbf{x}_N\}$.*

In the above definition, \mathbf{X} is the training set which has been used for training the model.

Recently, [14] have pointed out that, due to the so-called curse of dimensionality, extrapolation outside the training convex hull always ends up taking place if the input dimension is sufficiently large. The curse of dimensionality[1, pp. 17-18] can be illustrated by the fact that the unitary n -sphere’s volume asymptotically diminishes to 0 as n increases. In the end, the effect is that, as the number of dimensions increase, more data is needed in order for the model to work in interpolating regime, as is showed by the following theorem:

Theorem 1.1.1. [15] *Given a d -dimensional dataset $\mathbf{X} \triangleq \{\mathbf{x}_1, \dots, \mathbf{x}_N\}$ with i.i.d. samples uniformly drawn from a hyperball, the probability that a new sample \mathbf{x} is in interpolation regime (recall 1) has the following asymptotic behaviour:*

$$\lim_{d \rightarrow \infty} p(\mathbf{x} \in Hull(\mathbf{X})) = \begin{cases} 1 & \iff N > d^{-1}2^{\frac{d}{2}} \\ 0 & \iff N < d^{-1}2^{\frac{d}{2}} \end{cases} \quad (1.1)$$

The main answer to the argument of [14] is that interpolation does not occur in the ambient space, but in a latent, low-dimensional space of the input data[16]. This leads to a new definition of interpolation alternative to 1.

Interestingly, the authors in [16] go beyond demonstrating that interpolation occurs (at least in a latent representation of the ambient space). They unveil two more crucial conditions for optimal model performance:

- The training and testing data should share the same cumulative distribution. In situations where this is impossible, matching the tail distribution becomes essential.
- The testing points should not be isolated within the dataset. This means they should have similar characteristics to other data points and not represent extreme outliers that testing and training data follow the same cumulative distribution (or the same tail distribution whenever the former cannot be fulfilled) and that testing points be not isolated in the dataset.

Examples of unsupervised applicability classifiers include:

- **Input space range classifier.** The applicability region is defined as the boundary of the hypercube whose edges are the ranges $[min, max]$ of each input variable in the training set. In practice, this amounts to checking if each numerical feature X_i of the test point lies inside the range spanned by the training subset.
- **Input space convex hull classifier.** The applicability region is defined as the boundary of the convex hull of the training set.
- **Input space isolated region detector.** Even if a point is inside the convex hull of the training set, it can be very far away from other points, thus interpolation can be challenged. Isolated region detectors address this by checking the statistical vicinity of train points and comparing it to the distance of a given test point to the closest training point.

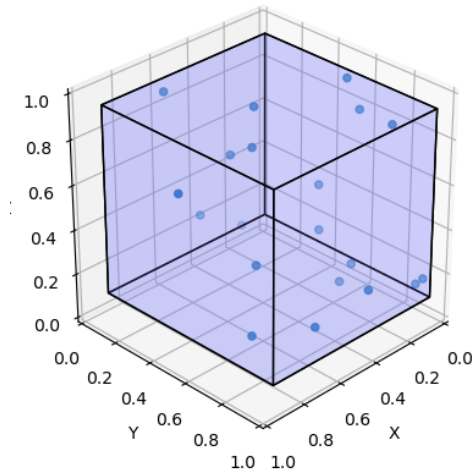


Figure 1.2: Smallest cube enclosing a set of 20 randomly generated points in a 3-dimensional euclidean space.

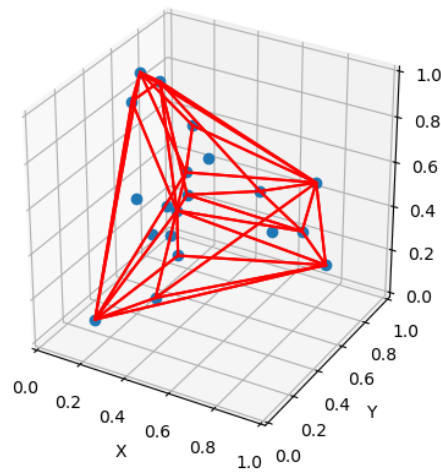


Figure 1.3: Convex hull enclosing the set of Figure 1.2. The convex hull's volume is always smaller than or equal to the volume of the hypercube.

1.1.3 Overview

(Sin acentos) Recorrido sumario por las distintas partes del analisis estadistico (plantillas) centrando en su funcion en vez de su funcionamiento tecnico. Explicacion de la arquitectura general de la validacion.

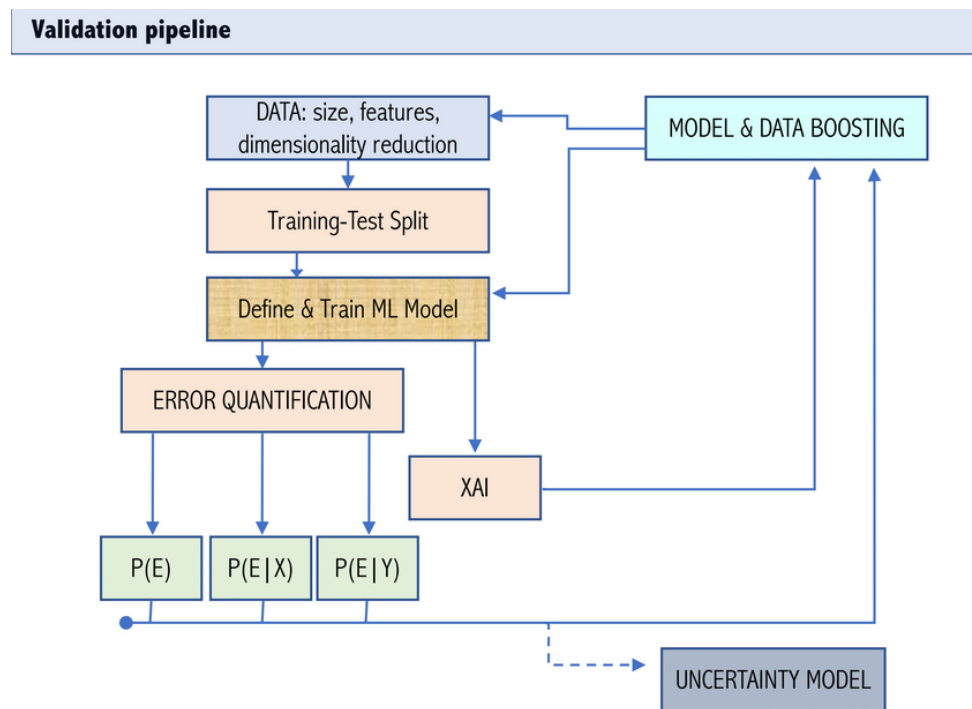


Figure 1.4: Validation pipeline

1.2 Train-test split

1.2.1 Preliminaries

In supervised learning applications, the dataset is typically divided into the training and the testing sets. Keeping different sets for each task is fundamental in order to prevent model bias. Typical figures for the train-test split ratio are 80%-20%. When the model being trained is very large, a third dataset (the validation set) may be needed for comparing different hyperparameter configurations, in which case the split is typically done at 60%-20%-20% for the train, test, and validation sets, respectively[1, pp. 20-21].

Training and evaluating the NN on the same dataset would result in the phenomenon called overfitting[1, pp. 19-20], which basically consists of the NN fitting the noise in the training data and thus losing generalization capabilities.

With the dataset split into the train, evaluation, and test sets, the standard training and validation loop is as follows: the model is trained to "fit" the data in the training set. After a certain amount of training, its performance is measured in the evaluation set. The test set is used to compare the performance of different hyperparameter configurations. Note that the NN is always evaluated with data not previously "seen" during training, and as such cannot develop

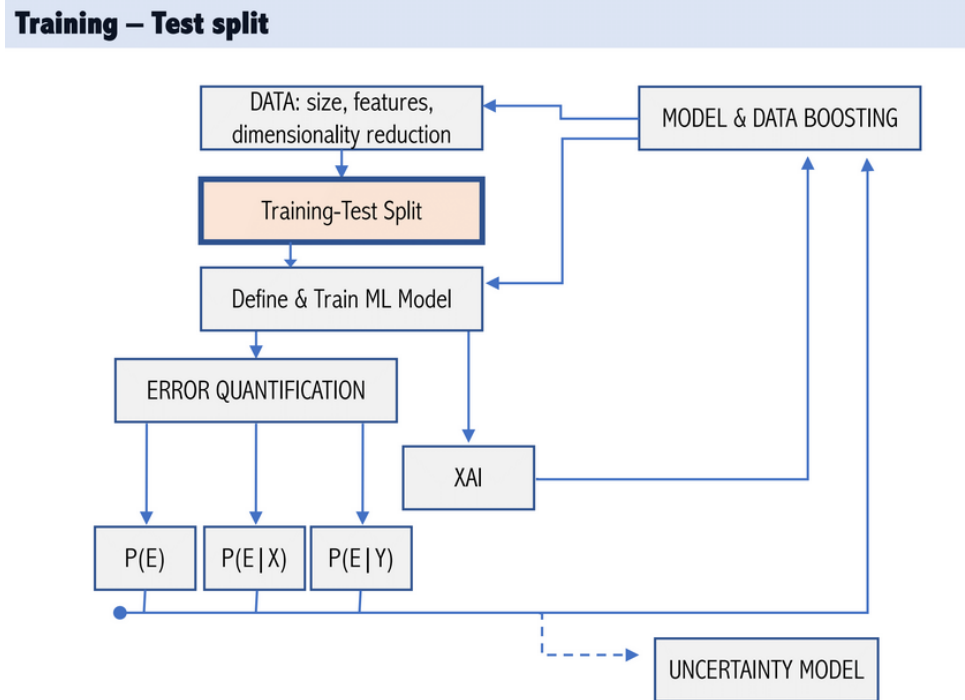


Figure 1.5: Location of the train-test split assessment in the overall validation pipeline

any bias for the training set (although bias for the validation or test sets may exist).

In the model validation loop, the first question that should be asked, even before training the model, is whether the dataset split is appropriate for training (vid Figure 1.5).

For our case of applicability (MSP18, explicar en otra sección), we suppose we have a dataset which has been split into a training set

$$\mathcal{S}_{\text{train}} = \{(\mathbf{X}^{\text{tr}}, \mathbf{Y}^{\text{tr}})_i\}_{i=1}^{N_{\text{training}}}$$

and a test set

$$\mathcal{S}_{\text{test}} = \{(\mathbf{X}^{\text{te}}, \mathbf{Y}^{\text{te}})_i\}_{i=1}^{N_{\text{test}}},$$

where $\mathbf{X} = (X_1, X_2, \dots, X_m)$ is the vector of input variables (also called feature vector), m is the dimensionality of the input parameter space, and $\mathbf{Y} = (Y_1, Y_2, \dots, Y_q)$ is the vector of output variables, with dimensionality q . Individual variables X_k can be numerical or categorical. For instance, for stress problems such as MSP-S18, we have a combination of numerical (*e.g.* external loads) and categorical (eg discrete geometrical variables such as "Frame" or "Stringer", and purely categorical such as "dp"). Individual variables Y_k describe the prediction and these are typically numerical (for stress problems such as MSP-S18, $q = 6$ and these are so-called reserve factors, quantifying the failure likelihood of different failure modes).

The aim of this section is to propose a set of tests to evaluate to which extent splitting fulfils the necessary conditions for the subsequent surrogate model $\mathbf{Y} = F(\mathbf{X})$ to be appropriately trained on $\mathcal{S}_{\text{train}}$ and tested on $\mathcal{S}_{\text{test}}$. This basically means the latter be in the applicability region of a model trained on the former, in order for the training-validation loop of the model to be coherent.

1.2.2 Validation loop for the train-test split

1.2.2.1 Geometrical analysis

To address the applicability classification problem, points in the test set extremely far away from the training set (effectively outside applicability) need to be detected. If found, that would mean the train-test split is incorrect.

There is a wide range of criteria for classifying a point inside or outside applicability. The proposed validation loop makes such analysis following a hierarchical flow. For each point in the test set a decision is made based on where that test set point lies with respect to the training

set.

Because categorical variables are usually related to different physical conditions, the first step is to condition the analysis of each test point only with respect to the training subset of points whose categorical variables have exactly the same values than the test point under analysis. This conditioning on categorical variables defines, for each test point, a *voxel*, *i.e.* a region in the input space defined by the precise values of each categorical variable. At this point the first requirement comes into play: the number of training samples inside such voxel needs to be large enough (*e.g.* larger than zero).

Then, inside the voxel the ranges of each feature X_i of the training subset are computed, and then the maximum ranges are checked and defined. Their cartesian product defines the voxel's hypercuboid volume associated to the numerical features. It is checked whether the test point is inside or outside the hypercube. In practice, this amounts to checking if each numerical feature X_i of the test point lies inside the range spanned by the training subset. If all numerical features fall inside these ranges, the test set falls inside the training subset hypercuboid, otherwise, it falls outside. The points lying outside such hypercuboid are outside applicability and are flagged. The "hypercube requirement" is that such percentage of points outside applicability is zero, or very close to it.

If the test point under analysis is found to be outside the hypercuboid, the analysis finishes and the loop moves to the next point. Otherwise, the second step is to check whether this point not only lies inside hypercuboid, but further, whether it also lies inside the convex hull spanned by the training subset in a PCA99¹ projection. This hull has a smaller volume than the hypercuboid. If the test point under analysis is found to be outside the convex hull in the PCA99 projection, the analysis finishes and the loop moves to the next point.

Otherwise, then the third step is to check whether this point (not only lies inside hypercuboid and CH_{PCA99}, but also) lies inside the convex hull spanned by the training subset in ambient space. The volume of this hull is typically smaller than the one of the PCA99 projection by virtue of the curse of dimensionality, and if the test point lies inside this hull, interpolating properties of the surrogate model will suggest that the model is not require to generalize outside the region where it cannot generalize.

The step of the PCA projection is motivated by the curse of dimensionality, which makes every test point be in extrapolating regime with respect to the training data when the convex hull of

¹A truncated PCA[17] projection in which the selected components explain at least 99% of the whole variance of the data.

the raw, unprocessed training data is used in a high-dimensional input space, as pointed out by [14]. The work of [16] effectively shows how in such cases, a low-dimensional space is more useful for applicability classification.

Each step provides different level of evidence of whether the point under analysis was adequately located, where the best is that it lies inside the convex hull of the corresponding voxel in ambient space, and the worst is that it lies outside the hypercuboid.

An additional check is to analyse whether p-hacking is happening, *i.e.* whether the test set point is "too close" to an actual training point (or indeed equal to a training point), what would falsely induce low test error of the model. For this, we measure the distance of the test point to the closest point of the training subset. This information is later used to assess different aspects of potential p-hacking and its impact on the decision of train-test split correctness.

The former procedure for classifying the applicability of test points is summarised in [algorithm 1](#).

Output of [algorithm 1](#) is depicted in [Table 1.1](#). This information has to be processed to complete [Table 1.4](#). The first column identifies the test point inside the test set. The next three columns show information about the corresponding voxel: existance, identification and size. Columns 5 to 7 show information related to pointwise distances inside the voxel. The last three columns show the relative position of the test point inside the voxel (inside the hypercube/convex hull in PCA99/convex hull in ambient space). In this algorithm, if the test point is found to be outside the hypercube (CH_{PCA99}), then its position with respect to CH_{PCA99} and $\text{CH}_{\text{ambient}}$ ($\text{CH}_{\text{ambient}}$) is not computed in the sake of computational efficiency.

To better understand how the voxels are computed, a reference of their categorical variables is given in [Table 1.2](#). Points inside each voxel all have the same categorical values, which effectively act as a unique identifier for the voxel. We see each voxel represents a different stringer section between two concrete frames, plus the categorical variable "np" which can take the values either 0 or 0.9.

Data in the column "inside vox. hypercube" of [Table 1.1](#) has been rearranged for the sake of interpretability in [Table 1.3](#). This table shows the points which lie outside the training voxel hypercube for every voxel where such points exist. Similar tables could be arranged with the number of points belonging to the hypercube but not to the convex hull in a PCA99 projection, or with those points belonging to the convex hull in a PCA99 projection but not in ambient space.

Algorithm 1: Train-test split geometrical analysis

Data: $\mathcal{S}_{\text{train}}, \mathcal{S}_{\text{test}}$, voxel_size_req

Result: inside_hypercube, inside_PCA99, inside_ambient, avg_train_dist, min_test_dist

```

1 Initialize empty lists: test_voxels, train_voxels  $\leftarrow []$ ;
2 Initialize boolean arrays:
   inside_hypercube, inside_PCA99, inside_ambient  $\leftarrow [\text{False}, \dots, \text{False}]_{1 \times \text{len}(\mathcal{S}_{\text{test}})}$ ;
3 Initialize arrays for distances: avg_train_dist, min_test_dist  $\leftarrow [\text{NaN}, \dots, \text{NaN}]_{1 \times \text{len}(\mathcal{S}_{\text{test}})}$ ;
4 foreach  $\mathbf{X} = (\mathbf{X}_{\text{numerical}}, \mathbf{X}_{\text{categorical}})$  in  $\mathcal{S}_{\text{test}}$  do
5   Compute test_voxel by imposing  $\mathbf{X}_{\text{categorical}}$ ;
6   Append test_voxel to test_voxels;
7 end
8 foreach  $\mathbf{X} = (\mathbf{X}_{\text{numerical}}, \mathbf{X}_{\text{categorical}})$  in  $\mathcal{S}_{\text{train}}$  do
9   Compute train_voxel by imposing  $\mathbf{X}_{\text{categorical}}$ ;
10  Append train_voxel to train_voxels;
11 end
12  $i \leftarrow 0$ ;
13 foreach test_voxel in test_voxels do
14   Get train_voxel by imposing  $\mathbf{X}_{\text{categorical}}$ ;
15   Compute main nearest neighbour distance inside train_voxel:
       $\bar{d}_{\text{train}}(\text{train_voxel}, \text{train_voxel})$ ;
16   avg_train_dist[i]  $\leftarrow \bar{d}_{\text{train}}$ ;
17   if size(train_voxel)  $\geq$  voxel_size_req then
18     foreach  $\mathbf{X}$  in test_voxel do
19       Compute minimum nearest neighbour distance:  $d_{\text{test}}(\mathbf{X}, \text{train_voxel})$ ;
20       min_test_dist[i]  $\leftarrow d_{\text{test}}$ ;
21       if  $\mathbf{X}$  not in hypercube then
22         break;
23       else
24         inside_hypercube[i]  $\leftarrow \text{True}$ ;
25         if  $\mathbf{X}$  not in CH_PCA99 then
26           break;
27         else
28           inside_PCA99[i]  $\leftarrow \text{True}$ ;
29           if  $\mathbf{X}$  in ambient_hull then
30             inside_ambient[i]  $\leftarrow \text{True}$ ;
31           end
32         end
33         i  $\leftarrow i + 1$ ;
34       end
35     end
36   end

```

Table 1.1: Output of algorithm 1.

	Vox. exists	Vox. ID	Vox. size	Min. test to train vox. dist.	Min. train to train vox. dist.	Avg. train to train vox. dist.	Inside vox. hypercube	Inside vox. CH (PCA99)	Inside vox. CH (ambient)
0	True	729	10	4.2222	2.3103	4.9535	False	NaN	NaN
1	True	703	10	6.8161	3.5068	6.2151	True	False	NaN
2	True	211	10	3.2955	1.6819	4.4763	False	NaN	NaN
3	True	799	8	NaN	NaN	NaN	NaN	NaN	NaN
4	True	531	6	NaN	NaN	NaN	NaN	NaN	NaN
...
1995	True	102	8	NaN	NaN	NaN	NaN	NaN	NaN
1996	True	536	11	3.3157	2.8551	4.4765	True	False	NaN
1997	True	770	6	NaN	NaN	NaN	NaN	NaN	NaN
1998	True	634	10	1.1911	1.8775	5.0745	True	False	NaN
1999	True	277	10	4.8021	3.1150	5.6874	True	False	NaN

2000 rows × 9 columns

Table 1.2: Voxel reference table

Voxel	
Voxel ID	
0	(0.0, Fr68-Fr69, Str40)
1	(0.9, Fr66-Fr67, Str36p)
2	(0.0, Fr69-Fr70, Str29)
3	(0.9, Fr69-Fr70, Str35)
4	(0.0, Fr65-Fr66, Str01)
...	...
827	(0.9, Fr64-Fr65, Str21)
828	(0.9, Fr66-Fr67, Str32)
829	(0.0, Fr64-Fr65, Str26p)
830	(0.0, Fr64-Fr65, Str29p)
831	(0.0, Fr67-Fr68, Str07)

751 rows × 1 columns

This information is used to check the following parameters and requirements, which are stored in [Table 1.4](#):

- Whether there are enough training samples inside each training subset is compared with `voxel_size_req`.
- The percentage of test points inside the ranges of the training samples is compared with `hypercube_req`.
- The number of points inside the hypercube but outside `CH_PCA99` is compared with `CHMP_PCA99_negative_req`.
- The number of points inside the hypercube and `CH_PCA99` but outside `CH_ambient` is compared to the requirement `CHMP_ambient_negative_req`.
- The total number of points inside `CH_ambient` is compared to `CHMP_ambient_abs_req`.
- All these requirements are stored in [Table 1.4](#).

Having analysed the isolation level of test points, it is necessary to check whether p-hacking is taking place. That is, whether test points are unrealistically close to train points, thus making the model evaluation flawed. This is measured using the Mann-Whitney U test[[18](#)]. In this test, the initial hypothesis H_0 is that both distributions are the same. H_1 is that the distribution underlying test-training distances is stochastically less than distribution underlying training-training distances, which would involve risk of p-hacking. H_0 is rejected only with a 95% confidence. For instance, for the dataset of MSP-18, the resulting p-value is $p = 0.9793$, thus the null hypothesis is not rejected and the dataset can be assumed to be free of p-hacking.

1.2.2.2 Non-geometrical analysis

To help (the engineer in charge) make a decision about the dataset split, another approach is developed, complementary to the geometrical analysis carried out so far. This approach consists of focusing on the statistical distributions of the train and the test datasets. A proper train-test split is characterised by similar statistical distributions of both sets (test and training)[[16](#)]. When this cannot be achieved, a softer requirement is that each of the feature variables X_i need to have reasonably similar marginal distributions in the training and the test set.

The following analysis checks whether, for each individual input feature, the distribution of the training and test set is reasonably similar. This is also checked for the output variables

Table 1.3: Points outside voxel hypercube

Voxel ID	Voxel	Num. of test points belonging to voxel	Num. of test points outside voxel's hypercube
729	(0.0, 'Fr66-Fr67', 'Str28')	2	2
703	(0.0, 'Fr65-Fr66', 'Str29')	3	2
211	(0.0, 'Fr66-Fr67', 'Str40')	4	3
219	(0.0, 'Fr64-Fr65', 'Str35')	4	3
413	(0.9, 'Fr68-Fr69', 'Str05p')	5	4
...
561	(0.9, 'Fr69-Fr70', 'Str43')	2	1
436	(0.0, 'Fr64-Fr65', 'Str40p')	1	1
276	(0.0, 'Fr64-Fr65', 'Str31')	1	1
109	(0.0, 'Fr69-Fr70', 'Str04')	2	1
446	(0.9, 'Fr69-Fr70', 'Str21')	1	1
104 rows × 3 columns			

Table 1.4: `reqs_results_table`. The first and the last requirements compare absolute figures of points at some isolation level with the overall number of points. Whereas the second and third requirements compare the difference in number of points between two consecutive levels with the total number of points.

	Desired rate (equal or less)	Obtained rate
Hypercube rate	0.1000	0.5780
CHMP PCA99 negative rate	0.1000	0.3880
CHMP ambient negative rate	0.1000	0.0340
CHMP ambient abs rate	0.1000	0.3880

(the ground true ones, thus this is independent from the surrogate model). Finally, the splitting can be done locally, *i.e.* region by region, by binning each numerical variable. The implementation of this analysis tackles each input variable X_i independently and for each input variable, it compares the training and the test set such that:

- If the variable X_i is ‘categorical’: both (train and test) categorical frequency distributions are plotted (Figure 1.7), a 2-sample χ^2 test[19, p. 431] is performed, and the p-value of such test is introduced in Table 1.5.
- If the variable X_i is numerical: both (train and test) numerical frequency distributions are plotted (Figure 1.6), a 2-sample Kolmogorov-Smirnov test[19, p. 454] is carried out, and the p-value of such test is introduced in the same table.

The null hypothesis for both tests is that both train and test distributions are the same. H_0 is only rejected with a 95% confidence.

As stated earlier, applicability is not only a matter of the *input* space, but also of the *output* space. The 2-sample Kolmogorov-Smirnov test has been performed again on each of the six output variables. The p-values and their statistical distributions are depicted in Table 1.6 and Figure 1.8, respectively.

1.2.2.3 Train-test split. Conclusions

The proposed validation loop for the train-test split focuses, on the one hand, on the applicability classification problem, which makes use of a geometrical analysis which classifies test points at different levels of isolation. A series of requirements are defined based on the proportions of such isolated points. Plus, p-hacking is checked. The output of this analysis is showed in Figure 1.9.

On the other hand, the distributions of both input and output variables in the training set are checked to be reasonably similar to that of the test set. The main outputs are the p-values shown at Table 1.5 and Table 1.6.

Of course, any given dataset may meet some of the requirements, but not all (as is the case with the MSP-18 dataset). The engineer in charge should evaluate the ensemble output and decide whether it is necessary to redo the split completely or partially, depending on data

Table 1.5: P-values of the input variables. The test performed is a 2-sample Kolmogorov-Smirnov or a 2-sample χ^2 test, depending on the data being numerical (first 19 rows) or categorical ("dp", "Frame" and "Stringer").

p-values	
	p-value
factors	0.97409
FU.0410.14	0.08896
FU.0410.15	0.77249
FU.0410.16	0.53206
FU.0410.24	0.31840
FU.0410.25	0.54828
FU.0410.26	0.58953
FU.0420.14	0.19180
FU.0420.15	0.50018
FU.0420.16	0.58953
FU.0420.24	0.54015
FU.0420.25	0.34948
FU.0420.26	0.74838
FU.0430.14	0.16084
FU.0430.15	0.17195
FU.0430.16	0.51601
FU.0430.24	0.55646
FU.0430.25	0.42458
FU.0430.26	0.66518
dp	0.99969
Frame	1.00000
Stringer	1.00000

availability.

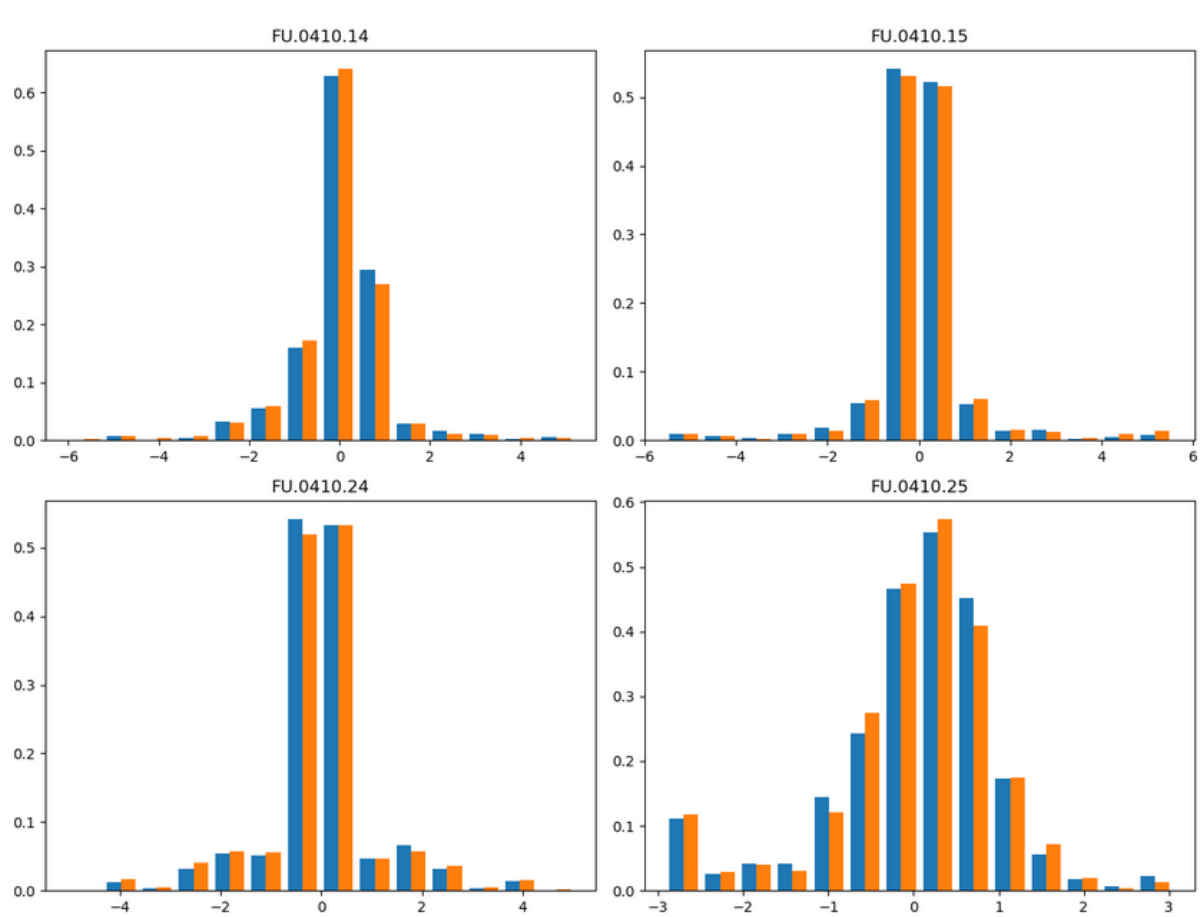


Figure 1.6: Input [numeric] variables distributions double histogram. Only the first four input variables have been plotted.

Table 1.6: P-values of the output variables distributions

	p-values	KS
RF Forced Crippling	1.00000	
RF Column Buckling	1.00000	
RF In Plane	1.00000	
RF Net Tension	0.24668	
RF Pure Compression	1.00000	
RF Shear Panel Failure	0.99995	

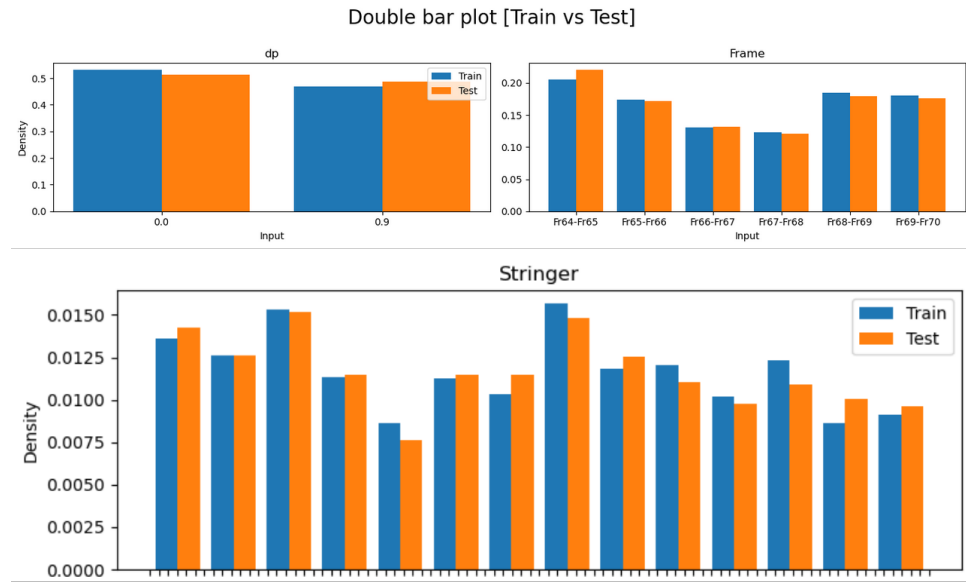


Figure 1.7: Input categorical variables distributions double histograms

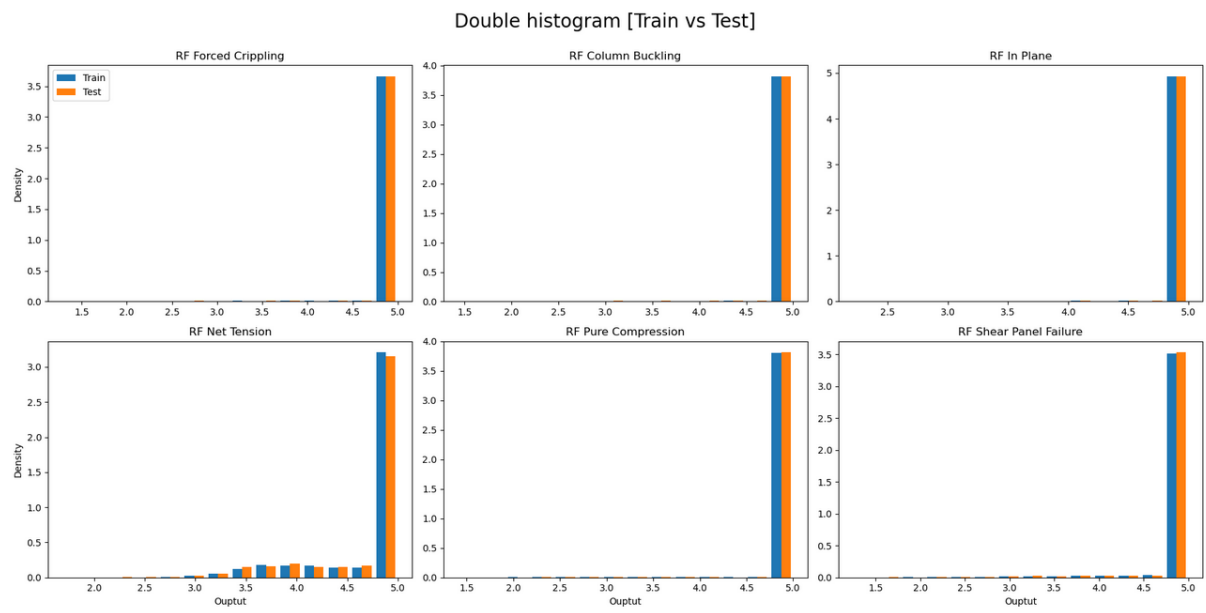


Figure 1.8: Output variables distributions double histograms

Requirement check		
Type	Check	
Variable Compatibility Check	Optional	True
Voxel Size	Optional	None
Voxel Hypercube Rate	Optional	False
CHMP PCA99 (negative)	Optional	False
CHMP ambient (negative)	Optional	True
Mann Whitney U test pvalue	Optional	True

Figure 1.9: Requirements of the geometrical analysis

1.3 Global error quantification

This section corresponds to box labelled "Error quantification" in Figure 1.4.

After running the model, the simplest analysis of its performance consists of measuring the aggregated error of predictions against ground true values over the whole test set. Different metrics and criteria can be adopted for this task. Common error measures are the Mean Absolute Error (MAE) and the Root Mean Square Error (RMSE). These metrics account for the distance between points representing ground true values (\mathbf{Y}) and model's predictions ($\tilde{\mathbf{Y}}$), taken as the $L1$ norm (MAE) or the square of the $L2$ norm (RMSE) of the distances. In many industrial applications of machine learning, difference between ground true and predicted values can be more or less important depending on whether that difference is due to *overestimating* or *underestimating*. Take, for instance, the case of MS-S18 model, whose predictions are a measure of the probability of failure of aeronautical structural components. Clearly, underestimating the risk is much more dangerous than overestimating it. For cases such as this one, a useful measure of the error is the **residue**. The residual error of a given point i is measured as

$$\mathbf{e}(i) = \mathbf{Y}(i) - \tilde{\mathbf{Y}}(i) \quad (1.2)$$

The drawback of the residual error is that, when using it as an aggregated indicator for the whole test set, residues can cancel out. A null MAE or RMSE account for a perfectly fitted model (ground true values and predictions are equal). That is not the case for the residual error. In the following sections, unless specifically specified, the metric of choice for measuring the error is the residue (Equation 1.2), although different error metrics are also supported from an implementation point of view, one of the most common alternatives being the absolute value of the residue, $|\mathbf{e}|(i) = |\mathbf{Y}(i) - \tilde{\mathbf{Y}}(i)|$.

An interesting scalar metric for the global performance of the model is the coefficient of determination R^2 [20] of the scatter distribution of \mathbf{Y} vs $\tilde{\mathbf{Y}}$. R^2 is a measure of the goodness of fit of predicted to ground true values. Illustration of this is provided in Figure 1.10. The most important conclusion of Figure 1.10 is that the error shows to be heteroscedastic², as demonstrates the fact that dispersion is higher for higher Reserve Factors (interestingly, this is the desired behaviour, as lower Reserve Factors implicate higher failure risk, and thus precision

²This means the variance of the error is not constant along some variable range (in this case, that variable is the output variable named "RF Net Tension"). In Figure 1.10 we can clearly see that dispersion grows with the output value. Cfr.[21, p. 374].

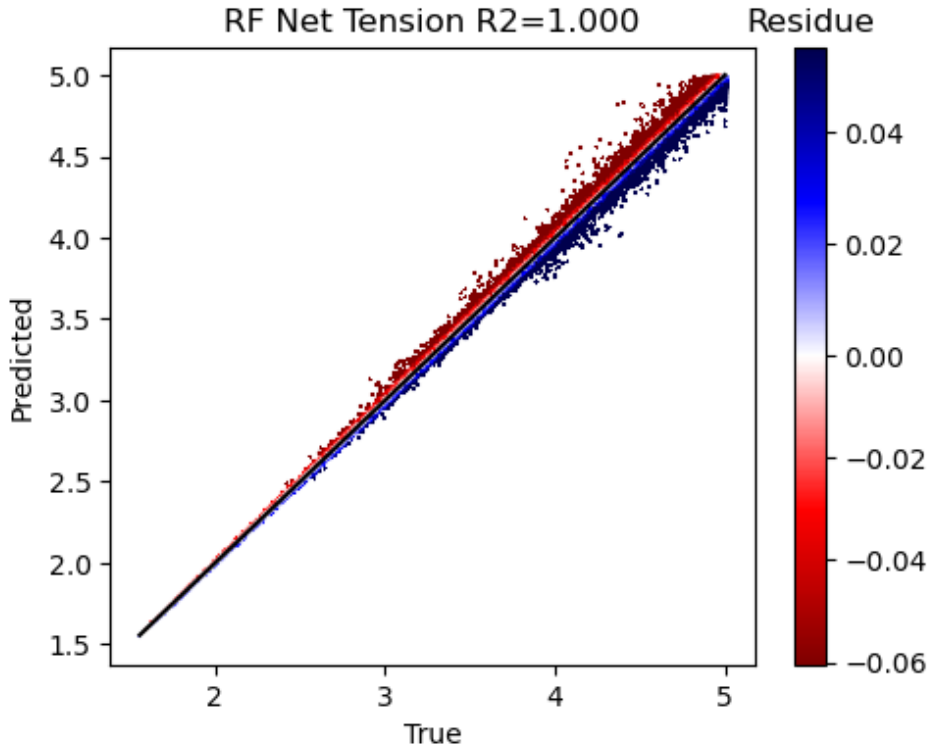


Figure 1.10: Scatter plot of ground true (x axis) against predicted values (y axis) of output variable "RF Net Tension", with the correspondent R^2 coefficient. In this case, $R^2 = 1,000$ indicates a perfect fit of predicted to ground true values. Mismatches due to underestimating failure risk are labelled in red, while those due to overestimating failure risk are labelled in blue. Similar graphs can be computed for every pair $\{y_j, \hat{y}_j\}$ of features in the output variables $\mathbf{Y} = \{y_1, y_2, \dots, y_m\}$. Plots for the rest of the six output variables of MS-S18 show analogous results.

is more important in the region of low Reserve Factors). This property makes it necessary to study the error distribution, as well as the error distribution conditioned on input and output space ($P(e)$, $P(e|\mathbf{X})$ and $P(e|\mathbf{Y})$, resp.) as is discussed in the following sections.

1.4 Distributed error quantification.

This section corresponds to box labelled " $P(E)$ " in Figure 1.11. From now on, the terms "error" and "residue" (as defined in the previous section) will be used as synonyms.

Beyond global error statistics, the PDF of the residue, $P(e)$, is of great importance for

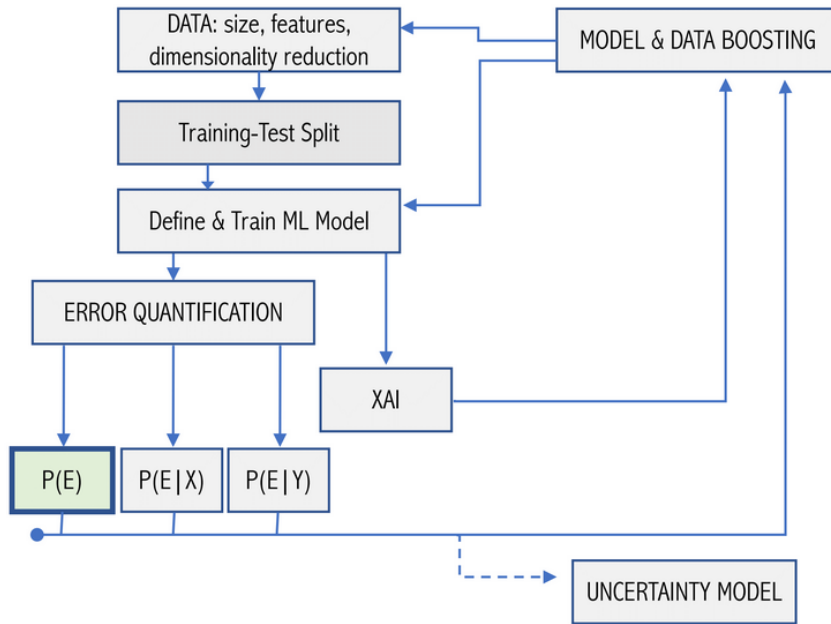


Figure 1.11: Location of ?? in the validation pipeline.

validation purposes. The main goal of this section is finding the analytic expression of $P(e)$ and computing important statistics of it, and, when the first is not possible, computing the important statistics from the empirical distribution of the residue (sampled from test set points) with the method of bootstrapping³. There are three main reasons for studying $P(e)$:

A. Non gaussian error distribution

It is common in industry-applied problems to find situations in which the error between ground-true values and predictions coming from a regression model (let it be a surrogate ANN, some parametric regressor, etc.) which is supposed to fit any function describing a complex system follows absolutely non-Gaussian distributions (see e.g. [22–25]). Amongst the reasons for

³Vid. following paragraphs

this, the most frequent are, on the one hand, non-homogeneous data sampling in the training set (leading to uncovered regions and isolated points) which can cause poor model performance due to non-interpolation-regime operation, and on the other hand, the inherent difficulty encountered at predicting outputs for specific input configurations due to strongly non-linear physics or governing equations (mathematically this manifests in the form of high gradients). When the error is non-Gaussian, concentration statistics such as MAE or RMSE stop being informative. In such case, a comprehensive analysis on $P(e)$ is more adequate.

B. Outlier detection

Outliers are strange events in a population sampled from a known PDF, in the sense that it is not expected to find them, or that their position is far away from expected. Outlier detection helps identifying strange phenomena which the engineer in charge could decide to investigate. Imagine, for instance, that certain residue e_x was systematically sampled from the test set with an unusual frequency, compared with similar values. In this case, it would be necessary to assess whether this high frequency is statistically expectable from the residue's PDF or not. If e_x was found to be an outlier, determining the underlying reason triggering such high frequency would help with model boosting.

Outlier detection relies on knowing $P(e)$. The probability of finding a residue larger than a given magnitude x is measured as $p_{>x} = \int_x^\infty P(e) de$. If we find some x for which $p_{>x} \ll 1$, all samples of the residue $e > x$ would be classified as outliers. This simple idea lies behind standard outlier-detection methods such as the z-score and the gESD (which are later discussed).

C. Uncertainty measuring

The marginalised distribution of $P(e)$ is the first step in the journey towards building an **uncertainty model**. This is the ultimate milestone of the whole validation pipeline, since it provides precise information about *how much* and *when* the model's predictions are trustworthy. This is the whole point of [section 1.7](#). The uncertainty model relies on the marginalised distribution of the residue for building confidence intervals which embed the model's error with a given statistical confidence level.

A simple plot can help us have a first intuition for the cause of subsequent results presented in this section. In [Figure 1.12](#) ground true values and model's predictions are represented in a double histogram for MS-18.

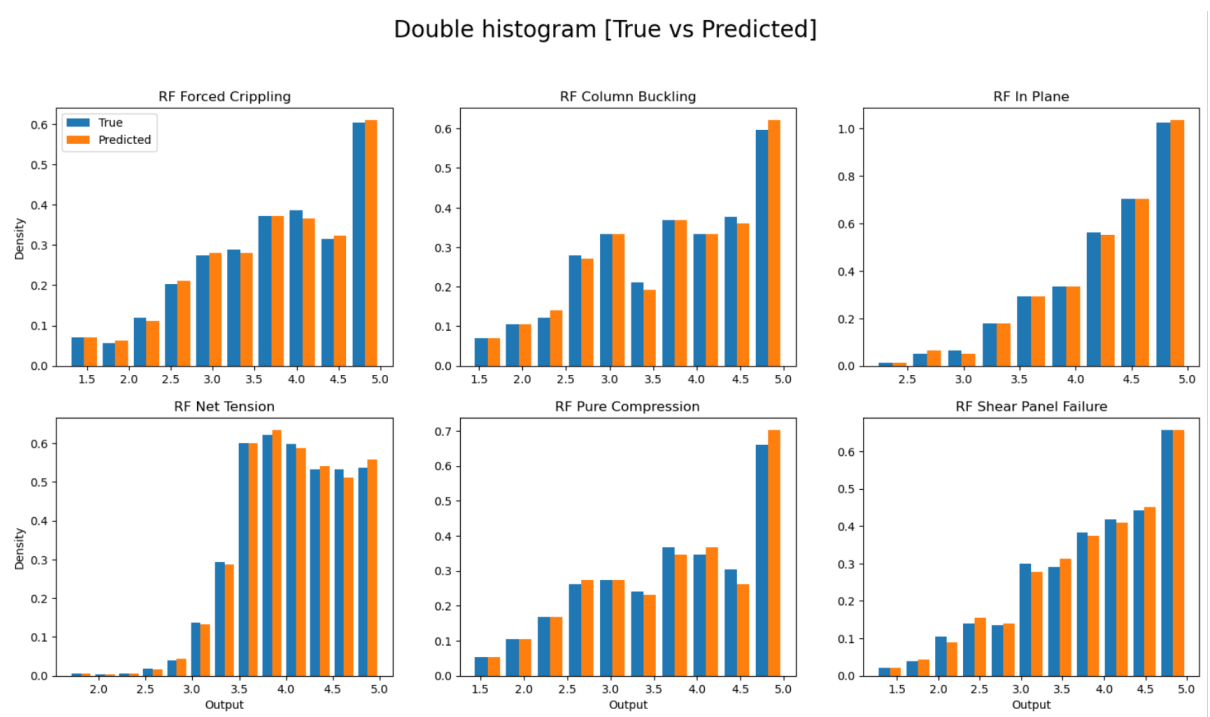


Figure 1.12: Double histogram depicting ground true values and model's predictions for the six output variables of MS-18.

If the model accurately predicts results along the whole output variables range (or equivalently it is not heteroscedastic), we would expect both the true and the predicted results to come from the same (unknown) distribution (this hypothesis is taken as H_0). We can test this with a (2 sample) goodness-of-fit test like the Kolmogorov-Smirnov. Once again, the null hypothesis is rejected only at a 95% confidence level (*i.e.* if the p-value derived from the K-S test is lower than 0.05). The corresponding p-values of the K-S test for the six output variables of MS-18 are depicted in [Table 1.7](#).

In [Table 1.7](#) we can see how the K-S test rejects the null hypothesis in some cases despite distributions in [Figure 1.12](#) looking very similar. This is due to the K-S test sensitivity to the size of datasets.

As it has been previously mentioned, outlier detection and uncertainty models both rely on the PDF of the residue, $P(e)$. The main goal of this section is finding the analytical definition of $P(e)$ ⁴, and measuring important statistics of it. This is addressed with a focus similar to that followed in [Figure 1.12](#) and [Table 1.7](#), but instead of assessing the fitness of the predictions (\hat{y}) distribution to the ground true values (y) distribution, we try to assess the goodness of fit of the

⁴This might not always be possible. When it is not, non-parametrical bootstrapping is given as an alternate solution (vid. next paragraphs).

Table 1.7: Resulting p -values from the 2-sample K-S test of goodness of fit between ground true (\mathbf{Y}) and predicted ($\hat{\mathbf{Y}}$) distributions. The null hypothesis H_0 that both distributions conform is rejected if the p -value is smaller than 0.05.

Hypothesis Tests Results (p-value)	
	KS
RF Forced Crippling	0.03763
RF Column Buckling	0.11906
RF In Plane	0.03428
RF Net Tension	0.60624
RF Pure Compression	0.08367
RF Shear Panel Failure	0.03510

empirical residue distribution to some well-known distributions. For reference, the (empirical) error distribution of the six output variables is depicted in Figure 1.13, as well as the corresponding cumulative distributions, given in Figure 1.14.

Under the assumption that $P(e)$ can be described by some well-known parametric distribution, we use the 1-sample K-S test (coupled with a minimal-squares based optimizer to find the optimal set of parameters for each distribution) to compare distributions of Figure 1.13 to the following distributions:

- Normal:

$$f(x|\mu, \sigma) = \frac{1}{\sigma\sqrt{2\pi}} \exp\left(-\frac{(x-\mu)^2}{2\sigma^2}\right)$$

- Laplace:

$$f(x|\mu, b) = \frac{1}{2b} \exp\left(-\frac{|x-\mu|}{b}\right)$$

- Cauchy:

$$f(x|x_0, \gamma) = \frac{1}{\pi\gamma \left[1 + \left(\frac{x-x_0}{\gamma}\right)^2\right]}$$

- JohnsonSU:

$$f(x|\gamma, \delta, \lambda, \xi) = \frac{\delta}{\gamma\sqrt{2\pi}} \frac{1}{x+\xi} \exp\left(-\frac{1}{2}(\gamma + \lambda \log(x+\xi))^2\right)$$

P-values from the K-S test are given in Table 1.8. As we can see, the normal distribution does not fit any of the output variables' error. While Laplace and Cauchy distributions' p-values

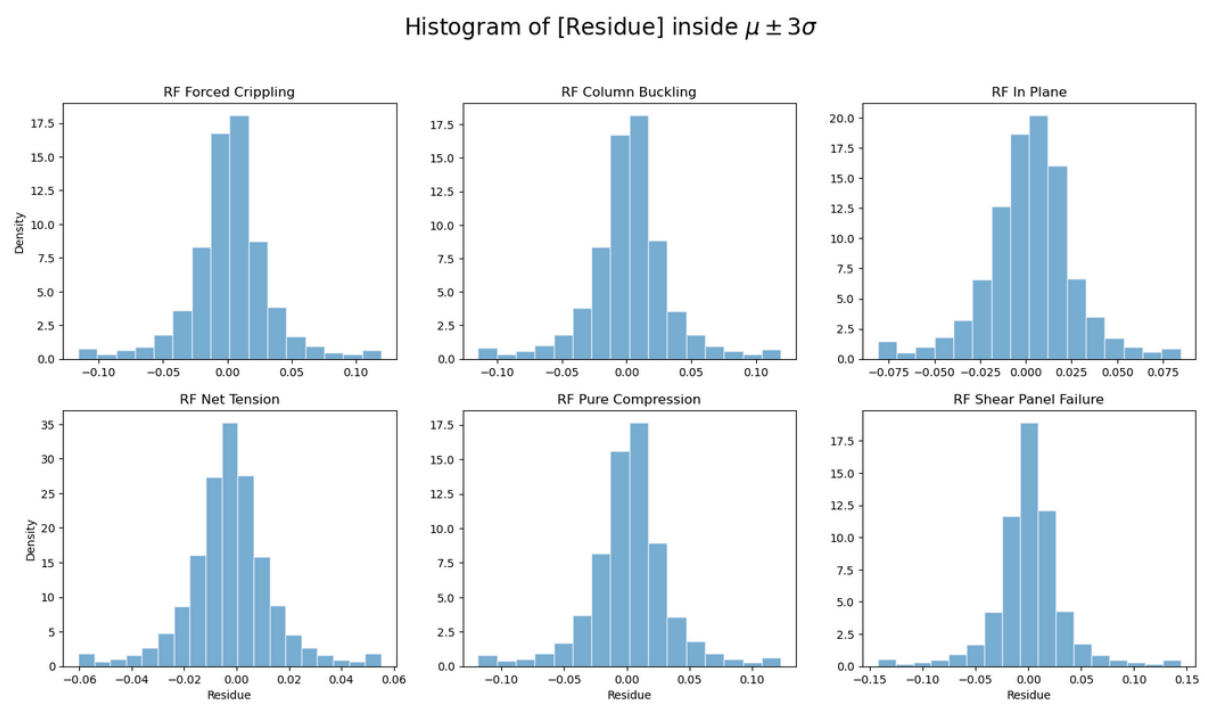


Figure 1.13: Empirical residue distribution sampled from the test set, for each of the six output variables of MS-S18. x -axis limits have been truncated to $\mu \pm 3\sigma$, where the most part of the error lies. Histograms have been appropriately binned for a correct visualization.

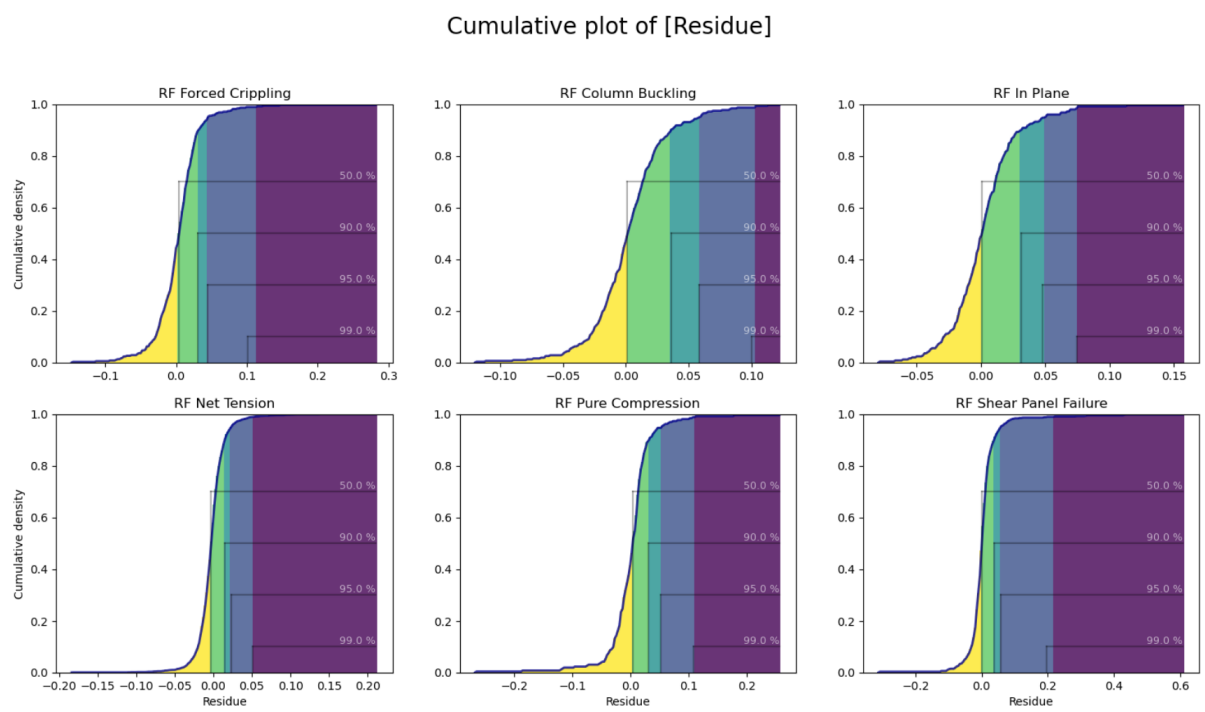


Figure 1.14: Cumulative error distributions corresponding to the PDFs showed (as binned histograms) in Figure 1.13.

from the K-S test are above the 0.05 threshold in five of the six output variables, they are well below the obtained p-values for the JohnsonSU[26] distribution (vid. Figure 1.15). In fact, when augmenting the dataset size from the illustrative-sized employed here (10,000 items) to a more realistic 800,000 items, neither of Laplace and Cauchy distributions pass the test (their p-values drop to near-zero orders of magnitude). This happens due to the K-S sensibility to the size of data, which makes the test more strict when the datasets are large (as would be expected). We conclude that the Laplace and Cauchy distributions just pass the K-S anecdotally for the unrealistically small dataset size which has been used for illustrative purposes, and we also conclude that the only theoretical distribution (of the list which has been checked) that fits the MS-18's error distribution is the JohnsonSU.

Provided that there exists a simple transformation of the JohnsonSU distribution's random variable (vid. Figure 1.16) that converges to a normal distribution, one can, with the information obtained from the K-S test (that is, assuming the error data comes from a JohnsonSU distribution) apply standard outlier detection methods to a transformed variable $z \sim \mathcal{N}(0, 1)$, like the z-score (every point located outside $\mu \pm 3\sigma$ is considered to be an outlier) and the generalised Extreme Studentized Deviate[27] (gESD), thus fulfilling the aims described at the beginning of this section concerning outlier detection (vid. Table 1.9).

Results shown in Table 1.7 rise some concerns about the method followed until now.

Table 1.8: P-values of the K-S test comparing the empirical sample of $P(e)$ to the theoretical distributions indicated in each column. The null hypothesis H_0 (the empirical distribution has been sampled from the one figuring in a given column) is rejected when $p - \text{value} < 0.05$.

	Fit to each output-metric			
	Norm	Laplace	Cauchy	Johnsonsu
RF Forced Crippling	0.004	0.138	0.138	0.613
RF Column Buckling	0.043	0.328	0.435	0.954
RF In Plane	0.005	0.691	0.691	0.616
RF Net Tension	0.000	0.060	0.001	0.843
RF Pure Compression	0.001	0.053	0.438	0.791
RF Shear Panel Failure	0.000	0.002	0.453	0.716

The immediate concern that arises is what would happen if we were unable to find a theoretical distribution that fits some variable's error distribution with a statistically significant confidence level. In fact, the most common statistical distributions (normal, Laplace, Cauchy)

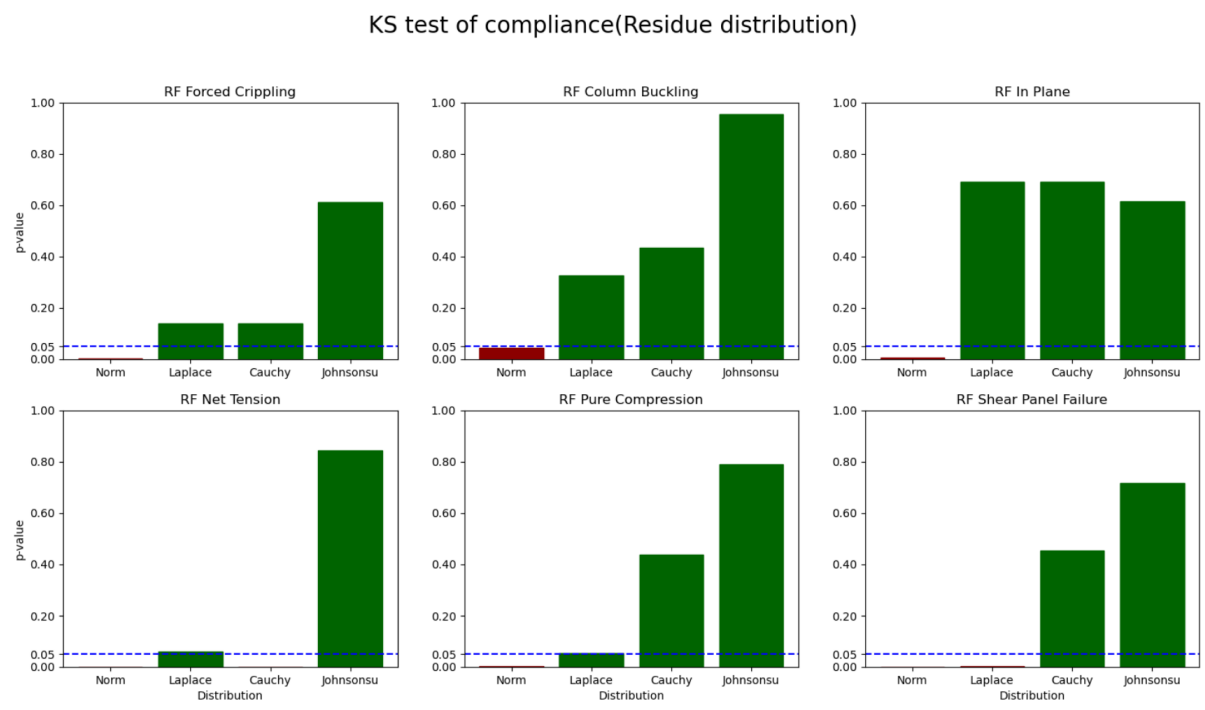


Figure 1.15: Graphical comparison of the p-values resulting from the K-S test for the MS-18 data.

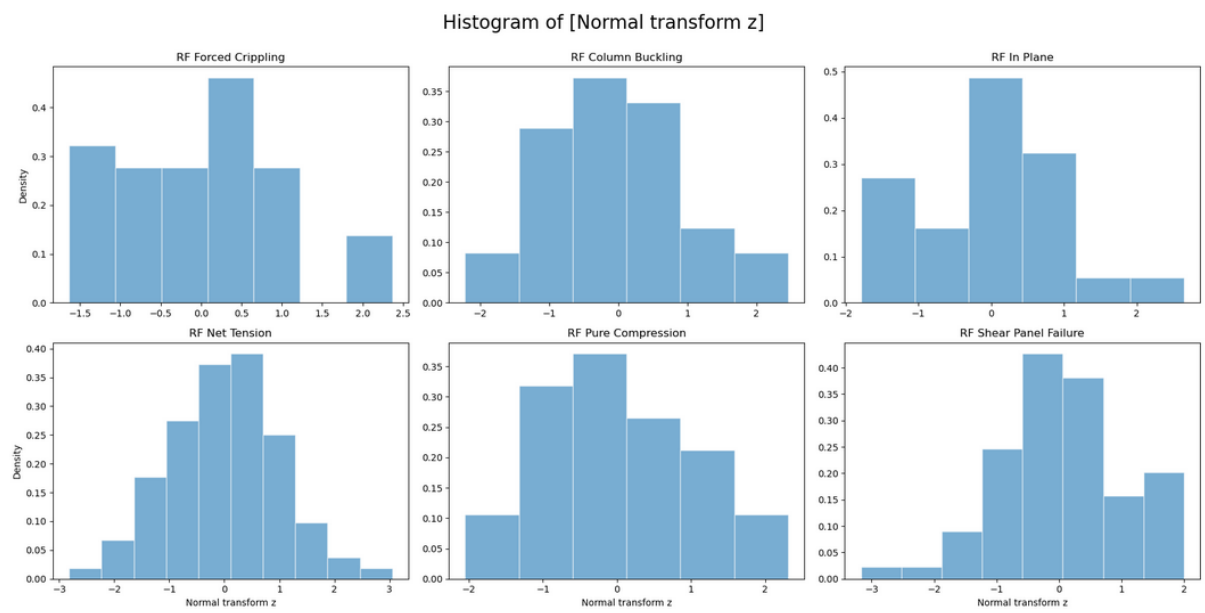


Figure 1.16: (Binned) histograms depicting the distribution of the variable $z = \gamma + \sinh \frac{e-\xi}{\lambda}$, where $e \sim JohnsonSU(\gamma, \delta, \xi, \lambda)$ is the sampled residue. It can be shown that z converges to a normal distribution[26].

do not properly fit the MS-18 error distribution (when using an industrial-sized dataset, not the one employed for illustration here), and we've had to rely on the (rather exotic) JohnsonSU

Table 1.9: Outlier detection taking $e \sim JohnsonSU$ as H_0 . N.B. for this table the usual requirements for classifying a point as an outlier ($z \in \sigma \pm 3\mu$ for the z-score and significance $1 - a \geq 95\%$ for the gESD) have been softened here for illustration purposes to $z \in \sigma \pm 1.2\mu$ and $a = 0.45$ for both tests, respectively.

	Outliers assuming JohnsonSU distribution					
	RF Forced Crippling	RF Column Buckling	RF In Plane	RF Net Tension	RF Pure Compression	RF Shear Panel Failure
st.normaltest pvalue	0.64	0.86	0.44	0.76	0.95	0.44
Total number of cases	38	31	25	279	26	69
Outliers outside 1.5 stds	5 / 13.16%	4 / 12.90%	3 / 12.00%	36 / 12.90%	4 / 15.38%	8 / 11.59%
Lower bound z=-1.5	-0.04	-0.04	-0.01	-0.03	-0.07	-0.04
Upper bound z=1.5	0.04	0.04	0.03	0.02	0.06	0.04
GESD outliers (a=0.45)	0-25 / 65.79%	0-1 / 3.23%	0-1 / 4.00%	0-270 / 96.77%	0-18 / 69.23%	0-1 / 1.45%
GESD lower bound	0.00	-0.09	-0.02	0.00	0.01	-0.10
GESD upper bound	0.01	0.04	0.04	0.00	0.02	0.07

distribution. Without a parametrized distribution that properly fits the error, an uncertainty model cannot be computed. Recall building an accurate uncertainty model is the main motivation for this section. Computing empirical statistics of the empirical distribution of the residue (obtained from test set points) is possible, but assuming the empirical statistics are the same than the true, theoretical ones is not possible. To solve this obstacle, an alternative method for calculating informative statistics of the error's distribution that do not rely on knowing the parametrized analytic expression of it is therefore needed. The method provided here is known as non-parametric bootstrapping[28] and the main concept behind it is showed in [algorithm 2](#).

This algorithm:

1. Samples N points with replacement from the original population S . N.B. replacement makes the new and the original populations (possibly) different.
2. Statistic x is calculated in the new population.

3. Steps 1 and 2 are repeated $M \gg 1$ times, giving a collection of x 's (called X).
4. If M is sufficiently large, X converges to a Gaussian population. The bootstrapped CI for the statistic x with a 95% confidence is bounded by the percentiles 2.5% and 97.5% of X .

Algorithm 2: Non-parametric bootstrapping

Data: Population $S = \{S_1, S_2, \dots, S_N\}$ with unknown PDF.

Result: Statistic x 's CI

```

1 Initial ize list:  $CI = [0]_{1 \times 2}$ ;
2 Initialize list:  $X = [0]_{1 \times M}$ ;
3 for  $i = 1, \dots, M \gg 1$  do
4    $S_i \leftarrow C_S(N, N)$ ;
5    $X(i) \leftarrow x_{S_i}$ ;
6 end
7  $CI(1) \leftarrow P_X^{2.5\%}$ ;
8  $CI(2) \leftarrow P_X^{97.5\%}$ ;
```

Some informative statistics of the error distribution are given in [Table 1.10](#). The statistics are computed twice, once in the empirical distribution of $P(e)$ sampled from the outputs of $\mathcal{S}^{\text{test}}$, and the other one in the form of bootstrapped CIs.

To better understand the utility of $P(e)$ for building an uncertainty model, the simple idea behind these models is presented here, although it is further discussed in [section 1.7](#).

In [Table 1.11](#), some quantiles of the error distribution are presented. For reference, they are computed as empirical statistics of the empirical error distribution, and using bootstrapping (in this case their confidence intervals are given instead). The simplest uncertainty model which can be built with this information assumes that, for future samples of the residue, the quantiles of [Table 1.11](#) will still hold true (*i.e.*, the empirical and the theoretical quantiles coincide). For instance, we would assume that, according to [Table 1.11](#), for future samples the error of variable "RF Forced Crippling" will belong to the interval $[-0.0432, 0.0448]$ (defined by percentiles 5th and 95th) with a frequency equal to 90%. If we wanted to soften the assumption that the empirical and the theoretical quantiles are the same, we could use the bootstrapped quantiles instead. That way, with a 95% confidence we could claim that the error of "RF Forced Crippling" variable will belong to $[-0.0548, 0.0586]$ with a frequency of 90% as a minimum, given that we now from bootstrapping that, with a 95% confidence, the true 5th quantile belongs to the range $[-0.0548, -0.0353]$ and the true 95th quantile belongs to $[0.0379, 0.0586]$.

Of course, the uncertainty model described in the last paragraph can be fine-tuned using additional information about the error distribution. If we found $P(e)$ to be heteroscedastic, we could benefit from conditioning our uncertainty model to certain regions of the input (or the output) space. This is the main motivation for section 1.5, section 1.6 and section 1.7.

Table 1.10: Summary of bootstrapped error statistics. For the median, the Wilson-score[29] is used for computing the confidence interval.

Confidence level at 95%. BS=Confidence Interval (percentile bootstrap), WS=CI (wilson-score)										
	count	min	mean	(BS) mean	(WS) median	std (BS) std	IQR (BS) IQR	kurtosis (BS)	skewness (BS)	skewness max
RF Forced Crippling	383	-0.15	0.0032	0.0062	0.0041	0.0068	0.034	0.039	0.035	14. 24. 2.7 1.4 3.1 -0.74 0.28
RF Column Buckling	319	-0.12	0.0027	0.0061	0.0014	0.0047	0.031	0.034	0.035	2.7 3.8 1.6 0.22 0.81 -0.33 0.12
RF In Plane	252	-0.08	0.0020	0.0059	0.00065	0.0028	0.027	0.031	0.030	5.0 8.3 0.84 1.1 1.9 0.13 0.16
RF Net Tension	2794	-0.18	-0.0026	-0.0019	-0.0028	-0.0022	0.018	0.02	0.016	17. 25. 6.2 0.72 2.0 -0.75 0.21
RF Pure Compression	265	-0.27	0.0019	0.0073	0.0040	0.0077	0.041	0.052	0.034	15. 21. 5.1 -0.31 2.4 -2.9 0.26
RF Shear Panel Failure	695	-0.31	0.0038	0.0081	0.00073	0.0026	0.053	0.067	0.031	44. 63. 20. 4.0 5.9 0.037 0.61

Table 1.11: Bootstrapped percentiles (1st, 5th, 10th, 90th, 95th and 99th) of the residue distribution, calculated with a 95% confidence interval using Wilson-score.

Confidence level at 95%. BS=Confidence Interval (percentile bootstrap), WS=CI (wilson-score)														
	1%	(WS) 1%	5%	(WS) 5%	10%	(WS) 10%	median	(WS) median	90%	(WS) 90%	95%	(WS) 95%	99%	(WS) 99%
RF Forced Crippling	-0.0834	-0.0712	-0.0432	-0.0353	-0.0286	-0.0253	0.00405	0.00676	0.0309	0.0389	0.0448	0.0586	0.101	0.147
	-0.115	-0.0548	-0.0361	-0.0361	-0.0361	-0.0361	0.0000785	0.027	0.027	0.027	0.0379	0.0379	0.0379	0.0768
RF Column Buckling	-0.0605	-0.0441	-0.0337	-0.0283	-0.0246	-0.0246	0.00139	0.00472	0.0362	0.0453	0.0582	0.0656	0.100	0.113
	-0.111	-0.0509	-0.0373	-0.0373	-0.0373	-0.0373	-0.00138	-0.00138	-0.0297	-0.0297	-0.0442	-0.0442	0.0442	0.0686
RF In Plane	-0.0586	-0.0449	-0.0386	-0.0306	-0.0284	-0.0203	0.000646	0.00281	0.0310	0.0418	0.0481	0.0664	0.0747	0.158
	-0.0798	-0.0449	-0.0337	-0.0337	-0.0337	-0.0337	-0.00220	-0.00220	0.0233	0.0233	0.0355	0.0355	0.0355	0.0664
RF Net Tension	-0.0506	-0.0444	-0.0277	-0.0198	-0.0187	-0.0187	-0.00280	-0.00280	0.0148	0.0158	0.0231	0.0250	0.0514	0.0596
	-0.0633	-0.0298	-0.0298	-0.0213	-0.0213	-0.0213	-0.00329	-0.00329	0.0135	0.0135	0.0211	0.0211	0.0211	0.0437
RF Pure Compression	-0.118	-0.0549	-0.0428	-0.0352	-0.0289	-0.0244	0.00400	0.00772	0.0314	0.0407	0.0521	0.0715	0.109	0.259
	-0.267	-0.074	-0.074	-0.0389	-0.0389	-0.0389	0.00124	0.00124	0.0258	0.0258	0.0369	0.0369	0.0369	0.0683
RF Shear Panel Failure	-0.0775	-0.0498	-0.0392	-0.0307	-0.0258	-0.0258	0.000728	0.00259	0.0376	0.0445	0.0572	0.0696	0.197	0.316
	-0.123	-0.0578	-0.0578	-0.0361	-0.0361	-0.0361	-0.00108	-0.00108	0.0299	0.0299	0.0489	0.0489	0.0489	0.0902

1.5 Distributed error quantification: conditioning the error distribution on the input space

This section corresponds to box labelled " $P(E|X)$ " in Figure 1.17. In section 1.4, the marginalised distribution of the residue $P(e)$ was discussed. This section aims at extracting useful information by conditioning the error distribution to the input variables' space, which mathematically can be denoted by $P(e|X)$. Amongst the motivations for this, we count in the first place that this section will help building our uncertainty model (vid. section 1.7) by refining the methods described in the previous section for uncertainty prediction with new information from $P(e|X)$. Furthermore, model and data boosting (vid. Figure 1.17) can both benefit from the analysis performed in this section. Knowledge of the error distribution conditioned to the input space can help identify those regions where either:

- The dataset is properly representing the region, but model training is deficient.
- Dataset quality is not sufficient for proper training according to the specified performance requirements.

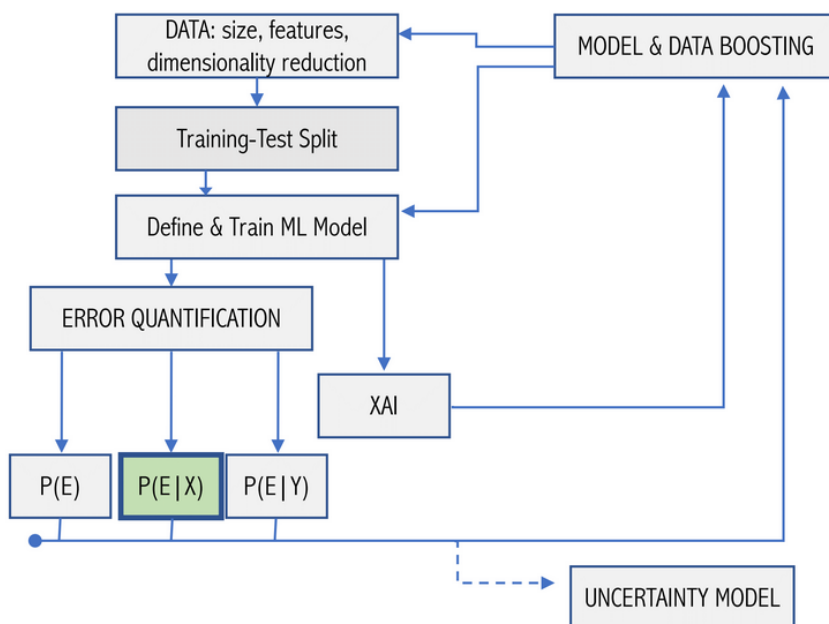


Figure 1.17: Box diagram showing the relative position of section 1.5 in the complete validation pipeline.

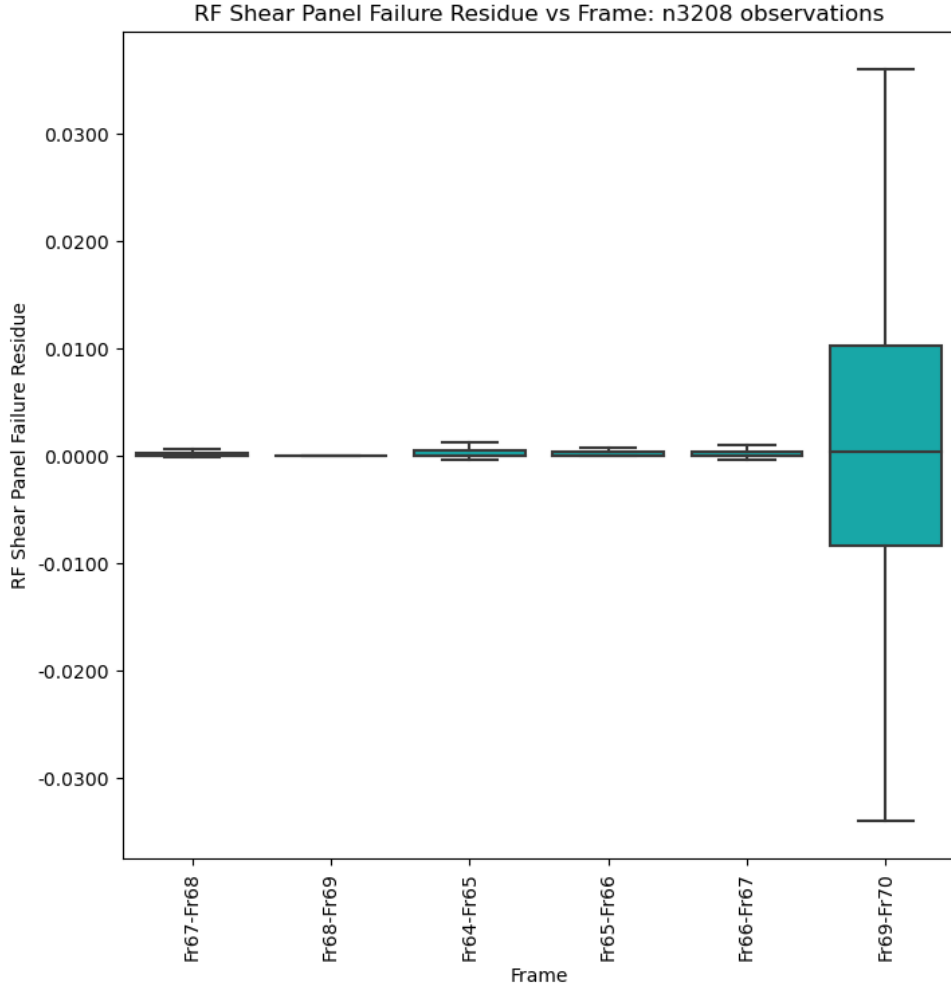
In the first case, training of the model can be reinforced by several means (longer training, hyperparameter tuning, transfer learning, etc.) In the second case, resampling data in deficient regions, or artificial data enhancing techniques such as data augmentation[30] are recommended.

The task of recomposing $P(e|X)$ needs to be addressed in a computationally efficient way, given the input space dimensionality m [recall the input features vector is $\mathbf{X} = (X_1, X_2, \dots, X_m)$] can be very large. For the case of MS-S18, for instance, the input space's dimensionality is $m = 31$ (28 numerical inputs plus 3 categorical). With industrial sized datasets (typically reaching up to millions of data points), recomposing $P(e|X)$ becomes unaffordable. The easiest way of overcoming this issue is by binning the input space according to a certain criteria. If we denote the binned input space by $X^B = \{X_1^B, X_2^B, X_3^B \dots X_r^B\}$ where X_j^B represents a certain bin, and there are a total of r bins, then we can substitute the task of recomposing $P(e|X)$ by that of recomposing $P(e|X^B)$. Although simple, this idea allows for an effective computational cost reduction.

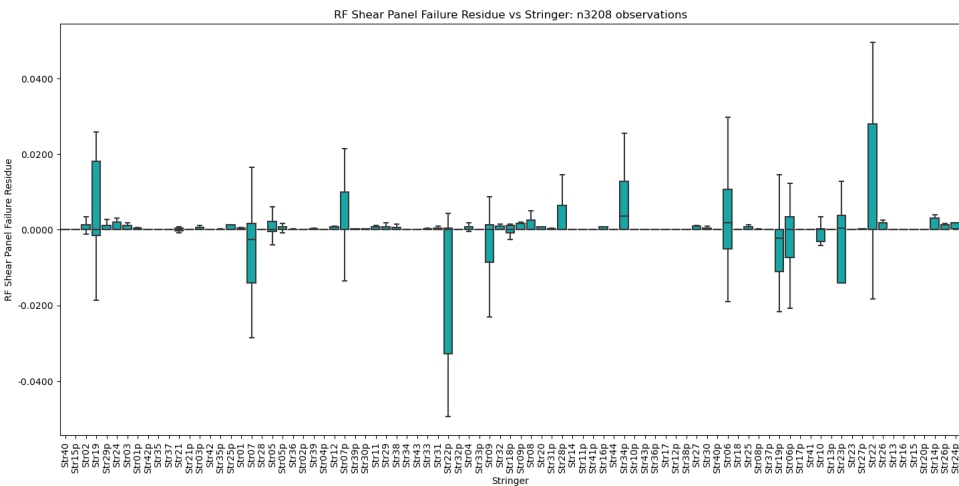
1.5.1 Visualization of error as a function of categorical (discrete) input variables

The immediate criteria for binning the input space is using categorical variables. These variables do in essence bin the input space as they can only take certain (or rather discrete) values. As previously mentioned, for MS-S18 there are three categorical variables enclosing geometrical information: "Frame", "Stringer", and "dp". [Figure 1.18](#) plots, for each categorical input variable, a box plot of the error as a function of the category.

The box plot layout reports the median, Inter-quantile Range and whiskers. Outliers showing anomalous dispersion of the residue could indicate geometrical configurations (*e.g.* the one defined by frames no. 69-70 and stringer no. 26) where training has been inefficient. The engineer in charge could inspect this zone and conclude, for instance, that the physics at play in that region involve exploding gradients which induce strong non-linearities.



(a) Error conditioned to the categorical variable "Frame"



(b) Error conditioned to the categorical variable "Stringer"

Figure 1.18: Box and whisker plots depicting the residue conditioned to two different categorical variables. Figure 1.18(a): "Frame". Figure 1.18(b): "Stringer". Clearly, outliers can be appreciated in both cases ("Fr69-Fr70" in Figure 1.18(a), and various stringers in Figure 1.18(b)).

1.5.2 Bias detection and quantification (1D)

After the visual inspection carried out in Figure 1.18, a statistical test is needed to actually check whether the observed residue for some frames or stringers is unexpected enough to be considered an "outlier". This is, we need to check whether anomalies shown in Figure 1.18 actually are statistically significant or not. To this end, the following procedure is proposed:

A. Detection of error bias in single categories (ANOVA)

The initial method of choice to detect whether a given input categorical variable shows any bias is the one-way ANOVA test[31]. This method consists on the following steps⁵:

- We fix a categorical variable i under analysis.
- The method scatter-plots the residual error versus the category of x^i , for all n samples of the test set.
- ANOVA makes then an hypothesis test, where the null hypothesis H_0 is that the mean of the (theoretical distribution) error for each of the categories is the same. The ANOVA test rejects H_0 with a certain confidence if the p -value of the test is smaller than a certain level.
- The output of the method is just the p -value, if this is smaller than 0.05, then H_0 is rejected at 95% confidence and we say that the categorical variable x^i shows bias.

In Table 1.12, results of the ANOVA test from MS-S18 are shown. The test shows bias in all the three categorical input variables, but for different output variables each one.

⁵N.B. ANOVA in principle requires data in each category to be normally distributed and homoscedasticity (variances in different categories are similar, cfr.[21, p. 374]). It is important to remark these conditions are sometimes not met.

Table 1.12: P-values results from the one-way ANOVA test. The red labelled cells show that variable "dp" shows bias for the residual distribution of "RF Net Tension", as well as variable "Frame" for the residual distribution of "RF Forced Crippling" and variable "Stringer" for the residual distributions of "RF Net Tension" and "RF Pure Compression". For the rest of the table, p-values greater than 0.05 indicate that H_0 cannot be rejected with a statistical confidence of at least 95%.

1-way ANOVA (p-value)						
	RF Forced Crippling	RF Column Buckling	RF In Plane	RF Net Tension	RF Pure Compression	RF Shear Panel Failure
dp	0.60142	0.35218	0.86072	0.00000	0.68189	0.90204
Frame	0.02972	0.69550	0.24502	0.22363	0.39069	0.59135
Stringer	0.32703	0.24055	0.28428	0.00062	0.04613	0.83613

B. Quantification of error bias in single categories test no. 1: based on error mean outlier

This analysis is to be done only if results from the one-way ANOVA test show bias in at least one categorical variable. Under this assumption, the former test has identified a number of categorical variables that show bias. Here we quantify such bias by checking whether there are certain categories which are "outliers", *i.e.* categories where the error mean is substantially different than for the rest of categories. We check this using z-score[32], which consists on the following steps: we initially construct the mean error e in each category. If the categorical variable has s categories, then we have a vector (e_1, e_2, \dots, e_s) . We then z-score this vector to build

$$\left(\frac{e_1 - \langle e \rangle}{\sigma(e)}, \frac{e_2 - \langle e \rangle}{\sigma(e)}, \dots, \frac{e_s - \langle e \rangle}{\sigma(e)} \right),$$

where

$$\langle e \rangle = \frac{1}{s} \sum_{i=1}^s e_i; \quad \sigma(e) = \sqrt{\frac{1}{s} \sum_{i=1}^s (e_i - \langle e \rangle)^2}$$

We make use of the rule of thumb that category i shows **weak bias** if

$$1 < \frac{|e_i - \langle e \rangle|}{\sigma(e)} \leq 3,$$

whereas category i shows **strong bias** if

$$\frac{|e_i - \langle e \rangle|}{\sigma(e)} > 3.$$

The test output is shown in Table 1.13, where for each categorical variable that was previously identified as having bias, a sub-table showing **only** the specific categories that either show weak or strong bias is displayed.

Table 1.13: Z-score results for biased categorical variables. One table is generated for each pair biased categorical input variable-output variable.

Frame with RF Forced Crippling as output			dp with RF Net Tension as output				
		Fr66-Fr67	Fr69-Fr70			0.000000	0.900000
N	4	1	N	15	2		
mean	-0.014281	0.008480	mean	0.004450	-0.005974		
Z score	1.174359	1.770030	Z score	1.000000	1.000000		
Bias	Weak	Weak	Bias	Weak	Weak		

Stringer with RF Net Tension as output					Stringer with RF Pure Compression as output	
		Str06	Str06p	Str31	Str39	Str07
N	1	2	1	1	N	1
mean	-0.022004	0.028592	-0.026716	0.035710	mean	0.178702
Z score	1.225013	1.331218	1.463067	1.690886	Z score	3.086849
Bias	Weak	Weak	Weak	Weak	Bias	Strong

C. Quantification of error bias in single categories test no. 2: based on error variance outlier

This analysis is to be done only if results from the one-way ANOVA test show bias is found in at least one categorical variable.

The procedure is similar as before, but here we investigate whether for certain categories the dispersion (not the mean) of the samples in a given category is substantially different than for the rest of categories. For instance, experience in MSP-S18 suggests that the main source of error bias in categorical variables comes from the fact that different categories have different variance. This is quantified by doing a z-score analysis on category variances: if the categorical variable under analysis has s categories, then we have a vector of variances (v_1, v_2, \dots, v_s) , where

v_i is the variance of the error for all samples in category i . We then z-score this vector to build

$$\left(\frac{v_1 - \langle v \rangle}{\sigma(v)}, \frac{v_2 - \langle v \rangle}{\sigma(v)}, \dots, \frac{v_s - \langle v \rangle}{\sigma(v)} \right),$$

where

$$\langle v \rangle = \frac{1}{s} \sum_{i=1}^s v_i; \quad \sigma(v) = \sqrt{\frac{1}{s} \sum_{i=1}^s (v_i - \langle v \rangle)^2}$$

We make use of the rule of thumb that category i shows ***weak variance bias*** if

$$1 < \frac{|v_i - \langle v \rangle|}{\sigma(v)} \leq 3,$$

whereas category i shows ***strong variance bias*** if

$$\frac{|v_i - \langle v \rangle|}{\sigma(v)} > 3$$

The analysis outputs, for each categorical variable that was previously identified as having bias, a table showing only the specific categories that either show weak or strong bias according to this second method.

D. Quantification of error bias in single categories test no. 3: based on identification of linear trend

This test is only applicable to categorical variables for which specific categories have a natural ordering (mathematically, we say there is a canonical geometric embedding for the categorical variable). Such identification needs to be done "by hand" by the engineer in charge.

Such embedding exists when the categorical variable is related for instance to a geometrical location in the plane (for instance the Frames and Stringers are categorical –in so far they are discrete– but they correspond to regions of the plane along a Cartesian and a radial axis, so there is a natural ordering). In those cases, it makes sense to investigate linear trends as these are interpretable.

The method just proceeds to fit a linear model (with just one explanatory variable). If the slope is above a certain threshold and if the fit is good, then we can be confident the linear trend is genuine, and the slope can be used to quantify the linear bias and as a source for uncertainty.

For each categorical variable that has a natural ordering and was previously detected as having bias, the test fits a linear model and outputs the result of this model.

If such model has a slope (statistically) significantly different from zero, then this categorical variable is flagged as having a linear trend.

Illustration of this test is provided in Figure 1.19.

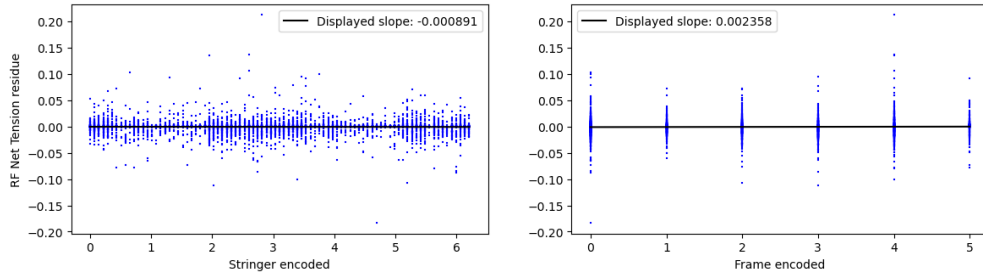


Figure 1.19: Quantification of linear trend for input categorical variables "Stringer" (left) and "Frame" (right). Variables have been numerically encoded following a logical order (*e.g.* in the right image, six integers in the x axis represent the six possible values of variable Frame). The residue of output variable "RF Net Tension" has been plotted against the categorical variable (y axis). In this case, no linear trend is appreciated in neither of the two input variables (no bias present).

1.5.3 Bias detection and quantification (2D)

In the previous section we considered the specific effect (bias) of individual input variables on the error. However, it can be the case that such bias is enhanced when groups of input variables are considered together. The method of choice to analyze whether two independent (input) categorical variables have an effect on the error means is the 2-way ANOVA test[33]. In general the method is not very informative except when the combination of input variables is itself interpretable. This usually requires the external feedback of the engineer. For instance, the engineer can know a priori that certain combination of input variables play a synergistic role, go together, etc. For instance, in MSP-S18, the categorical variables **Frame** and **Stringer** are geometric locations and thus, together, provide a location of the specific region of the plane that the configuration analyses. One can thus perform a 2-way ANOVA to analyze the presence of bias accordingly. If such bias exists, then bias quantification tests described in subsection 1.5.2 can be applied.

A. Bias detection (2D)

For the pair of (previously chosen) categorical variables, the test performs 2-way ANOVA as described above and outputs the p -value. If this p -value is smaller than 0.05, we conclude that

there exists bias at 95% confidence.

B. Bias quantification (2D)

Suppose we have two categorical variables A and B , where A has q categories $A = (A_1, A_2, \dots, A_q)$ and B has r categories $B = (B_1, B_2, \dots, B_r)$. Suppose also that a 2-way ANOVA concluded that the error is biased on the combined effect of A and B . We then can build all the pairs (A_i, B_j) and interpret each of them as a single category of this "block categorical variable", *i.e.* we have now qr categories. We can subsequently apply the bias quantification tests 1 and 2 described above, applied to the "block categorical variable".

- If bias has been detected, the "block categorical variable" with qr categories is built and a table with qr columns and 2 rows is defined (for test no. 1 and test no. 2 results).
- Bias quantification test no. 1 (error mean, see above) is performed on the block categorical variable, and fills up in the table the first row for those columns that show either weak or strong bias.
- Bias quantification test no. 2 (error variance, see above) is performed on the block categorical variable, and fills up in the table the second row for those columns that show either weak or strong bias.

Results from this tests are illustrated in [Table 1.14](#).

Table 1.14: 2D bias quantification: Results from mean and variance z -score tests on biased Stringer-Frame input pairs (bias detection has been performed through 1-way ANOVA). For the input value combinations showed in the columns, either mean or variance (or both) show bias (weak: z -score < 3 . Strong: z -score > 3). For the combination of Frame Fr67-Fr69 and Stringer Str07, there are not enough test points to compute the z -score variance test.

	Fr64-Fr65:Str38	Fr67-Fr68:Str07
# samples	2	1
1-way ANOVA - ZScore(mean)	Weak	Weak
1-way ANOVA - ZScore(var)	Strong	-

1.5.4 Visualization of error as a function of numerical (continuous) input variables

In this section the same basic analysis is performed as in subsection 1.5.2, although conditioning the error on numerical instead of categorical input variables.

In this section we plot, for each numerical input variable, a scatter plot of the error as a function of the input numerical variable at analysis. From the scatter plot and its linear fit, we expect to (with human intervention) identify bias in the variables which present it, and use visual information for model and data boosting. Illustrative results of two input variables are given in Figure 1.20.

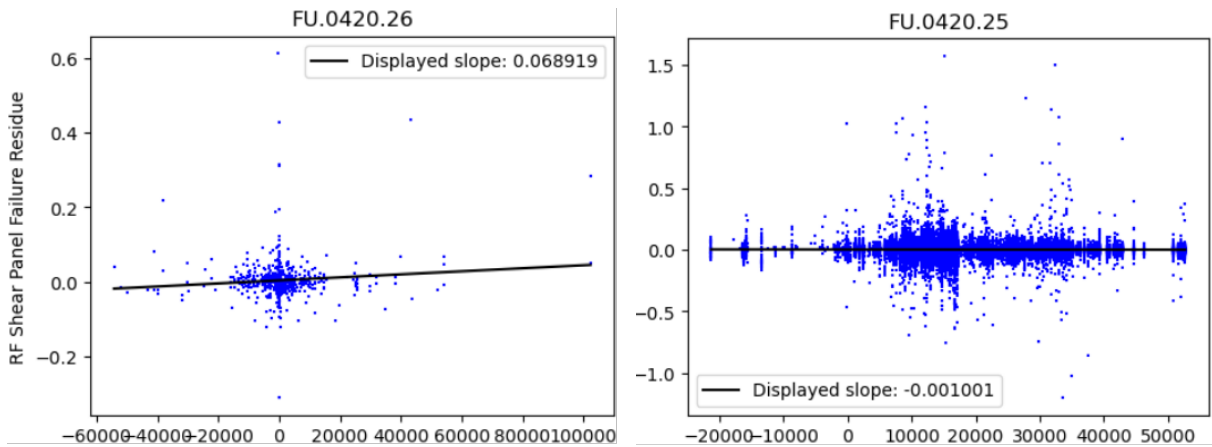


Figure 1.20: Scatter plots of residue against a particular numerical input variable. Left: Input var. FU.0420.26. A linear trend is appreciated, suggesting the model makes worse predictions as input load "FU.0420.26" is larger. Right: input var. FU.0420.25. No linear trend is appreciated, although severe heteroscedasticity can be observed. Note the vertical bar arrangement, showing particular input loads for which dispersion is unusually large. In view of the former results, the engineer may decide to investigate the underlying causes both for the linear trend in the left and for heteroscedasticity on the right. With the information, model and data boosting may be performed. More training data could be decided to be sampled in the range of [20000, 60000] of FU.0420.26, for instance, and some regularization technique could be tried for the loss function in order to penalise inputs triggering high variance observed in the right.

1.5.5 Bias detection and quantification

The goal of this section is to flag statistically significant bias found in output variables, in order to provide mathematical assurance to engineers when interpreting results from Figure 1.20. Similar to categorical variables, we use different tests for bias detection and for bias quantification. As the input variables are now numerical, instead of ANOVA and z-score we use:

A. Detection of linear trends for individual numerical variables

For each input variable, the code fits a linear model that can identify a linear trend of the error as a function of the input variable.

The test outputs (vid. Table 1.15):

- The p -value that accounts for whether such type of bias indeed exists.
- The Pearson correlation coefficient.
- The slope of the best linear model fit.

Table 1.15: Bias detection and quantification on numerical input variables (the results for just five input variables are shown here – in columns–): P-value (statistical significance of the hypothesis that the variable is biased), Pearson coefficient, and slope of the best linear fit are shown in the first three rows. The last row shows the message "Biased" in case the p -value > 0.05 , "NO" otherwise. Data from this table corresponds to residue of the output variable "RF Column Buckling". Analogous tables exist for the rest of the output variables.

FACTORS	FU.0410.14	FU.0410.15	FU.0410.16	FU.0410.24
p-value	0.600663	0.625659	0.037808	0.480859
Pearson coeff.	0.029417	0.027417	-0.116347	-0.039608
Slope (normalized)	0.013192	0.027099	-0.141826	-0.019688
Linear trend	NO	NO	Biased	NO

B. Discretizing continuous variables

The process is to bin each input numerical variable and thus treat them as categorical, so that one can perform one-way ANOVA followed by bias quantification tests no. 1 (mean outlier) and test no. 2 (variance outlier) former discussed. By default the number of bins is equal to 10.

For each input variable:

- The input variable is binned.
- The steps depicted in sections subsection 1.5.2 are applied.

Results are shown in Table 1.16, Table 1.17 and Table 1.18.

Table 1.16: 1-way ANOVA test results (p-values) for binned numerical input variables. For the output variable "RF Forced Crippling", bias is found in the input variables "FU.0420.25" and "FU.0430.25". Similarly, for the output variable "RF Net Tension", bias is found in the input variable "FU.0430.15".

	1-way ANOVA (p-value)					
	RF Forced Crippling	RF Column Buckling	RF In Plane	RF Net Tension	RF Pure Compression	RF Shear Panel Failure
factors_binned	0.36995	0.57707	0.16276	0.32759	0.72817	0.67178
FU.0410.14_binned	0.14541	0.60928	0.47117	0.86966	0.16037	0.72052
FU.0410.15_binned	0.47235	0.07028	0.23893	0.19848	0.69785	0.36203
FU.0410.16_binned	0.99209	0.29325	0.30693	0.59764	0.86850	0.11857
FU.0410.24_binned	0.28251	0.37036	0.06887	0.30212	0.50172	0.10088
FU.0410.25_binned	0.84519	0.27807	0.35407	0.71585	0.99200	0.10885
FU.0410.26_binned	0.97916	0.23816	0.63145	0.18726	0.59593	0.54611
FU.0420.14_binned	0.11827	0.54753	0.44448	0.69463	0.13006	0.87985
FU.0420.15_binned	0.27700	0.05152	0.19852	0.27864	0.86905	0.30744
FU.0420.16_binned	0.96355	0.29429	0.34697	0.53042	0.88578	0.10234
FU.0420.24_binned	0.28161	0.36135	0.06327	0.32091	0.60557	0.12283
FU.0420.25_binned	0.03686	0.09300	0.46097	0.78027	0.13730	0.83867
FU.0420.26_binned	0.56289	0.15438	0.85899	0.28868	0.77835	0.78597
FU.0430.14_binned	0.20706	0.64043	0.65843	0.16471	0.25147	0.57201
FU.0430.15_binned	0.34776	0.20721	0.70087	0.01776	0.68061	0.87189
FU.0430.16_binned	0.29934	0.05751	0.33328	0.78752	0.76107	0.21693
FU.0430.24_binned	0.50895	0.18564	0.79205	0.09649	0.68746	0.90018
FU.0430.25_binned	0.03176	0.07608	0.30233	0.82106	0.70637	0.73546
FU.0430.26_binned	0.75006	0.18252	0.25337	0.45661	0.99750	0.39317

Table 1.17: Bias quantification in binned FU.0430.15 input variable. Columns represents bins showing bias. The same quantification methods employed for categorical variables (z-score for mean and variance outlier detection) have been used.

FU.0430.15_binned with RF Net Tension as output				
	3	4	8	9
N	269	284	281	299
mean	-0.003908	-0.005275	-0.001238	-0.001153
Z score	1.004073	2.079140	1.096293	1.163220
Bias	Weak	Weak	Weak	Weak

Table 1.18: Summary of binned input variables bias quantification after binning the numerical variables and performing one-way ANOVA and z-score tests to every bin.

RF Forced Crippling		
FU.0420.25_binned		FU.0430.25_binned
1-way ANOVA - ZScore(mean)		Weak
1-way ANOVA - ZScore(var)		Weak
RF Net Tension		
FU.0430.15_binned		
1-way ANOVA - ZScore(mean)		Weak
1-way ANOVA - ZScore(var)		Weak

1.6 Distributed error quantification: conditioning the error distribution on the output space

This section corresponds to box labelled " $P(E|Y)$ " in Figure 1.21.

Figure 1.10 shows an important fact about the error distribution: dispersion is not homogeneous in the full range of the output variables –in the case of MS-S18, all the six Reserve Factors belong in the range (1, 5)–, *i.e.* error is heteroscedastic. This means that the residue is dependent on the prediction of the model, which has important implications in our validation approach. First, some statistical tests rely on the assumption of homoscedasticity. Second and most important, heteroscedasticity is a first indicator which tells us the need to carry out the analysis of the error distribution conditioned on the output space, $P(e|Y)$. Characterising the error in different regions of the output space is the final building block for our complete uncertainty model (vid. section 1.7).

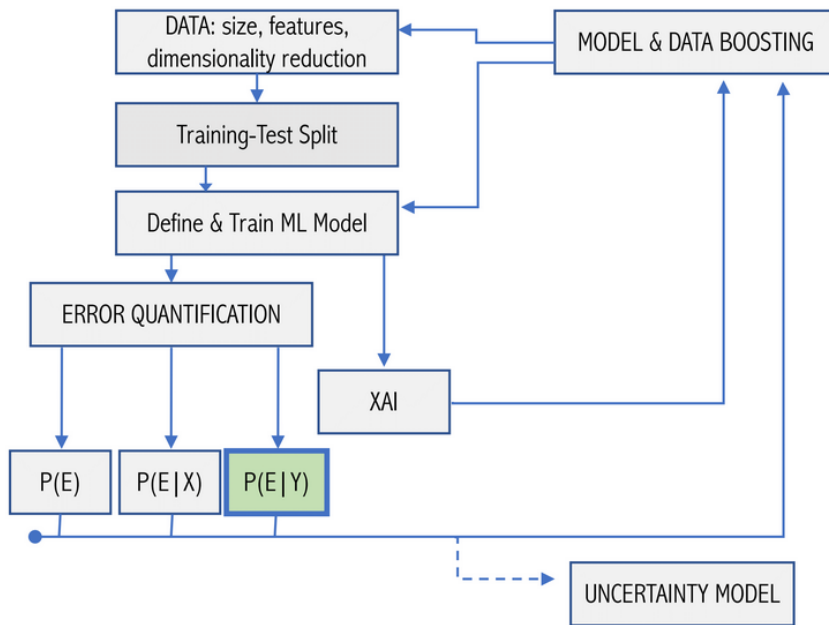


Figure 1.21: Relative position of [section 1.6](#) in the complete validation pipeline.

The first step in the reconstruction of $P(e|Y)$ is to try to fit the error distribution to some well known theoretical distribution. But instead of just repeating what was done in [section 1.4](#), now we add an extra variable to the equation: the prediction of the model \hat{y} . Instead of trying to fit the whole error distribution, we filter the test set by establishing $\hat{y} < \hat{y}_0$ and try to fit the

filtered test set to one of the well known distributions discussed in section 1.4 (Normal, Laplace, Cauchy, JohnsonSU). In Figure 1.22 four of the six output variables –for convenience– of MS-S18 are put under a 1-variable K-S test to assess the goodness of fit of the error to the mentioned distributions. For this figure, the absolute value of the residue has been used instead of the plain residue. We can observe that, while all four theoretical distributions start fitting $P(e)$ when $\hat{y}_0 < 1.5$, soon the p-value drops down indicating a mismatch between the empirical error and Cauchy, Laplace, and Normal distributions. Only the JohnsonSU remains a good fit, but finally diverges as well when $\hat{y}_0 \approx 3$. The conclusion is that only the JohnsonSU distribution is found to be a good match for $P(e|Y)$, but only when filtering the test set up to moderate values of \hat{y}_0 . This suggests presence of extreme phenomena in the error distribution, which in fact is in accordance with the heteroscedastic behaviour observed in Figure 1.10, showing dispersion increases with the output \hat{y} .

By filtering the test set using a maximum allowable value of predictions \hat{y}_0 , we have reached to interesting conclusions. The question now is, why filtering the test set just the particular way we have done it? The choose was motivated by the intuition from Figure 1.10 that dispersion increases with the prediction value. A logical way of filtering the test set in order to find local information of the error distribution is binning it. For the next part, we bin the test set in 10 bins according to their output values, as described in Table 1.19.

For each bin, a 2-sample K-S test comparing the true against the predicted distribution is performed. Such test is only performed if the number of points inside each bin is greater than a minimum threshold (set at 30 points). Results (only four output variables are displayed for convenience) are shown in Figure 1.23. There we can see a clear tendency: while for low output values the two distributions conform well, the p-value eventually drops for higher bins. This confirms the information of Figure 1.10 and Figure 1.22 that the model predicts very well when the output is in the low range, while it has more difficulties predicting higher Reserve Factors. This idea is reinforced by looking at Figure 1.24, where violin plots of the residue for every bin have been plotted. In this figure, it can be clearly appreciated that the (absolute) residue dispersion is dependent with the model’s prediction, growing as \hat{y} does so. As previously discussed, this is the desired behaviour, as low RF indicate high failure risk, whereas high reserve factors indicate low risks. It is therefore preferable to accumulate variance at the low RF extreme of the spectrum.

In Figure 1.25 the error distribution of each individual bin is put under a K-S test to

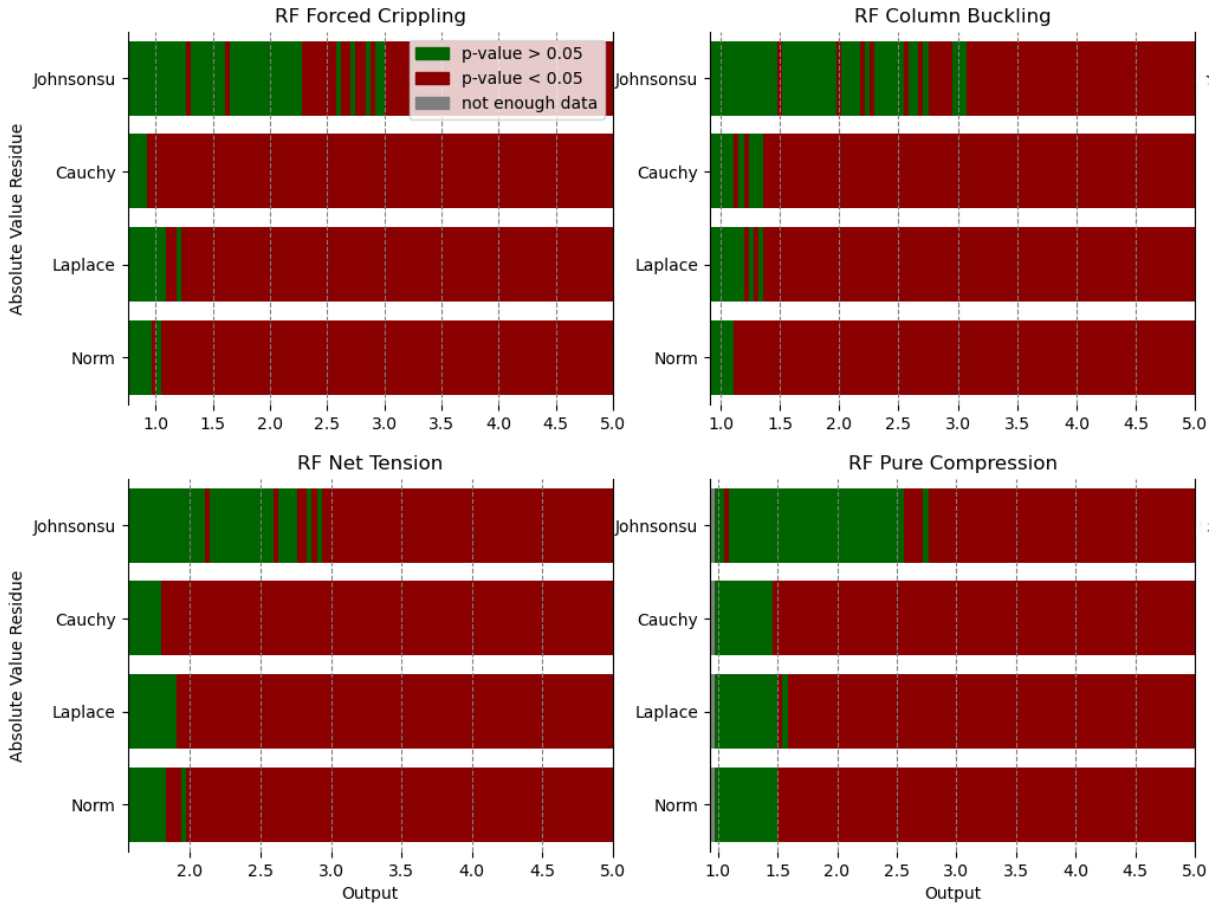


Figure 1.22: Goodness of fit of the error distribution (test set previously filtered) to some parametrised distributions. The test is performed individually for the output variables (Reserve Factors) displayed on top of each image. The goodness of fit is assessed with a 1-variable K-S test. The test set is filtered using the x axis, rejecting every point whose output \hat{y} is larger than x . If the p-value resulting from the K-S test in the filtered test set is greater than 0.05, the vertical slice at position x is labelled green (red if $p\text{-value} < 0.05$, grey if less than a threshold number of points –namely, 30– are present in the filtered test set).

assess the goodness of fit to one of the aforementioned theoretical distributions. Results show similar conclusions to Figure 1.22: only the JohnsonSU makes a good match, even though the p -value drops to under 0.05 for certain bins (note the last bin never passes the test).

Finally, we conclude by pointing out that the binned output space can be subject to the same bias detection and quantification tests (1-way ANOVA, z -score for median, z score for variance, linear fit) which were discussed in subsection 1.5.2 for categorical input (and binned numerical) variables.

Table 1.19: Binnarization of the test set. The test set has been divided into ten bins according to output values. Extremes of the six intervals –one for each Reserve Factor– defining the bins are shown below.

	Bins limits									
	Bin 1	Bin 2	Bin 3	Bin 4	Bin 5	Bin 6	Bin 7	Bin 8	Bin 9	Bin 10
RF Forced Crippling	(0.754, 1.179)	(1.179, 1.603)	(1.603, 2.028)	(2.028, 2.453)	(2.453, 2.877)	(2.877, 3.302)	(3.302, 3.726)	(3.726, 4.151)	(4.151, 4.575)	(4.575, 5.001)
RF Column Buckling	(0.909, 1.318)	(1.318, 1.727)	(1.727, 2.136)	(2.136, 2.545)	(2.545, 2.954)	(2.954, 3.364)	(3.364, 3.773)	(3.773, 4.182)	(4.182, 4.591)	(4.591, 5.001)
RF In Plane	(2.01, 2.309)	(2.309, 2.608)	(2.608, 2.907)	(2.907, 3.206)	(3.206, 3.505)	(3.505, 3.804)	(3.804, 4.103)	(4.103, 4.402)	(4.402, 4.701)	(4.701, 5.001)
RF Net Tension	(1.556, 1.901)	(1.901, 2.245)	(2.245, 2.589)	(2.589, 2.934)	(2.934, 3.278)	(3.278, 3.622)	(3.622, 3.967)	(3.967, 4.311)	(4.311, 4.656)	(4.656, 5.001)
RF Pure Compression	(0.933, 1.34)	(1.34, 1.747)	(1.747, 2.153)	(2.153, 2.56)	(2.56, 2.967)	(2.967, 3.373)	(3.373, 3.78)	(3.78, 4.187)	(4.187, 4.593)	(4.593, 5.001)
RF Shear Panel Failure	(0.854, 1.269)	(1.269, 1.683)	(1.683, 2.098)	(2.098, 2.512)	(2.512, 2.927)	(2.927, 3.342)	(3.342, 3.756)	(3.756, 4.171)	(4.171, 4.585)	(4.585, 5.001)

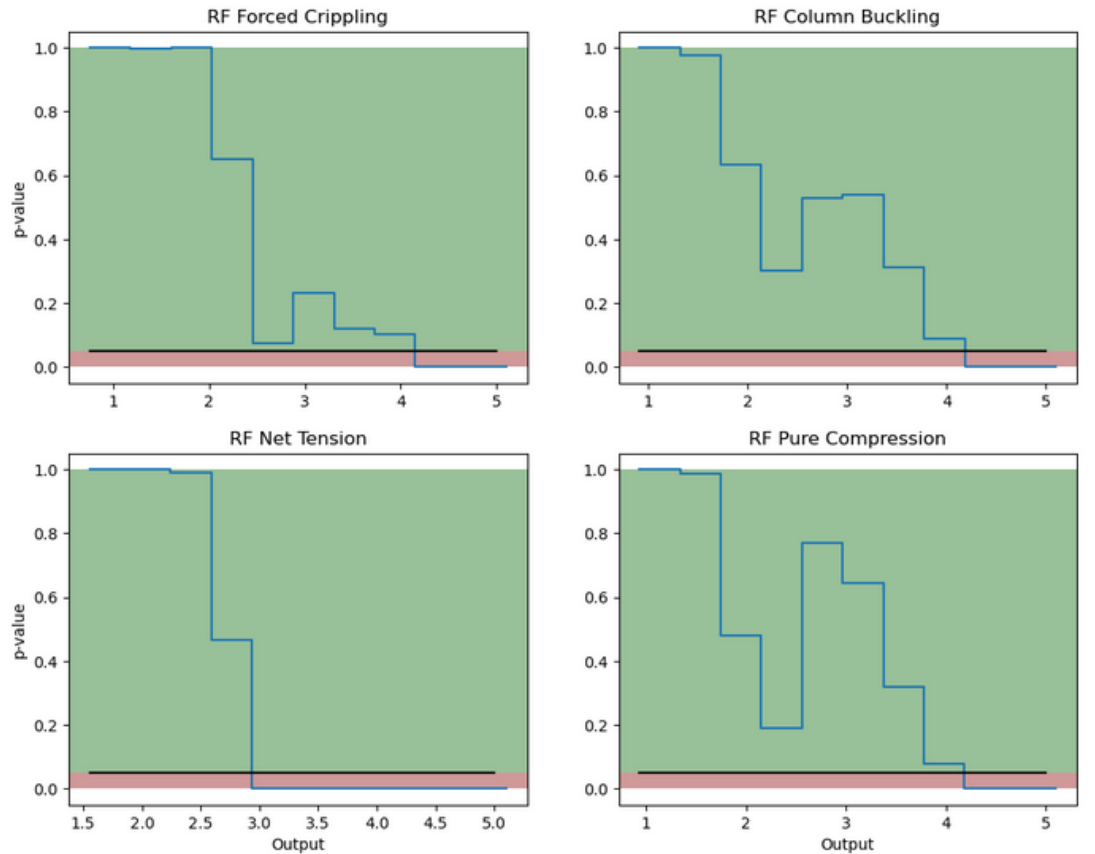


Figure 1.23: Line plot of the p -value from the true-predicted distributions under a 2 sample K-S test. Distribution similarity is rejected if p -value < 0.05 .

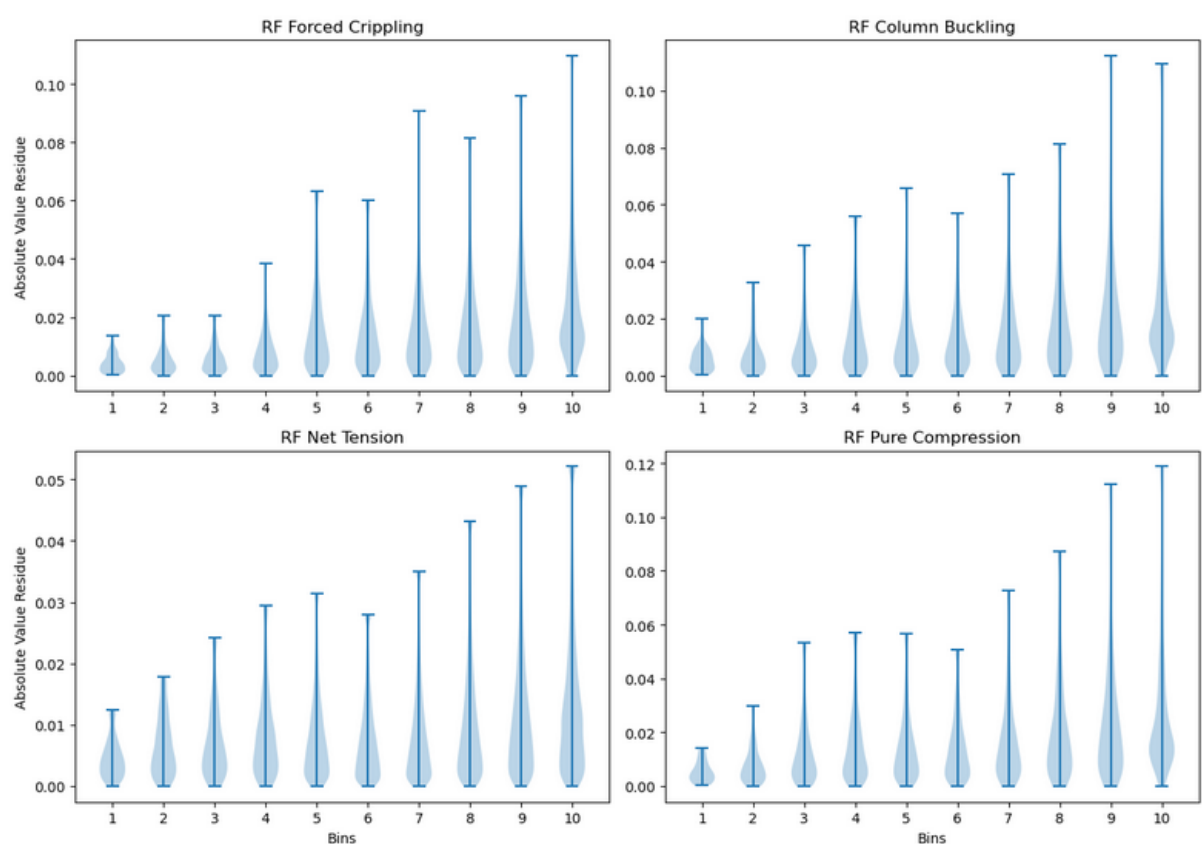


Figure 1.24: Violin plots showing the absolute value residue for every bin.

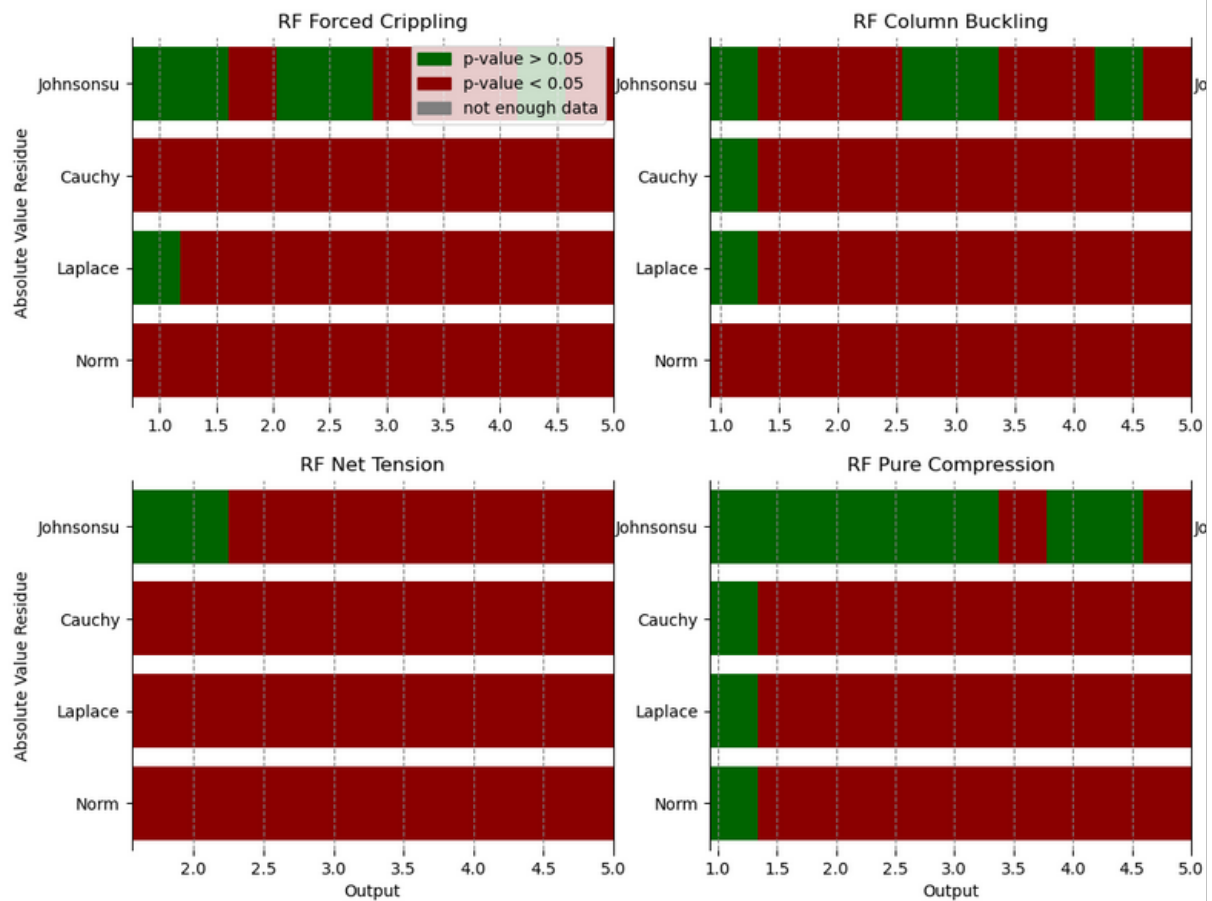


Figure 1.25: Sliced-bar with p-values from the binned error under a K-S test to assess the goodness of fit to several parametrised distributions.

1.7 Uncertainty model

This section corresponds to box labelled "Uncertainty model" in Figure 1.4. It is envisioned with the following question in mind:

Given a new configuration with input parameters $\mathbf{X} = (X_1, X_2, \dots, X_m)$ and prediction $\mathbf{Y} = (Y_1, Y_2, \dots, Y_q)$, where $\mathbf{Y} = F(\mathbf{X})$, what is the expected uncertainty (error) associated to the prediction \mathbf{Y} ?

To the aim of answering this question, the main tasks are:

- To build an **uncertainty model**.
- To **validate** such model.

The expected uncertainty translates into (for instance) $q = 6$ confidence intervals $(CI_1, CI_2, \dots, CI_6)$, such that the k -th predicted reserve factor Y_k has a confidence interval $CI_k = [Y_k^{min}, Y_k^{max}]$. Other types of uncertainty quantifications are possible (standard deviation, credible interval, etc).

Importantly, there are various sources of uncertainty that need to be combined:

1. **Global error distribution** (cfr. section 1.4). This is, the distribution of error in the test set, $P(E)$.
2. **Local-output error distribution** (cfr. section 1.6). This is, the distribution of the error in the test set, conditioned to a specific region of the prediction, $P(E|\mathbf{Y})$.
3. **Local-input error distribution** (cfr. section 1.5). This is, the distribution of the error in the test set, conditioned to a specific region of the input space (error bias characterization), $P(E|\mathbf{X})$.

Our uncertainty model will combine contributing factors (1), (2) and (3) into an effective uncertainty.

Each part (1-3) of the process will need to be **validated**. To this aim, we split the test set into a calibration set \mathcal{E}^{cal} and a test set⁶ $\mathcal{E}^{\text{test}}$ (80/20 random split), estimate the uncertainty

⁶Not to be confused with $\mathcal{S}^{\text{test}}$. Here we denote by "test set" the empirical error distribution sampled from

model on the calibration set and evaluate it by computing its **coverage** (*i.e.* the percentage of configurations whose true output belongs to the confidence interval region) in the test set.

1.7.1 Global uncertainty model based on $P(E)$

After a sanity check that the dataset under analysis (here, the full calibration set) fulfils the minimum size requirements (threshold is set at 300 points for each output variable \mathbf{Y}_i) we proceed with:

A. Global Uncertainty Model (GUM) computation

The interval $[P_{2.5}, P_{97.5}]$ (or in general, the interval $[a, b]$ if other percentiles are chosen) of $P(E)$ is estimated in the calibration set, where the lower bound $P_{2.5}$ and the upper bound $P_{97.5}$ are not raw estimates but the mean of a bootstrap analysis of the lower and upper percentiles respectively. The bootstrapping procedure is implemented as described in [algorithm 3](#). This procedure is repeated for all m output variables. Illustration of the GUM is provided in [Table 1.20](#).

Algorithm 3: Bootstrapped uncertainty CI

Data: Calibration set \mathcal{E}^{cal}
Result: Bootstrapped 95% CI $[P_{2.5}, P_{97.5}]$

- 1 Initialize empty arrays $P_{2.5}$ and $P_{97.5}$;
- 2 **for** $i = 1$ **to** 100 **do**
- 3 Build calibration set i by randomly sampling (with replacement) a total number of points equal to the size of the calibration set;
- 4 Compute lower ($P_{2.5}^{(i)}$) and upper ($P_{97.5}^{(i)}$) percentiles;
- 5 Add $P_{2.5}^{(i)}$ to $P_{2.5}$;
- 6 Add $P_{97.5}^{(i)}$ to $P_{97.5}$;
- 7 **end**
- 8 $P_{2.5_mean} \leftarrow \text{mean}(P_{2.5})$;
- 9 $P_{97.5_mean} \leftarrow \text{mean}(P_{97.5})$;
- 10 **return** $P_{2.5_mean}$ and $P_{97.5_mean}$;

B. Global Uncertainty Model (GUM) evaluation

The (bootstrapped) error coverage is estimated in the test set. This is done by computing the points belonging to $\mathcal{S}^{\text{test}}$.

Table 1.20: Global Uncertainty Model: Confidence Interval (mean and extremes) for output variables "RF Forced Crippling" (left) and "RF Column Buckling" (right). Header showing $[y_{min}, y_{max}]$ in the calibration set.

[0.75, 4.99]		[0.9069, 4.99]	
Mean	0.001859	Mean	0.002292
CI	$[-0.5366, 0.1018]$	CI	$[-0.5339, 0.1076]$

percentage of points in the test set whose error lies inside the chosen uncertainty model. The bootstrap procedure is carried out as described in [algorithm 4](#).

Algorithm 4: Bootstrapped coverage

Data: Uncertainty model (CI), test set $\mathcal{E}^{\text{test}}$
Result: Mean and confidence interval of error coverage

```

1 Initialize empty array error_coverages;
2 for i = 1 to 100 do
3   Build resampled test set i by randomly sampling (with replacement) a total number
     of points equal to the size of the test set;
4   Compute error coverage in resampled test set i;
5   Add error coverage to error_coverages;
6 end
7 Sort error_coverages in increasing order;
8 Calculate mean, 2.5th percentile, and 97.5th percentile of error_coverages;
9 return Mean, 2.5th percentile, and 97.5th percentile;
```

The output is the bootstrap error coverage and its 95% confidence interval. The criteria for a correctly calibrated error coverage is that it is correctly calibrated if $(b-a)\%$ (by default, 95%) lies inside the bootstrapped error coverage confidence interval.

This procedure is repeated for all m output variables. For a graphical interpretation of results, cfr. [Figure 1.26](#). The six GUM's CIs are given in [Table 1.21](#).

Table 1.21: Global Uncertainty Model. The six confidence intervals (bootstrapped) defining the GUM alongside their coverage –in the calibration set– are showed.

Coverage table						
	RF Forced Crippling	RF Column Buckling	RF In Plane	RF Net Tension	RF Pure Compression	RF Shear Panel Failure
Coverage	98.89	99.07	98.92	98.9	99.12	99
CI	[98.61, 99.13]	[98.77, 99.31]	[98.57, 99.21]	[98.8, 98.99]	[98.8, 99.37]	[98.8, 99.17]

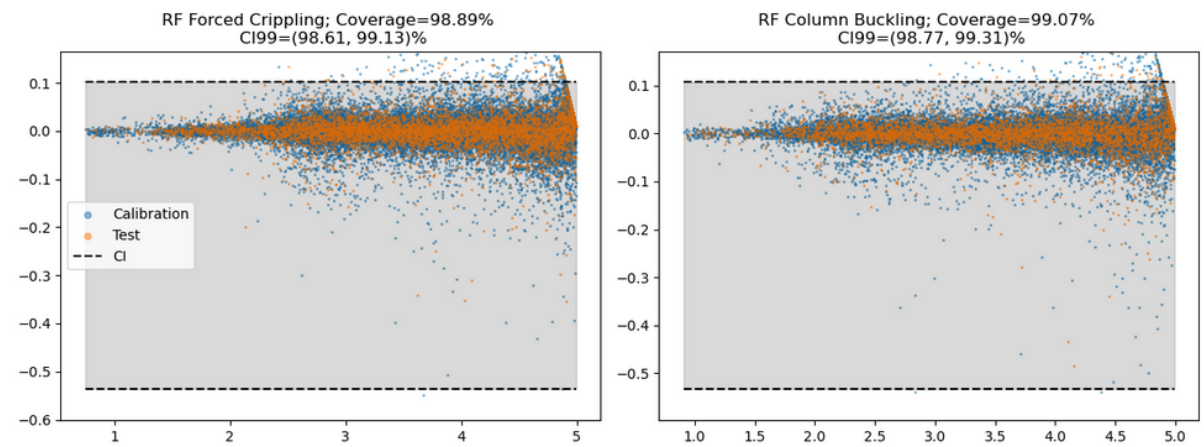


Figure 1.26: Global Uncertainty Model: error coverage. The coverage is higher than 95% for both output variables –for convenience just two output variables are depicted– what means the calibration criteria is successfully met.

1.7.2 Local uncertainty model based on $P(E|\mathbf{Y})$

A. Output variable binning

In order to be able to computationally afford this analysis, the output space \mathbf{Y} must be binned.

In the first place, a scatter plot of the error of each point in the calibration set is plotted for illustration as a function of the true output y_t in Figure 1.27.

The calibration set is then partitioned into a total of equispaced n_{bins} bins according to the range of the true output y_t .

For illustration, a total of n_{bins} violin plots (one per bin, concatenated in a single plot where the "x axis" is the bin number) is plotted in Figure 1.28, where each violin plot describes the error density of the points in the respective bin.

B. Local Output Uncertainty Model (LOUM) computation

First, a sanity check that the number of points in each bin is above a certain threshold (namely, 300 points) assures statistical robustness for this next part.

For those bins for which the minimum-size requirement is not met, the bin is given the Global Uncertainty Model (GUM).

For those bins for which the minimum-size requirement is met, the code computes an uncertainty model in terms of the bootstrap [P2.5, P97.5] (or a general [a,b]) using algorithm 3, and assigns to the bin the resulting local uncertainty model (vid. Table 1.22).

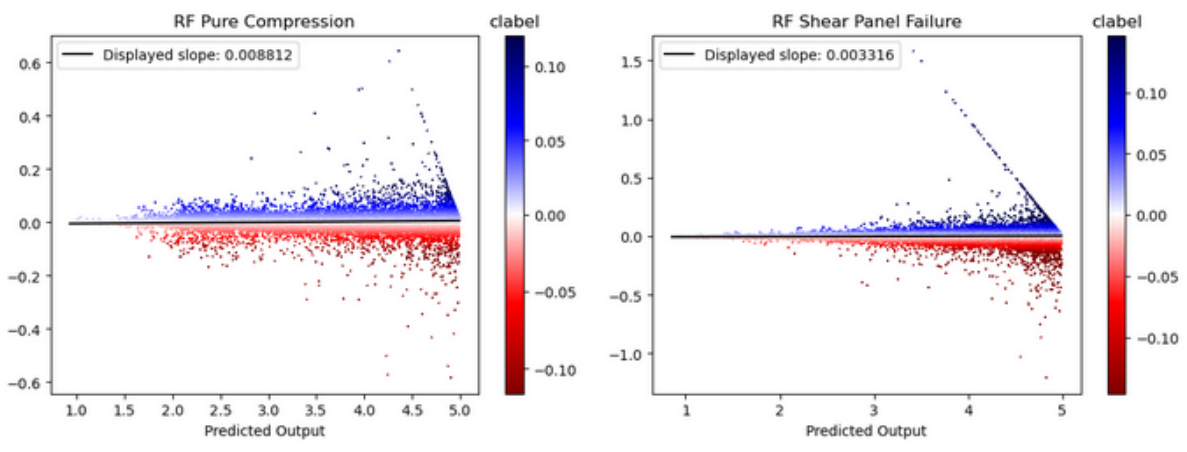


Figure 1.27: Local Uncertainty Model based on $P(E|\mathbf{Y})$: Scatter plot of the residue as a function of the predicted output \hat{y} , for output variables "RF Pure Compression" and "RF Shear Panel Failure".

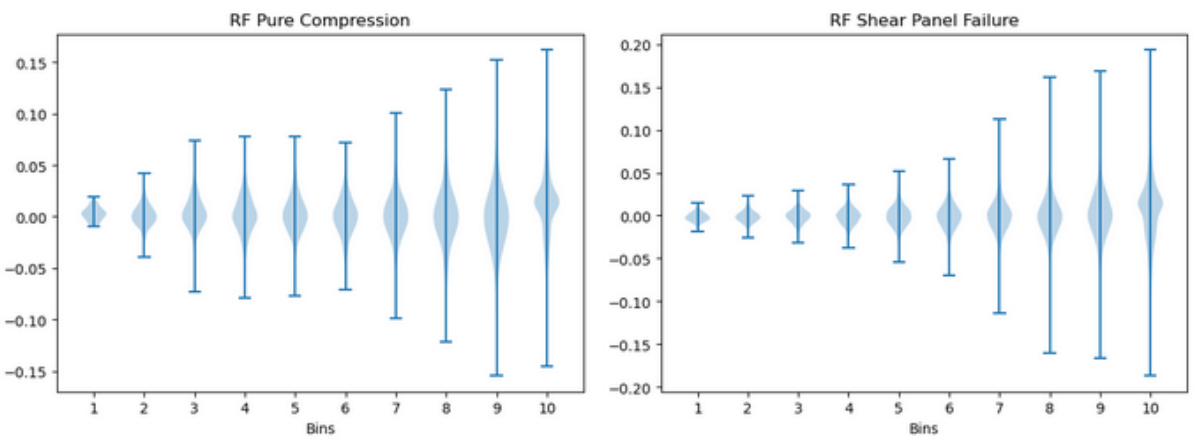


Figure 1.28: Local Uncertainty Model based on $P(E|\mathbf{Y})$: Violin plots of the residue, for binned output variables "RF Pure Compression" and "RF Shear Panel Failure".

This procedure is repeated for all m output variables.

C. Local Output Uncertainty Model (LOUM) evaluation

The bootstrapped error coverage in the test set associated to the LOUM vector is computed with [algorithm 4](#), with the nuance that for each point in the test set, we need to find, based on the point's error, to which bin of the output variable it belongs, and then it is checked whether such error is within the corresponding bootstrapped interval [P2.5, P97.5].

The output is the bootstrap error coverage and its 95% confidence interval. The criteria for a correctly calibrated error coverage is that it is correctly calibrated if $(b-a)\%$ (by default, 95%) lies inside the bootstrapped error coverage confidence interval.

Table 1.22: Local Output Uncertainty Model: Bootstrapped CIs for each of the ten bins into which the output variable "RF Forced Crippling" has been binned. The mean of each CI is also given, as well as the bin extrema $[\hat{y}_{min}, \hat{y}_{max}]$ for every bin (in the first row).

Input: RF Forced Crippling; Output: RF Forced Crippling						
	[0.75, 1.174]	[1.174, 1.598]	[1.598, 2.022]	[2.022, 2.446]	[2.446, 2.87]	[2.87, 3.294]
Mean	-0.000885	-0.0001975	0.0001137	0.001315	0.0004612	-0.0002439
CI	[-0.02095, 0.01634]	[-0.03995, 0.02743]	[-0.06692, 0.02547]	[-0.1572, 0.05091]	[-0.2539, 0.07597]	[-0.1987, 0.0708]

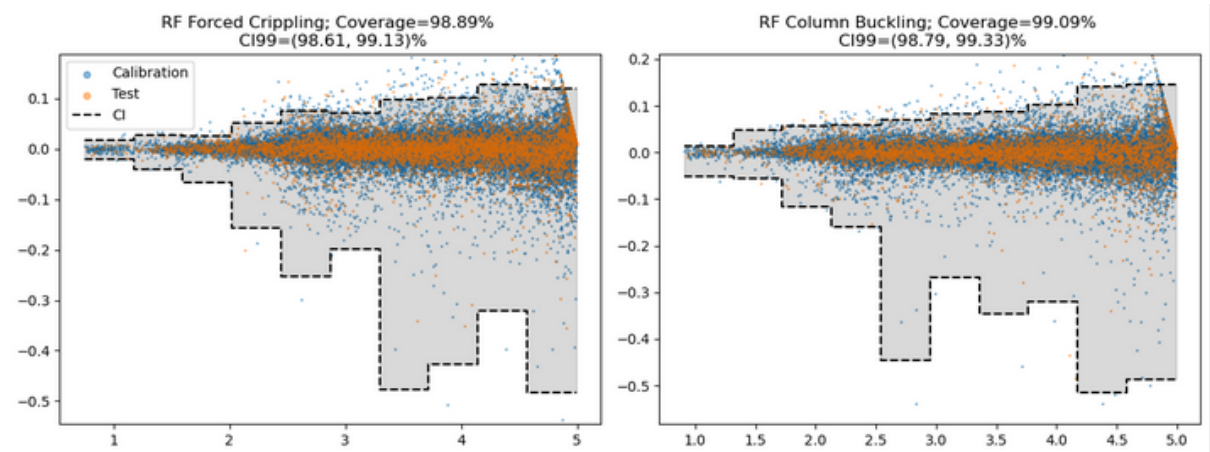


Figure 1.29: LOUM coverage in the validation set. For both output variables coverage is above the minimum 95% threshold.

This procedure is repeated for all m output variables.

A scatter plot of the error of each point in the calibration set is displayed in Figure 1.29, along with the uncertainty model interval (the upper and lower percentiles emphasized in blue and red respectively). This LOUM shows up as a piece-wise constant upper curve and a piece-wise constant lower curve. LOUM coverage for all the six Reserve Factors can be found in Table 1.23.

Table 1.23: LOUM coverage. Coverage in the validation set is displayed in the first row, whereas the coverage bootstrapped CIs are displayed in the second row.

Input: dp; Output: RF Forced Crippling		
	0.000000	0.900000
Mean	0.001506	0.002707
CI	[-0.5033, 0.09891]	[-0.5199, 0.1104]

1.7.3 Local uncertainty model based on $P(E|\mathbf{X})$

A. Input variable binarization

In order to be able to computationally afford LIUM calculation, it is needed to bin the input space in the first place.

For illustration, a scatter plot of the error of each point in the calibration set as a function of x_i is displayed in Figure 1.30 (just two input numerical and two categorical variables have been selected for convenience).

For each continuous input variable x_i the calibration set is partitioned into a total of equispaced n_{bins} bins according to the range of input variable x_i .

For illustration, in [Figure 1.31\(a\)](#) n_{bins} number of violin plots (one per bin, concatenated in a single plot where the "x axis" is the bin number) are plotted, where each violin plot describes the error density of the points in the respective bin.

Binning is exclusive to continuous numerical variables. For illustration, in [Figure 1.31\(b\)](#) and [Figure 1.31\(c\)](#) m_i violin plots (one per each possible value that the corresponding input variable x_i can take) are plotted, where each violin plot describes the error density of the points whose input variable x_i takes the same value.

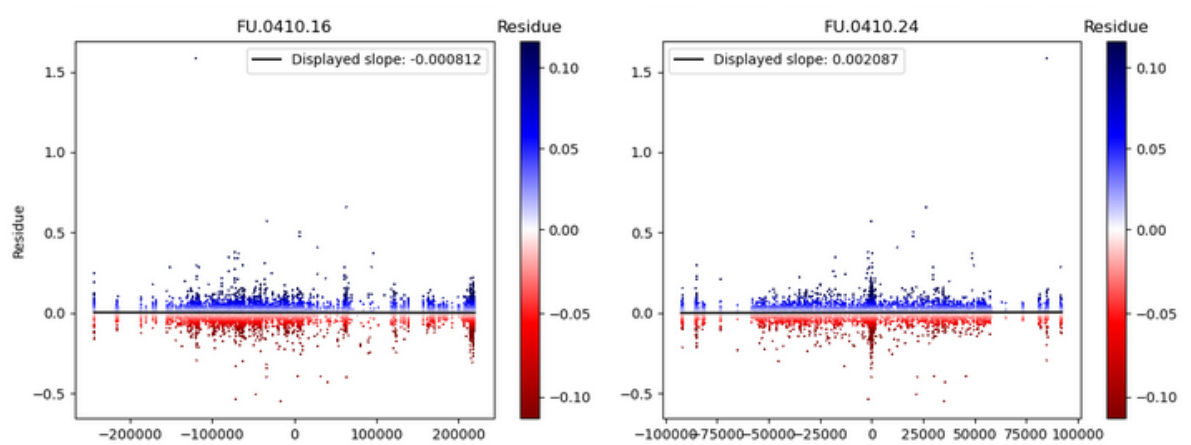


Figure 1.30: LIUM: Scatter plot of the residue of "RF Forced Crippling" as a function of the input x (left: x is "FU.0410.16". Right: x is "FU.0410.24").

B. Local Input Uncertainty Model (LIUM) computation

For each continuous input variable x_i that has been discretized into n_{bins} bins:

- It is checked whether the number of points inside each bin fulfils the minimum bin size (set at 300 points) requirement.
- For those bins for which the minimum bin size requirement is not met, the bin is given the Global Uncertainty Model (GUM).
- For those bins for which the minimum bin size requirement is met, an uncertainty model is computed in terms of the bootstrapped interval [P2.5, P97.5] (or a general [a,b]) with [algorithm 3](#), and the resulting local uncertainty model is assigned to the bin.

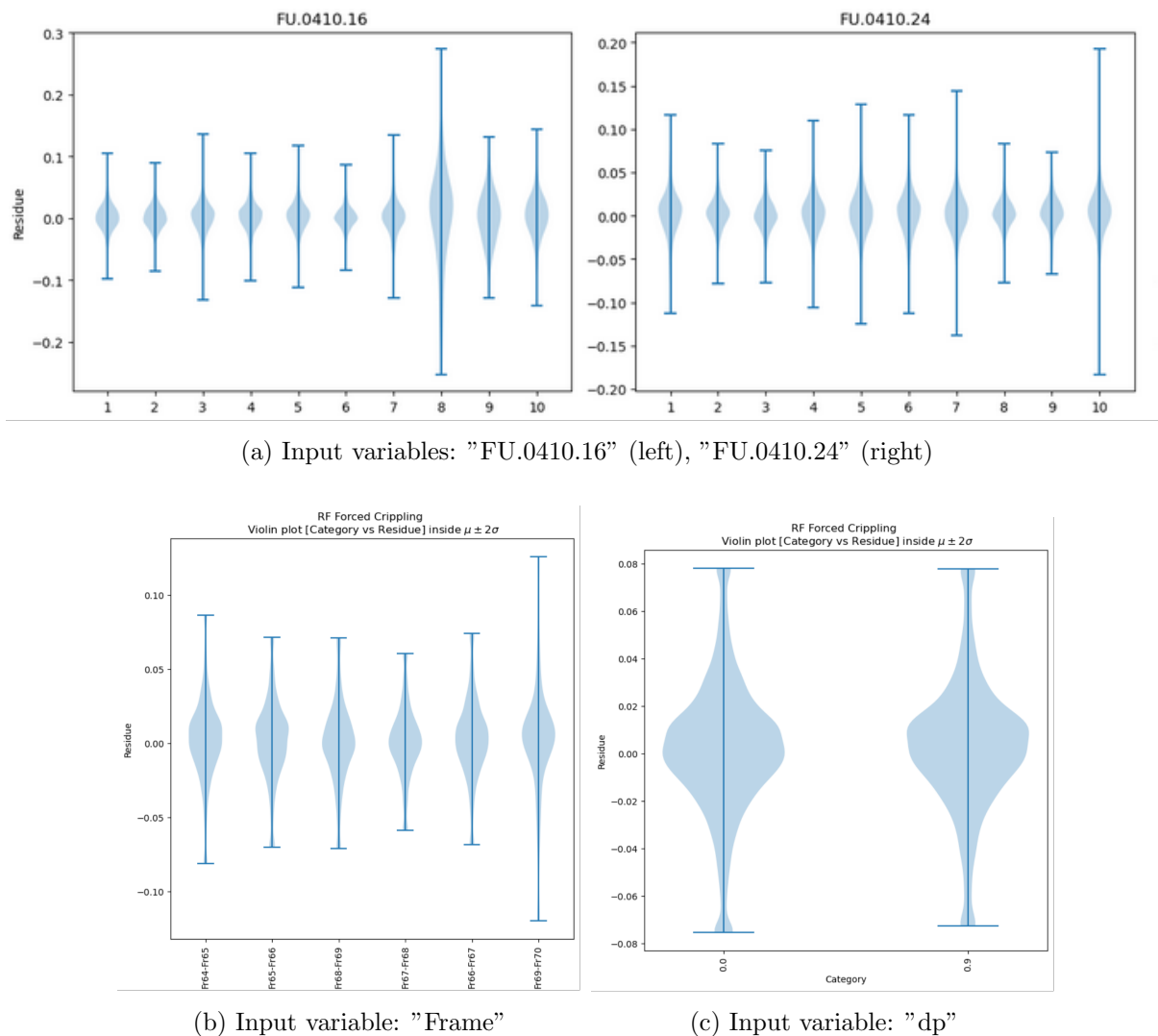


Figure 1.31: Violin plots showing the residue of output variable "RF Forced Crippling". (a): Numerical inputs (binned). (b) and (c): categorical inputs.

- The output (illustration of it is provided in [Table 1.24](#)) is the resulting vector of bootstraps [P2.5, P97.5] associated to the input variable x_i .

For each categorical input variable x_i :

- The code checks whether the number of points inside each category fulfils the minimum bin size requirement (the minimum bin size requirement is just a name, note nevertheless that categorical variables have not been binned).
- For those categories for which the minimum bin size requirement is not met, the category is given the Global Uncertainty Model (GUM).

Table 1.24: LIUM: Bootstrapped CIs for binned input variable "FU.0430.26" (bins' extrema displayed as column names). Residue corresponds to output variable "RF Shear Panel Failure".

Input: FU.0430.26; Output: RF Shear Panel Failure								
	[-1.656e+04, -1.325e+04]	[-1.325e+04, -9938]	[-9938, -6625]	[-6625, -3313]	[-3313, 0]	[0, 3313]	[3313, 6625]	[6625, 9938]
Mean	-0.003271	0.007046	-0.001071	0.001169	0.001253	0.0003371	-0.0001739	0.002927
CI	[-0.3023, 0.1606]	[-0.179, 0.1424]	[-0.2358, 0.1031]	[-0.6774, 0.09636]	[-0.6403, 0.1062]	[-1.116, 0.1228]	[-0.2585, 0.1092]	[-0.1927, 0.175]

Table 1.25: LIUM: Bootstrapped CIs for categorical input variable "dp" (possible values that the variable can take are displayed as column names). Residue corresponds to "RF Shear Panel Failure" output variable.

Input: dp; Output: RF Forced Crippling		
	0.000000	0.900000
Mean	0.001506	0.002707
CI	[-0.5033, 0.09891]	[-0.5199, 0.1104]

- For those categories for which the minimum bin size requirement is met, the code computes an uncertainty model in terms of the bootstrap [P2.5, P97.5] (or a general [a,b]) with [algorithm 3](#), and assigns to the category the resulting local uncertainty model.
- The output (illustration of it is provided in [Table 1.25](#)) is the resulting vector of bootstraps [P2.5, P97.5] (with length equal to the number of categories of the categorical variable x_i) associated to the input variable x_i .

This procedure is repeated for all m output variables.

C. Local Input Uncertainty Model (LIUM) evaluation

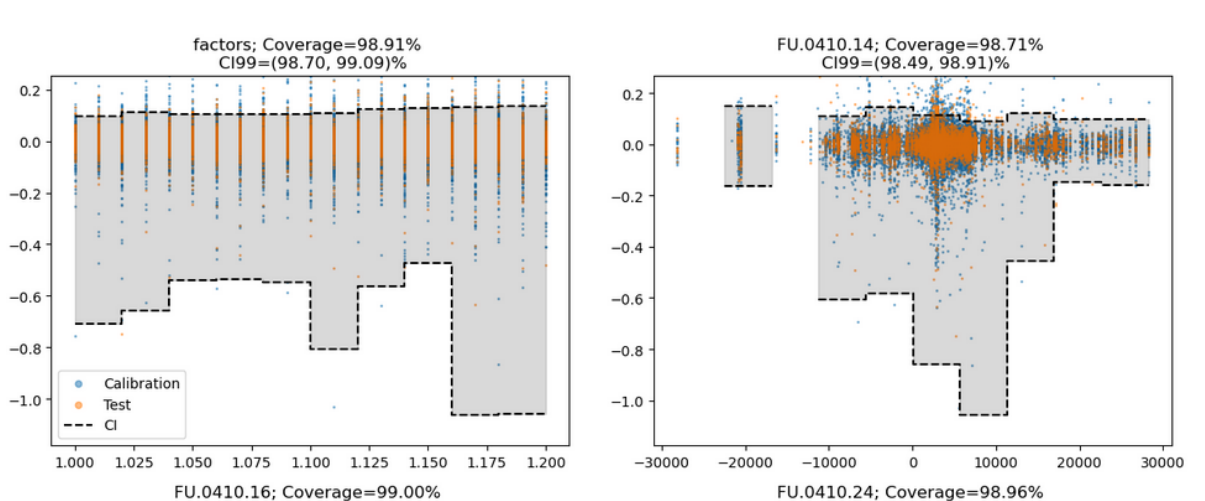
For each input variable:

- The bootstrap error coverage in the test set associated to the LIUM vector is computed with [algorithm 4](#), with the nuance that for each point in the test set, we need to find, based on the point's error, to which bin (or category) of the input variable it belongs, and then check whether such error is within the corresponding bootstrapped interval [P2.5, P97.5].
- The output is the bootstrap error coverage and its 95% confidence interval. The criteria for

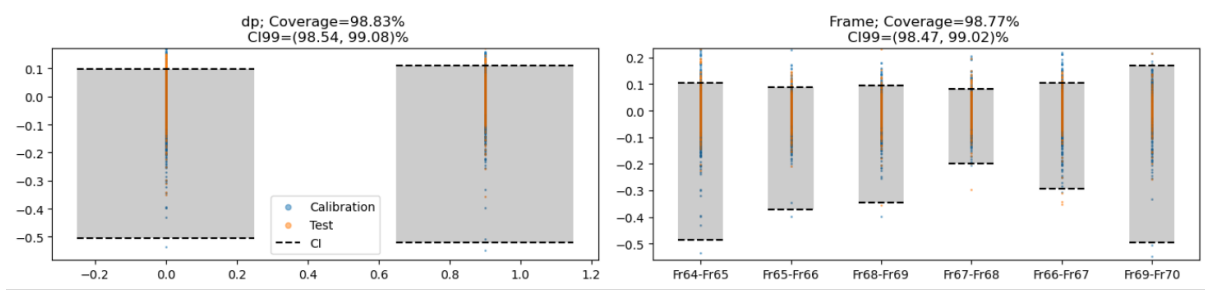
a correctly calibrated error coverage is that it is correctly calibrated if $(b-a)\%$ (by default, 95%) lies inside the bootstrapped error coverage confidence interval.

This procedure is repeated for all m output variables.

For illustration, a scatter plot of the error of each point in the calibration set is displayed in Figure 1.32, along with the uncertainty model interval (the upper and lower percentiles emphasized in blue and red respectively). This LIUM shows up as a piece-wise constant upper curve and a piece-wise constant lower curve.



(a) Numerical inputs: "FU.0410.14" (left), "FU.0410.15" (right). White slices correspond to bins which have not fulfilled the minimum bin size requirements. For such bins, the GUM is used instead of LIUM.



(b) Categorical inputs: "dp" (left), "Frame" (right)

Figure 1.32: LIUM coverage on the evaluation set. Residue of the output variable "RF Forced Crippling". The grey area represents the uncertainty CI calculated by the LIUM for the corresponding bin.

1.7.4 Full uncertainty model (FUM)

The FUM is a conservative uncertainty model that consistently takes, for a given point of the test set (\mathbf{X}, y) , the largest uncertainty

$$\text{FUM}((\mathbf{X}, y)) = \max\{\text{GUM}, \text{LOUM}(y), \text{LIUM}(x_1), \text{LIUM}(x_2), \dots, \text{LIUM}(x_n)\}$$

Accordingly (vid. [Figure 1.33](#)),

- For each point in the test set with input variables (x_1, \dots, x_n) and output prediction y , the the larger out of all the intervals in the set

$$\{\text{GUM}, \text{LOUM}(y), \text{LIUM}(x_1), \text{LIUM}(x_2), \dots, \text{LIUM}(x_n)\}$$

is selected and it is checked whether the error associated to this point lies inside the corresponding interval.

- The error coverage is computed, accordingly.
- The bootstrap error coverage is computed, as per previous sections, and the final output is the bootstrap error coverage and its 95% confidence interval, along with a markdown message about whether the FUM is well calibrated.

Merge: $\max\{P(E), P(E|Y), P(E|X)\}$: FULL UNCERTAINTY MODEL

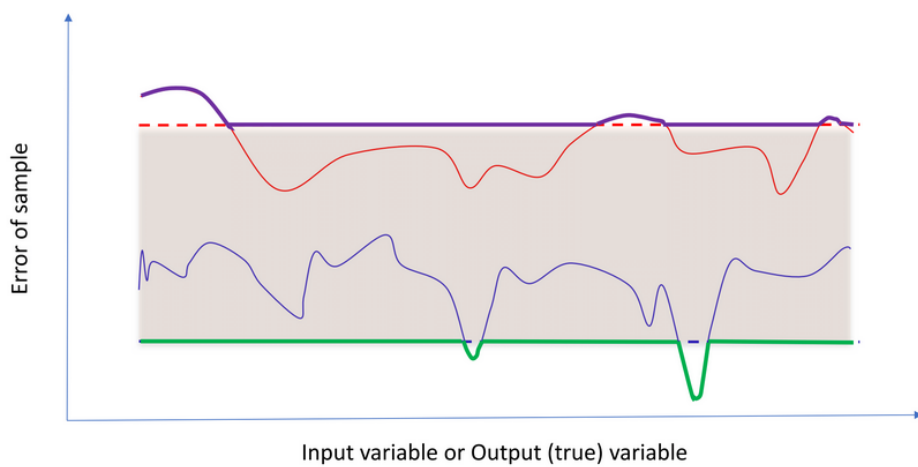


Figure 1.33: Conceptual visualization of FUM as a conservative merge between GUM (whose bootstrap interval [P2.5,P97.5] is represented by the two straight horizontal lines), LOUM and LIUM (whose bootstrap intervals [P2.5,P97.5] are represented indistinctively by the red and blue curves).

Table 1.26: Output of algorithm 1: `reqs_results` table

Voxel ID	Voxel
0	(0.0, Fr68-Fr69, Str40)
1	(0.9, Fr66-Fr67, Str36p)
2	(0.0, Fr69-Fr70, Str29)
3	(0.9, Fr69-Fr70, Str35)
4	(0.0, Fr65-Fr66, Str01)
...	...
827	(0.9, Fr64-Fr65, Str21)
828	(0.9, Fr66-Fr67, Str32)
829	(0.0, Fr64-Fr65, Str26p)
830	(0.0, Fr64-Fr65, Str29p)
831	(0.0, Fr67-Fr68, Str07)
751 rows × 1 columns	

The first step is check whether the train and test datasets follow the same empirical distributions. If test data is found to not follow the same distribution as the train data, the evaluation of the model would be biased or the test data would be outside input applicability. Take, for instance, the extreme case in which the statistical distribution for some input numerical variable follows a uniform distribution $x_{train} \sim U(a_1, a_2)$ whereas the same input variable in the test dataset follows another distribution $x_{test} \sim U(b_1, b_2)$ where $b_1 \leq a_2$. Clearly, x_{test} is outside the hypercube spanned by x_{train} and is outside the applicability region as a consequence.

Definition 2. Let \mathbf{X} represent some dataset, which has been split in \mathbf{X}^{TRAIN} and \mathbf{X}^{TEST} . \mathbf{X} is said to be order 1 [$O(1)$] well-split if and only if $\mathbf{X}^{TEST} \subseteq Hull[\mathbf{X}^{TRAIN}]$.

Where we denote the convex hull of \mathbf{X}^{TRAIN} by $Hull[\mathbf{X}^{TRAIN}]$.

Definition 3. Let \mathbf{X} represent the dataset defined in 2. \mathbf{X} is said to be order 2 well-split if and only if

Table 1.27: Voxel reference table. Lorem ipsum dolor sit amet, consectetur adipiscing elit.

Voxel ID	Voxel
0	(0.0, Fr68-Fr69, Str40)
1	(0.9, Fr66-Fr67, Str36p)
2	(0.0, Fr69-Fr70, Str29)
3	(0.9, Fr69-Fr70, Str35)
4	(0.0, Fr65-Fr66, Str01)
...	...
827	(0.9, Fr64-Fr65, Str21)
828	(0.9, Fr66-Fr67, Str32)
829	(0.0, Fr64-Fr65, Str26p)
830	(0.0, Fr64-Fr65, Str29p)
831	(0.0, Fr67-Fr68, Str07)

751 rows × 1 columns

1.8 Las movidas de Rodrigo

Orbit propagation is a very wide and varied field. It comprises many different approaches and methods to obtain more or less accurate results, with a higher or lower computational cost. Some examples are the numerical integration of the equations of motion in cartesian coordinates, the numerical integration of the variational equations (*i.e.* equations of motion expressed in OEs) and the development of closed-form solutions by simplifying the problem. Within this last group, State Transition Matrices arise.

The State Transition Matrix is a linearization procedure of a nonlinear dynamical system. It is used to approximate the dynamics of said system over short periods of time, allowing for a lower computational cost while maintaining an acceptable accuracy. This concept is not restricted to orbital mechanics, although it is one of the main fields in which it is used [34].

This section intends to provide some background in (a) its mathematical formulation and (b) its applications in orbit theory.

1.8.1 Concept: System dynamics.

Consider the uncontrolled, nonlinear dynamic system that is characterized through the state vector $\underline{y} = [y_1, y_2, \dots, y_n]$. The Initial Value Problem (IVP) for this system may be expressed as:

$$[P] \equiv \begin{cases} \text{Eq. } \frac{dy}{dt} = \mathbf{F}(\underline{y}, t) \\ \text{ICs. } \underline{y}(t_0) = \underline{y}_0 \end{cases} \quad (1.3)$$

where $\mathbf{F}(\underline{y}, t)$ represents the nonlinear dynamics of the system. This problem is unsolvable in general, mainly due to its nonlinearity. In the context of orbit propagation, the state vector \underline{y} might be the position and velocity (be it relative or absolute) of the celestial body, and the dynamics function \mathbf{F} contains the considered force model. In order to arrive at a closed-form, solvable problem, it is assumed that the solution $\underline{y}(t)$ can be expressed as:

$$\underline{y}(t) = \Phi(t, t_0)\underline{y}(t_0) \quad (1.4)$$

where $\Phi(t, t_0)$ is the State Transition Matrix (STM) of the system. This matrix allows the state vector at a certain epoch t to be calculated as the product of the matrix times the initial condition. This expression is obviously very favorable, but the question now is how does one

compute it. Its actual definition can be easily derived from (1.4) as:

$$\Phi(t, t_0) \equiv \frac{\partial \underline{y}}{\partial \underline{y}_0} \quad (1.5)$$

Yet again, how to compute it is not clear at all. There are three main options, depending on the situation:

- A. If the nonlinear solution as a function of the initial condition is known, then the expression (1.5) is directly applied. This is an uncommon case, although simplified examples exist in the orbit propagation field. For example, the Keplerian motion equations expressed in Keplerian orbital elements (OEs) can be solved this way, due to the trivial remaining equations. Another example is the Clohessy-Wiltshire solution, from which the STM can be directly obtained. This process is detailed later on in section ??.
- B. The nonlinear solution is unknown in the original state space, but can be calculated in a different space through a transformation. Mathematically, this can be written as:

$$\Phi_y(t, t_0) = \frac{\partial \underline{y}}{\partial \underline{y}_0} = \frac{\partial \underline{y}}{\partial \underline{u}} \frac{\partial \underline{u}}{\partial \underline{u}_0} \frac{\partial \underline{u}_0}{\partial \underline{y}_0} \equiv W(t) \Phi_u(t, t_0) (W(t_0))^{-1} \quad (1.6)$$

where $W(t)$ is the transformation matrix, where it is assumed that the transformation $\underline{y} = h(\underline{u})$ is known. An example of this kind of approach is the transformation of the Cartesian equations of motion into the Keplerian OEs, whose solution is known, as mentioned in A.. This is a very commonly used method in relative orbit propagation, as in [35, 36].

- C. If none of the above can be performed, then the STM can be integrated itself, to be then used to calculate the state vector. This starts by differentiating (1.3) with respect to the initial condition \underline{y}_0 , leading to:

$$\begin{aligned} & \bullet \quad \frac{\partial}{\partial \underline{y}(t_0)} \frac{d \underline{y}(t)}{dt} = \frac{d}{dt} \frac{\partial \underline{y}(t)}{\partial \underline{y}(t_0)} = \frac{d}{dt} \Phi(t, t_0) \\ & \bullet \quad \frac{\partial \mathbf{F}(t, \underline{y})}{\partial \underline{y}(t_0)} = \frac{\partial \mathbf{F}(t, \underline{y})}{\partial \underline{y}(t)} \frac{\partial \underline{y}}{\partial \underline{y}(t_0)} = \mathbf{A} \Phi(t, t_0) \\ \Rightarrow [P] \equiv & \begin{cases} \text{Eq. } \frac{d}{dt} \Phi(t, t_0) = \mathbf{A} \Phi(t, t_0) \\ \text{IC } \Phi(t_0, t_0) = \mathbb{I}_{n \times n} \end{cases} \quad (1.7) \end{aligned}$$

This last method is a bit unrewarding, as it forces one to integrate an IVP. However, the problem in terms of $\Phi(t, t_0)$ (eq. (1.7)) might be simpler or more efficient than the original (eq. (1.3)), although it is rare. An example of this approach is shown later in section ??.

1.8.2 Applications of STMs in celestial mechanics.

State Transition Matrices can be useful in a wide range of spacecraft dynamics applications. Some of the most important are [37]:

A. Precise Orbit Determination.

Precise Orbit Determination (POD) is a method through which the orbit of a flying spacecraft can be determined with a high accuracy [38]. This estimation is performed using general orbit determination algorithms, such as Kalman filtering or a batch least squares. It requires both high-precision geodetic receivers and high-precision dynamics models, where STMs comes to play. POD usually requires all typically important perturbations, such as non-spherical gravity, drag, tidal forces ...

B. Guidance, Navigation and Control (GNC).

GNC deals with the design the systems to control the spacecraft. It involves the determination of the desired trajectory (guidance), the instantaneous determination of the spacecraft's position (navigation) and the manipulation of the controllers to execute guidance commands (control). STMs become very useful specially in situations in which the linearization error is small, such as in rendez-vous, station-keeping or formation flying operations. They prove to be useful in all three branches:

- Guidance: STMs are a lightweight yet precise tool to generate reference trajectories.
- Navigation: Signal filtering makes extensive use of STMs for the propagation of the estimated state. This is certainly one of the most relevant applications.
- Control: Algorithms like robust online optimal control involve state propagation, using the STM.

C. Orbit design.

Alternatively, rather than propagating already defined orbits, it may be useful to solve the inverse problem: that is, find the orbit that satisfies a set of conditions (*e.g.* optimality). This

is specially relevant for the Circular Restricted Three Body Problem (CR3BP), or its particular case of Halo orbits (periodic 3D orbit near one of the Lagrange libration points). STMs are quite useful to determine an initial solution for said Halo orbits, and can also be used to evaluate the effect of a deviation in initial conditions or other parameters.

D. Covariance matrix propagation.

Some degree of uncertainty will always be assumed in the estimation of a spacecraft's position and velocity. This matter becomes really important in the context of collision avoidance, where ideally, said uncertainty would be exactly calculated. However, these values are usually not something inherently worrying. What is worrying indeed is that this uncertainty may propagate in a divergent fashion, leading to unbounded trajectories with its inherent collision risk.

Here is where the covariance matrix comes to light. Conceptually, it can be seen as an entity which indicates how certain are each of the components of the state vector. That is represented by their variances and covariances. Mathematically, it is defined as:

$$P(t) = E \left[(\hat{x} - \underline{x}) (\hat{x} - \underline{x})^T \right]$$

If one knew the covariance at a certain epoch t_j , it is possible to map it to a different epoch t_k (latter or earlier) through the STM, that is:

$$\begin{aligned} P(t_k) &= E \left[(\hat{x}_k - \underline{x}_k) (\hat{x}_k - \underline{x}_k)^T \right] = E \left[\Phi(t_k, t_j) (\hat{x}_j - \underline{x}_j) (\hat{x}_j - \underline{x}_j)^T \Phi^T(t_k, t_j) \right] \\ &\Rightarrow P(t_k) = \Phi(t_k, t_j) P(t_j) \Phi^T(t_k, t_j) \end{aligned}$$

Now, once the mathematical formalism has been stated, it is time to apply it to the situation at hand. Spacecraft state uncertainty has essentially two sources: estimation error (associated to navigation) and execution error (associated to control/manoeuvres).

In a fairly relaxed approach (*i.e.* assuming the state variables be decoupled), the covariance matrix associated to the estimation error has the following shape:

$$P_{est} = \begin{bmatrix} \delta x^2 & 0 & 0 & 0 & 0 & 0 \\ 0 & \delta y^2 & 0 & 0 & 0 & 0 \\ 0 & 0 & \delta z^2 & 0 & 0 & 0 \\ 0 & 0 & 0 & \delta v_x^2 & 0 & 0 \\ 0 & 0 & 0 & 0 & \delta v_y^2 & 0 \\ 0 & 0 & 0 & 0 & 0 & \delta v_z^2 \end{bmatrix} \quad (1.8)$$

where $\delta\psi$ indicates the standard deviation of the variable ψ . An useful way to visualize the covariance is the probability ellipsoid, defined by:

$$\begin{bmatrix} \tilde{x} & \tilde{y} & \tilde{z} \end{bmatrix} P_{xyz}^{-1} \begin{bmatrix} \tilde{x} \\ \tilde{y} \\ \tilde{z} \end{bmatrix} = l^2$$

where $\tilde{x}, \tilde{y}, \tilde{z}$ are the coordinates of a point of the ellipsoid (referred to its center), P_{xyz} is the partition of the covariance matrix related to the position and l is the sigma coefficient. That is, for $l = 2$, the equation represents the ellipsoid in which the spacecraft will be found with a 2σ probability. An example of the evolution of this ellipsoid can be seen for a small radial hop in figure 1.34.

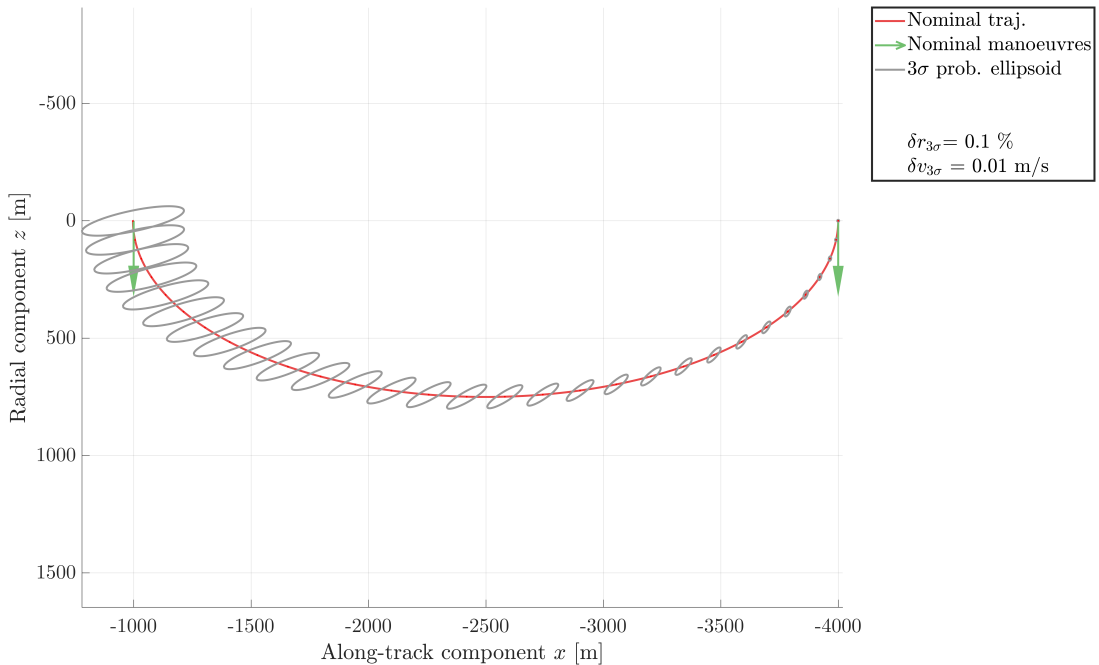


Figure 1.34: Covariance ellipsoid evolution along a radial hop.

Most of these concepts lie out of the thesis' scope. However, it is important to know that the STMs developed or quoted throughout this thesis can be used in many different fields of celestial mechanics.

Conclusions and research outlook.

The increasingly higher relevance of relative motion is beyond question. Satellite constellations, rendez-vous operations and formation flying missions are becoming an everyday occurrence, and their growing success rates are no coincidence. Incrementally better models (*i.e.* truer-to-life, accounting for more effects) have an essential role in this.

In order to gain a comprehensible insight on this topic, this thesis has followed the same bottom-up structure, starting from the very simple Hill/Clohessy-Wiltshire equations up to the modelling of perturbations. The use of linear, closed-form models (through STMs) is an advantageous approach: firstly, computational cost drops, but even more importantly, deeper knowledge about the dynamics of the system is achieved. This allows for, among other things, the design of relative orbits with certain characteristics (*e.g.* safe orbits).

Any state-of-the-art model requires an analysis of the relevant perturbations to be carried out. For the case of Earth artificial satellites, this usually leaves the non-spherical gravity as the most important of them. Kaula's theory allows for the analysis of the effect of any spherical harmonic, which naturally leads for better accuracy models. Although it features certain singular cases (resonances and circular or equatorial orbits), these can be solved. Many applications can be branched from this theory, such as mean-to-osculating transformations, linearized relative motion models, resonance analysis ...

In conclusion, the modelling of perturbations is key for the construction of accurate linearised relative motion models as well as relative orbit design; both of which play a paramount role in the constantly growing discipline of distributed space systems.

Research outlook and future work.

The very wide horizon in which this topic is framed leads for countless possible research areas.

The evaluation of a robust implementation of Kaula's theory is the first on the list. This would be followed by an analysis of the resonant and secular terms, such as done by Chao [39]. The development of mean-to-osculating transformations through this theory is also considered,

which could derive into the development of linear relative motion models based on it.

In a somewhat more general sense, the survey, analysis and implementation of perturbed relative motion models (STMs) is to be tackled. A performance analysis of these models against a High-Fidelity and unperturbed models would be insightful, surely.

Orbit safety might also be an interesting topic to follow up on. A review of the existent models for non-circular, perturbed reference orbits would be insightful, and would continue on the here developed models for simpler cases (*i.e.* circular perturbed and elliptic unperturbed).

Further down the road, other types of perturbations might be analyzed, through the averaging methods here presented. Third bodies or drag are the most relevant ones, although second-order NSG effects are also to be considered.

Finally, real world scenarios may be analyzed, and eventually, a self-contained tool for this purpose could be regarded. Hopefully, this sort of roadmap looks as compelling as it does to the author.

Absolute and relative orbital element sets.

A.1 Introduction.

The description of a spacecraft's state is done via a state vector. While it can include several variables with other purposes (*e.g.* filtering), its only information throughout this thesis is the position and velocity. There are two main ways to describe them:

- A.** Through **cartesian coordinates**
- B.** Through **orbital elements**

While the first option yields a very explicit and graphic-ready description, the second one usually has two advantages over it. Firstly, orbital elements are generally more intuitive about both the orbit and the position on it. Secondly, as orbital elements are generally slow-varying, they allow for a bigger integration timestep without losing accuracy. This is quite clear when studying keplerian motion, as most of the elements remain constant. Variational formulation and Hamilton-Jacobi theory (with the notion of changing variables as the full solution of a problem) relate to this fact.

Throughout this thesis, several sets of orbital elements have been used. The goal of this appendix is to clarify on the definition and differences between them. Absolute orbital elements (OEs) will be described first, followed by relative OEs (ROEs).

A.2 Absolute element sets.

A.2.1 Workflow for transformations between absolute element sets.

Consider two different sets of OEs, denoted by \underline{OE} and $\widetilde{\underline{OE}}$. The transformation function $\mathbf{G}_{\underline{OE} \rightarrow \widetilde{\underline{OE}}}$ between them is defined by:

$$\widetilde{\underline{OE}} = \mathbf{G}_{\underline{OE} \rightarrow \widetilde{\underline{OE}}}(\underline{OE}) \quad (\text{A.1})$$

A numerous amount of element sets have been historically defined. Nevertheless, some of them are much more commonly used than others. Although this analysis will be restricted to a short number of sets (say n), the number of transformations becomes arduously large as n increases ($n(n - 1)$).

In order to reduce the number of transformation functions \mathbf{G} , the later defined Keplerian OEs (KOE) will be used as a pivot, that is, building only transformations to and from KOEs. This will in turn reduce the number of required functions to $2n$. The Keplerian set also has a further advantage: as it is the classical element set, almost every other set is defined explicitly in terms of it, so that transformations to and from them can be easily derived. A simple, graphical explanation of this is shown in figure A.1.



Figure A.1: Workflow for transforming between two arbitrary absolute element sets.

A.2.2 Element sets.

A.2.2.1 Keplerian orbital elements (KOE).

The Keplerian set of OEs (KOE) is one of the most widely used and classic options. An usual definition is the following:

$$\left\{ \begin{array}{lll} a & \equiv & \text{Semimajor axis} & [L] \\ e & \equiv & \text{Eccentricity} & [-] \\ i & \equiv & \text{Inclination} & [\text{rad}] \\ \Omega \text{ or } RAAN & \equiv & \text{Right ascension of the ascending node} & [\text{rad}] \\ \omega & \equiv & \text{Argument of periapsis} & [\text{rad}] \\ M & \equiv & \text{Mean anomaly} & [\text{rad}] \end{array} \right. \quad (\text{A.2})$$

The last element commonly varies across literature, being substituted by the true anomaly θ ; or, when tackling the variation of orbital parameters, by the mean anomaly at $t = 0$ (M_0) or the perigee time T_0 [40]. Mean anomaly is used due to the simplicity of its unperturbed variational equation, as it has a constant rate (denoted by n). The geometrical meaning and definition of these elements is out from the scope of this thesis. Nonetheless, figure A.2 shows a simple geometrical drawing of the involved angles.

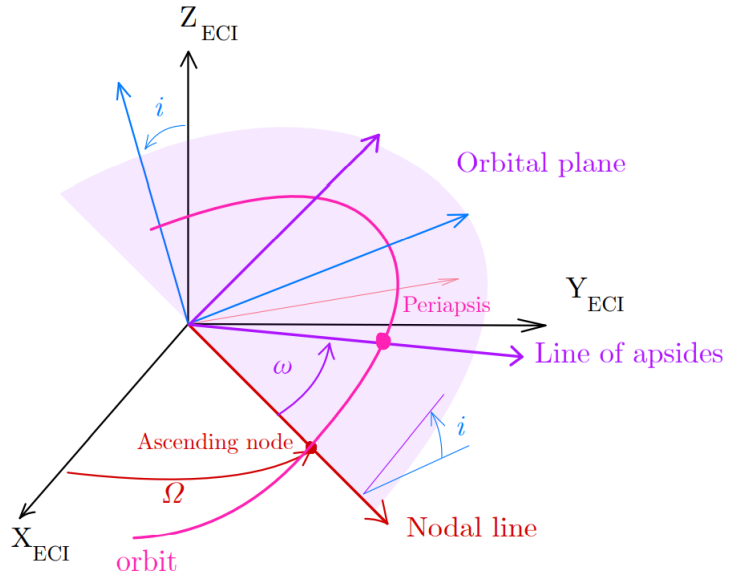


Figure A.2: Frame rotation from inertial to perifocal frame.

As it is seen in the figure before, the Keplerian elements become singular in two cases:

- A. If the **inclination** is null, the orbital plane is coincident with the inertial reference (ECI x-y) plane. The ascending node is hence undefined in this case.
- B. If the **eccentricity** is null, the periapsis is not defined, as it is the nearest point of the orbit around the central body. Thus, there is no angle defining its position, making the argument of periapsis singular.

These singularities are unfortunately quite common in orbit design. They correspond respectively with equatorial and circular orbits. In order to avoid this behaviour, many different elements sets have been defined. Wiesel [40] shows an intuitive approach in section 2.10, solving either problem with a graphic approach.

A.2.2.2 Eccentricity/inclination vectors orbital elements (EIOE).

This set, originally defined for geostationary orbits in absolute terms [41], is used mainly as a relative OE set. Though it is actually not used along this thesis, its definition is helpful for introducing the relative counterpart.

I. Eccentricity vector.

The notion of the eccentricity vector is quite basic, as it is, when in unperturbed motion, a constant of the dynamic system. It is defined as the eccentricity-sized vector pointing towards the perigee. Nonetheless, for this purpose, the eccentricity vector is defined as [42]:

$$\underline{e} = \begin{Bmatrix} e_x \\ e_y \end{Bmatrix} = e \begin{Bmatrix} \cos \varpi \\ \sin \varpi \end{Bmatrix} \quad (\text{A.3})$$

where the argument of perigee ω might be substituted with the sum $\omega + \Omega$ [as in 41]. A graphical representation can be seen later in the relative definition A.5(a). As it arises from (A.3), it substitutes the eccentricity and argument of perigee from the Keplerian OE set.

II. Inclination vector.

The inclination vector is perpendicular to the orbital plane, similarly to the angular momentum, but inclination-sized. It is defined by its components as [41]:

$$\underline{i} = \begin{Bmatrix} i_x \\ i_y \end{Bmatrix} = i \begin{Bmatrix} \cos \Omega \\ \sin \Omega \end{Bmatrix}$$

The graphical interpretation is not as straightforward as for the eccentricity vector. It is clear that these components substitute the out-of-plane related elements i and Ω .

III. Element set.

The EI orbital element set is then composed of:

$$\left\{ \begin{array}{lcl} a & \equiv & \text{Semimajor axis} & [L] \\ e_x = e \cos \omega & \equiv & \text{x-projection of } \underline{e} & [--] \\ e_y = e \sin \omega & \equiv & \text{y-projection of } \underline{e} & [--] \\ i_x = i \cos \Omega & \equiv & \text{x-component of } \underline{i} & [--] \\ i_y = i \sin \Omega & \equiv & \text{y-component of } \underline{i} & [--] \\ \lambda = \omega + M & \equiv & \text{Mean argument of latitude} & [\text{rad}] \end{array} \right. \quad (\text{A.4})$$

A.2.2.3 Quasi-nonsingular orbital elements (QNSOE).

The quasi-nonsingular (QNS) orbital element set tackles the singularity existing in circular orbits [43], [44] [45]. It is quite similar to the formerly defined EI set, as it uses again the components of the eccentricity vector to substitute e and ω . The set is then defined as:

$$\left\{ \begin{array}{lcl} a & \equiv & \text{Semimajor axis} & [L] \\ q_1 = e \cos \omega & \equiv & \text{x-projection of } \underline{e} & [--] \\ q_2 = e \sin \omega & \equiv & \text{y-projection of } \underline{e} & [--] \\ i & \equiv & \text{Inclination} & [\text{rad}] \\ \Omega & \equiv & \text{Right ascension of the ascending node} & [\text{rad}] \\ \lambda = \omega + M & \equiv & \text{Mean argument of latitude} & [\text{rad}] \end{array} \right. \quad (\text{A.5})$$

Though some authors use a different order, this is the one used in this thesis, so as to keep the time-varying element on the last place.

A.2.2.4 Equinoctial orbital elements (EOE).

The QNS set of elements only solved half of the singularity problem. To solve both, thus enabling the description of equatorial and polar orbits, the equinoctial set of elements is defined

as:

$$\left\{ \begin{array}{lll} a & \equiv & \text{Semimajor axis} & [L] \\ P_1 = e \cos \varpi & \equiv & \text{unclear physical meaning, similar to } e_x & [-] \\ P_2 = e \sin \varpi & \equiv & \text{unclear physical meaning, similar to } e_y & [-] \\ Q_1 = \tan \frac{i}{2} \cos \Omega & \equiv & \text{unclear physical meaning, similar to } i_x & [-] \\ Q_2 = \tan \frac{i}{2} \sin \Omega & \equiv & \text{unclear physical meaning, similar to } i_y & [-] \\ L = \Omega + \omega + \theta & \equiv & \text{True longitude} & [\text{rad}] \end{array} \right. \quad (\text{A.6})$$

where $\varpi = \Omega + \omega$. Not only does the order does change depending on the author, but also the symbols to refer to them. An example of its use is [43].

A.2.2.5 Delaunay orbital elements (DOE).

Delaunay elements arise when formulating the two-body problem through analytical mechanics ???. Conversely to the previous element sets, who are clearly non-canonical (*i.e.* they do not satisfy Hamilton's equations), Delaunay elements are built based on the analytical perspective of the problem. Starting from the canonical set of elements (see appendix ??), Delaunay elements are reached after performing a canonical transformation, leading to the following definition:

$$\left\{ \begin{array}{lll} L = \sqrt{\mu a} & \equiv & \text{unclear physical meaning} & [L^{1/2}] \\ G = L\sqrt{1 - e^2} & \equiv & \text{Angular momentum} & [L^{1/2}] \\ H = G \cos i & \equiv & \text{Polar component of angular momentum} & [L^{1/2}] \\ l = M & \equiv & \text{Mean anomaly} & [\text{rad}] \\ g = \omega & \equiv & \text{Argument of perigee} & [\text{rad}] \\ h = \Omega & \equiv & \text{Right ascension of ascending node} & [\text{rad}] \end{array} \right. \quad (\text{A.7})$$

This set is mainly used in the context of perturbations, as it yields a very convenient expression for the perturbed Hamiltonian (see section ??).

A.3 Relative sets.

Relative elements are at the deepest roots of spacecraft relative motion, offering several advantages over cartesian relative states. First and foremost, they are more intuitive, but they also lead to a reduction of linearisation errors when expanding the deputy's movement around the chief's orbit [46]. In general, relative elements are defined as:

$$\delta \underline{OE} = \mathbf{f} (\underline{OE}_C, \underline{OE}_D) \quad (\text{A.8})$$

which is usually simplified by just taking the arithmetic difference between them, namely

$$\delta \underline{OE} = \underline{OE}_D - \underline{OE}_C \quad (\text{A.9})$$

where the subscripts denote respectively the deputy and chief spacecraft. The question now is, how do transformations between ROEs work.

A.3.1 Workflow for transformations between ROEs.

As for the absolute elements, Keplerian elements will be used as a pivot point. That means that only the transformations from and to RKOEs must be implemented. There are then two types of transformations:

A) From any ROE set to RKOE

While authors provide with scenarios expressed in their own ROE set, the element choice for this thesis is the Keplerian set. That leads to the need of implementing a transformation from the former set to the latter. The considered inputs and outputs are:

- **Inputs:**

- $\widetilde{\underline{ROE}} = \delta \widetilde{\underline{OE}}$: Any type of ROEs, whose absolute equivalents are known as a function of the KOEs ($\widetilde{\underline{OE}} = \mathbf{f}(\underline{KOE})$)
- \underline{KOE}_C : Chief spacecraft/reference orbit KOEs

- **Output:**

- $\underline{RKOE} = \delta \underline{KOE}$: Keplerian ROEs

Taking equation (A.9) and particularizing it for KOEs:

$$\delta \underline{KOE} = \underline{KOE}_D - \underline{KOE}_C \quad (\text{A.10})$$

while the second term is known (input), the second one must be calculated through a certain process:

^{1st} Calculate chief's OEs in the source phase space (*i.e.* $\widetilde{\underline{OE}}_C$)

$$\widetilde{\underline{OE}}_C = \mathbf{G}_{\underline{KOE} \rightarrow \widetilde{\underline{OE}}}(\underline{KOE}_C)$$

2nd Compute deputy's OEs by direct addition

$$\widetilde{\underline{OE}}_D = \widetilde{\underline{OE}}_C + \delta \widetilde{\underline{OE}}$$

3rd Compute deputy's KOEs by back-transformation

$$\underline{KOE}_D = \mathbf{G}_{\widetilde{\underline{OE}} \rightarrow \underline{KOE}}(\underline{OE}_D)$$

4th Subtract chief's KOEs from deputy's

$$\delta \underline{KOE} = \underline{KOE}_D - \underline{KOE}_C$$

See graphic A.3 for a more visual explanation.

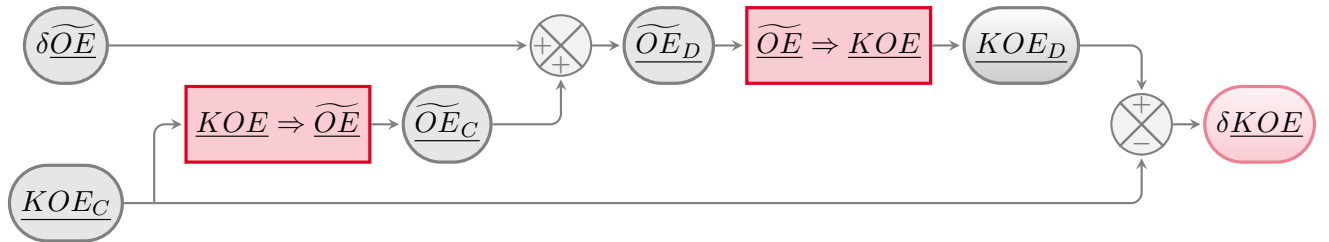


Figure A.3: Workflow for transforming any relative set into KOE.

B) From RKOE to any ROE set

In this case, the assumed inputs and outputs are:

- **Inputs:**

- $\underline{RKOE} = \delta \underline{KOE}$: Keplerian ROEs
- \underline{KOE}_C : Chief KOEs

- **Output:**

- $\widetilde{\underline{ROE}} = \delta \widetilde{\underline{OE}}$: Any type of ROEs, whose absolute equivalents are known as a function of the KOEs ($\widetilde{\underline{OE}} = f(\underline{KOE})$)

For this transformation, the equation A.8 particularized for this case acquires the following shape:

$$\delta\widetilde{OE} = \widetilde{OE}_D - \widetilde{OE}_C \quad (\text{A.11})$$

Equation A.11 can be tackled in two main ways:

- A. Using the pertinent transformations, compute the absolute elements for both spacecrafts \widetilde{OE}_D , \widetilde{OE}_C , and then calculate the arithmetic difference (in a A.3.1). See graphic A.4.

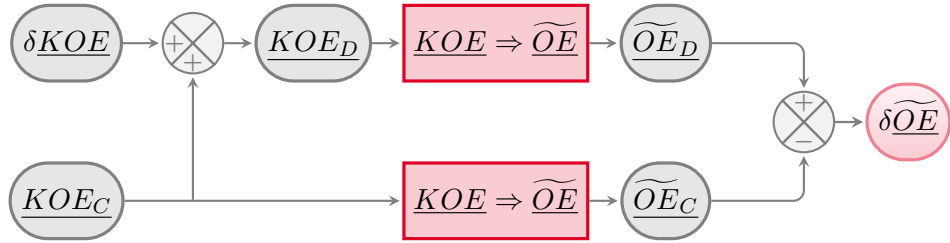


Figure A.4: Workflow for transforming RKOE into any other set.

- B. Expand the deputy absolute OEs (*i.e.* \widetilde{OE}_D) around the chief via a Taylor series expansion with respect to the Keplerian set of elements, retaining terms up to first order, achieving a linearised expression for the transformation. Mathematically:

$$\widetilde{OE}_D = \widetilde{OE}(KOE_D) = \widetilde{OE}(KOE_C + \delta KOE) = \widetilde{OE}_C + \frac{\partial \widetilde{OE}}{\partial KOE} \delta KOE + \mathcal{O}(\delta KOE^2)$$

hence,

$$\delta \widetilde{OE} \approx \widetilde{OE}_C + \frac{\partial \widetilde{OE}}{\partial KOE} \delta KOE - \widetilde{OE}_C = \frac{\partial \widetilde{OE}}{\partial KOE} \delta KOE \quad (\text{A.12})$$

where the Jacobian matrix is generally simple, as it usually only implies polynomic or trigonometric functions. Equation (A.12) is then a first order approximation of (A.11). Its validity is then reduced to a close proximity between both spacecrafts, which should be assessed.

A.3.2 Element sets.

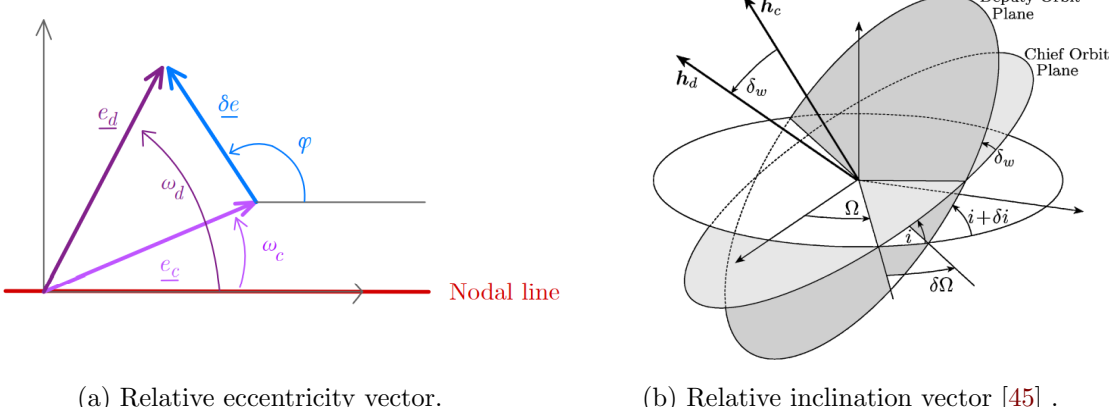
Besides the ones derived directly from its absolute counterparts, a couple of additional ROE sets will be herewith defined and explained. This is due to one of two reasons. The first one is that some ROE sets are only defined in relative terms, lacking any absolute equivalent. The second one is that it might be interesting to dive in the meaning of the relative sets, deriving

interesting relations that would otherwise be overlooked.

A.3.2.1 Relative eccentricity/inclination vectors orbital elements (REIOE).

This ROE set is the counterpart of the EI set (see A.2.2.2). It is nonetheless interesting to see the meaning and shape of it, as it is quite widely used in literature [42, 44, 45]. Firstly, the elements themselves are defined, to later analyze the meaning behind them:

$$\left\{ \begin{array}{l} \delta a \equiv \text{Relative semimajor axis} \quad [L] \\ \delta e_x \equiv \text{x-component of } \underline{\delta e} \quad [--] \\ \delta e_y \equiv \text{y-component of } \underline{\delta e} \quad [--] \\ \delta i_x \equiv \text{x-component of } \underline{\delta i} \quad [--] \\ \delta i_y \equiv \text{y-component of } \underline{\delta i} \quad [--] \\ \delta \lambda \equiv \text{Relative mean argument of latitude} \quad [rad] \end{array} \right. \quad (\text{A.13})$$



(a) Relative eccentricity vector.

(b) Relative inclination vector [45].

Figure A.5: Relative eccentricity & inclination vectors.

Concept & meaning

The relative eccentricity vector components substitute the relative eccentricity and the relative argument of perigee. It is based on the eccentricity vector definition (A.3), and a graphical representation can be seen in figure A.5(a). Mathematically:

$$\underline{\delta e} = \begin{Bmatrix} \delta e_x \\ \delta e_y \end{Bmatrix} = \delta e \begin{Bmatrix} \cos \varphi \\ \sin \varphi \end{Bmatrix}$$

where φ is referred to as the AOP of the relative orbit. This vector rules the in-plane relative motion (hand in hand with δa and $\delta\lambda$). There are two ways of tackling the transformation from RKOE to this set (see A.3.1). Besides the exact nonlinear form, a linear version can be derived. Assuming that the difference in the eccentricity vector is due to that of the eccentricity and argument of perigee (δe , $\delta\omega$), it follows that:

$$\delta \underline{e} \approx \begin{bmatrix} \cos \omega & -e \sin \omega \\ \sin \omega & e \cos \omega \end{bmatrix} \begin{Bmatrix} \delta e \\ \delta \omega \end{Bmatrix} \quad (\text{A.14})$$

where terms of second order and higher have been neglected. The relative inclination vector is defined in an alternative way [42] (comparing with the absolute counterpart). Mathematically:

$$\delta \underline{i} = \sin \delta i \begin{Bmatrix} \cos \theta \\ \sin \theta \end{Bmatrix}$$

where θ is the analogue angle to φ in the eccentricity vector, being commonly referred to as the RAAN of the relative orbit. Once again, the linearised transformation from RKOE to this set may be analysed, considering the differences δi and $\delta\Omega$. Applying the law of sines and the law of cosines for spherical trigonometry and assuming small values of δi and $\delta\Omega$, it follows that:

$$\delta \underline{i} = \begin{Bmatrix} \delta i \\ \sin i \delta \Omega \end{Bmatrix} \approx \begin{bmatrix} 1 & 0 \\ 0 & \sin i \end{bmatrix} \begin{Bmatrix} \delta i \\ \delta \Omega \end{Bmatrix} \quad (\text{A.15})$$

where i is the inclination of the chief's orbit. Combining the results of (A.14) and (A.15) with the definitions of the remaining elements, an expression analogue to (A.12) is reached:

$$\left\{ \begin{array}{l} \delta a \\ \delta e_x \\ \delta e_y \\ \delta i_x \\ \delta i_y \\ \delta \lambda \end{array} \right\} \approx \left[\begin{array}{cccccc} 1 & 0 & 0 & 0 & 0 & 0 \\ 0 & \cos \omega & 0 & 0 & -e \sin \omega & 0 \\ 0 & \sin \omega & 0 & 0 & e \cos \omega & 0 \\ 0 & 0 & 1 & 0 & 0 & 0 \\ 0 & 0 & 0 & \sin i & 0 & 0 \\ 0 & 0 & 0 & 0 & 1 & 1 \end{array} \right] \left\{ \begin{array}{l} \delta a \\ \delta e \\ \delta i \\ \delta \Omega \\ \delta \omega \\ \delta M \end{array} \right\} \quad (\text{A.16})$$

A graphical representation of this concept can be seen in figure A.5(b).

However, this definition is changed in some references. In particular, the mean argument of latitude λ is sometimes substituted by the modified relative mean longitude, which is defined as:

$$\delta l_0 \equiv \delta \lambda + \delta \Omega \cos i$$

The advantage of this formulation is that the in-plane motion becomes decoupled. This will also be done in the following set of relative elements.

A.3.2.2 C set of relative orbital elements (CROE).

Defined by Peters & Noomen in [47], this set is also closely related with the orbit safety notion. It arises from the analysis of the Gauss Variational Equations (GVEs) applied to the relative dynamics between a deputy and a chief spacecraft, when the former performs a cotangential

transfer. The elements themselves are defined as:

$$\left\{ \begin{array}{lll} C_1 = \delta p = \eta^2 \delta a - 2 a e \delta e & \equiv & \text{Relative parameter of the orbit} & [L] \\ C_2 = e \delta p - p \delta e & \equiv & \text{unclear physical meaning} & [L] \\ C_3 = -e p (\delta \omega + \cos i \delta \Omega) & \equiv & \text{unclear physical meaning} & [L] \\ C_4 = a (\delta \omega + \cos i \delta \Omega + \eta^{-1} \delta M) & \equiv & \text{Modified relative mean longitude} & [L] \\ C_5 = -p (\cos \omega \delta i + \sin i \sin \omega \delta \Omega) & \equiv & \text{unclear physical meaning} & [L] \\ C_6 = p (\sin \omega \delta i - \sin i \cos \omega \delta \Omega) & \equiv & \text{unclear physical meaning} & [L] \end{array} \right. \quad (A.17)$$

For a proper geometrical and conceptual description of the elements, please see [47]. As an introduction, the first four elements essentially determine the in-plane relative motion. C_1 , C_2 & C_3 arise from a very intelligent interpretation of the GVEs, with C_4 completing the element set. On the other hand, elements C_5 and C_6 describe the out-of-plane motion.

Bibliography

- [1] S. Marsland. *Machine Learning: An Algorithmic Perspective*. 2nd ed. Boca Raton, USA: Chapman & Hall/CRC, 2015 (cit. on pp. xix, 3, 7).
- [2] Y. Xu et al. “Machine-Learning-Assisted Optimization of Aircraft Trajectories Under Realistic Constraints”. In: *Journal of Guidance, Control, and Dynamics* (2023), pp. 1–12.
- [3] B. Shukla, I.-S. Fan, and I. Jennions. “Opportunities for explainable artificial intelligence in aerospace predictive maintenance”. In: *PHM Society European Conference*. Vol. 5. 1. 2020, pp. 11–11.
- [4] P. Adhikari, H. G. Rao, and M. Buderath. “Machine learning based data driven diagnostics & prognostics framework for aircraft predictive maintenance”. In: *Proceedings of the 10th International Symposium on NDT in Aerospace, Dresden, Germany*. 2018, pp. 24–26.
- [5] P. Korvesis. “Machine learning for predictive maintenance in aviation”. PhD thesis. Université Paris Saclay (COmUE), 2017.
- [6] P. Bijlaard. “On the Buckling of Stringer Panels Including Forced Crippling”. In: *Journal of the Aeronautical Sciences* 22.7 (1955), pp. 491–501 (cit. on p. 1).
- [7] F. P. Preparata and M. I. Shamos. “Convex Hulls: Basic Algorithms”. In: *Computational Geometry: An Introduction*. New York, NY: Springer New York, 1985, pp. 95–149. ISBN: 978-1-4612-1098-6. DOI: [10.1007/978-1-4612-1098-6_3](https://doi.org/10.1007/978-1-4612-1098-6_3). URL: https://doi.org/10.1007/978-1-4612-1098-6_3 (cit. on p. 2).
- [8] D. Barrett et al. “Measuring abstract reasoning in neural networks”. In: *Proceedings of the 35th International Conference on Machine Learning*. Ed. by J. Dy and A. Krause. Vol. 80. Proceedings of Machine Learning Research. PMLR, Oct. 2018, pp. 511–520. URL: <https://proceedings.mlr.press/v80/barrett18a.html> (cit. on p. 3).
- [9] B. M. Lake and M. Baroni. “Still not systematic after all these years: On the compositional skills of sequence-to-sequence recurrent networks”. In: *CoRR* abs/1711.00350 (2017). arXiv: [1711.00350](https://arxiv.org/abs/1711.00350). URL: [http://arxiv.org/abs/1711.00350](https://arxiv.org/abs/1711.00350) (cit. on p. 3).
- [10] D. Saxton et al. “Analysing Mathematical Reasoning Abilities of Neural Models”. In: *CoRR* abs/1904.01557 (2019). arXiv: [1904.01557](https://arxiv.org/abs/1904.01557). URL: [http://arxiv.org/abs/1904.01557](https://arxiv.org/abs/1904.01557) (cit. on p. 3).

- [11] T. Ebert, J. Belz, and O. Nelles. “Interpolation and extrapolation: Comparison of definitions and survey of algorithms for convex and concave hulls”. In: *2014 IEEE Symposium on Computational Intelligence and Data Mining (CIDM)*. IEEE. 2014, pp. 310–314 (cit. on p. 3).
- [12] W.-Y. Loh, C.-W. Chen, and W. Zheng. “Extrapolation errors in linear model trees”. In: *ACM Transactions on Knowledge Discovery from Data (TKDD)* 1.2 (2007), 6–es (cit. on p. 3).
- [13] P. Klesk. “Construction of a Neurofuzzy Network Capable of Extrapolating (and Interpolating) With Respect to the Convex Hull of a Set of Input Samples in R”. In: *IEEE Transactions on Fuzzy Systems* 16.5 (2008), pp. 1161–1179. doi: [10.1109/TFUZZ.2008.924337](https://doi.org/10.1109/TFUZZ.2008.924337) (cit. on p. 3).
- [14] R. Balestriero, J. Pesenti, and Y. LeCun. “Learning in high dimension always amounts to extrapolation”. In: *arXiv preprint arXiv:2110.09485* (2021) (cit. on pp. 3, 4, 10).
- [15] I. Bárány and Z. Füredi. “On the shape of the convex hull of random points”. In: *Probability theory and related fields* 77 (1988), pp. 231–240 (cit. on p. 3).
- [16] L. Bonnasse-Gahot. “Interpolation, extrapolation, and local generalization in common neural networks”. In: *arXiv preprint arXiv:2207.08648* (2022) (cit. on pp. 4, 10, 13).
- [17] H. Hotelling. “Analysis of a complex of statistical variables into principal components.” In: *Journal of educational psychology* 24.6 (1933), p. 417 (cit. on p. 9).
- [18] B. Rosner and D. Grove. “Use of the Mann–Whitney U-test for clustered data”. In: *Statistics in medicine* 18.11 (1999), pp. 1387–1400 (cit. on p. 13).
- [19] R. Velez Ibarrola and A. Garcia Perez. *Calculo de probabilidades y Estadistica Matematica*. 1st ed. Madrid, Spain: Universidad Nacional de Educacion a Distancia, 1994 (cit. on p. 15).
- [20] D. Zhang. “A coefficient of determination for generalized linear models”. In: *The American Statistician* 71.4 (2017), pp. 310–316 (cit. on p. 20).
- [21] J. D. Jobson. *Applied multivariate data analysis: regression and experimental design*. Springer Science & Business Media, 2012 (cit. on pp. 20, 37).
- [22] G. Chen, J. R. Gott, and B. Ratra. “Non-Gaussian Error Distribution of Hubble Constant Measurements”. In: *Publications of the Astronomical Society of the Pacific* 115.813 (2003), p. 1269 (cit. on p. 22).

- [23] P. Pernot, B. Huang, and A. Savin. “Impact of non-normal error distributions on the benchmarking and ranking of Quantum Machine Learning models”. In: *Machine Learning: Science and Technology* 1.3 (2020), p. 035011 (cit. on p. 22).
- [24] D. Smyl et al. “Learning and correcting non-Gaussian model errors”. In: *Journal of Computational Physics* 432 (2021), p. 110152 (cit. on p. 22).
- [25] L. Chai et al. “Using generalized Gaussian distributions to improve regression error modeling for deep learning-based speech enhancement”. In: *IEEE/ACM Transactions on Audio, Speech, and Language Processing* 27.12 (2019), pp. 1919–1931 (cit. on p. 22).
- [26] M. C. Jones and A. Pewsey. “Sinh-arcsinh distributions”. In: *Biometrika* 96.4 (2009), pp. 761–780 (cit. on pp. 27, 28).
- [27] B. Rosner. “Percentage points for a generalized ESD many-outlier procedure”. In: *Tech-nometrics* 25.2 (1983), pp. 165–172 (cit. on p. 27).
- [28] B. Efron. “Bootstrap methods: another look at the jackknife”. In: *Breakthroughs in statistics: Methodology and distribution*. Springer, 1992, pp. 569–593 (cit. on p. 29).
- [29] E. B. Wilson. “Probable inference, the law of succession, and statistical inference”. In: *Journal of the American Statistical Association* 22.158 (1927), pp. 209–212 (cit. on p. 32).
- [30] L. Taylor and G. Nitschke. “Improving deep learning with generic data augmentation”. In: *2018 IEEE symposium series on computational intelligence (SSCI)*. IEEE. 2018, pp. 1542–1547 (cit. on p. 35).
- [31] T. K. Kim. “Understanding one-way ANOVA using conceptual figures”. In: *Korean journal of anesthesiology* 70.1 (2017), pp. 22–26 (cit. on p. 37).
- [32] B. R. Kirkwood and J. A. Sterne. *Essential medical statistics*. John Wiley & Sons, 2010 (cit. on p. 38).
- [33] Y. Fujikoshi. “Two-way ANOVA models with unbalanced data”. In: *Discrete Mathematics* 116.1-3 (1993), pp. 315–334 (cit. on p. 41).
- [34] O. Montenbruck and E. Gill. *Satellite Orbits: Models, Methods and Applications*. 1st ed. Wessling, Germany: Springer, 2001 (cit. on p. 72).
- [35] K. Yamanaka and F. Ankersen. “New State Transition Matrix for Relative Motion on an Arbitrary Elliptical Orbit”. In: *Journal of Guidance, Control & Dynamics* 25.1 (2002), pp. 60–66. DOI: [10.2514/2.4875](https://doi.org/10.2514/2.4875) (cit. on p. 73).

- [36] D.-W. Gim and K. Alfriend. “State Transition Matrix of Relative Motion for the Perturbed Noncircular Reference Orbit”. In: *Journal of Guidance Control and Dynamics* 26 (Nov. 2003), pp. 956–971. DOI: [10.2514/2.6924](https://doi.org/10.2514/2.6924) (cit. on p. 73).
- [37] S.-S. Exchange. *Practical Uses of an STM*. 2019. URL: <https://space.stackexchange.com/questions/32916> (cit. on p. 74).
- [38] ESA. *Precise Orbit Determination*. 2011. URL: https://gssc.esa.int/navipedia/index.php/Precise_Orbit_Determination (cit. on p. 74).
- [39] C. Chao and F. Hoots. *Applied Orbit Perturbation and Maintenance*. Aerospace Press, 2018. ISBN: 9781523123346 (cit. on p. 79).
- [40] W. E. Wiesel. *Modern Astrodynamics*. 2nd ed. Beavercreek, Ohio: Aphelion Press, 2010 (cit. on p. 83).
- [41] M. Eckstein, C. Rajasingh, and P. Blumer. “Colocation Strategy and Collision Avoidance for the Geostationary Satellites at 19 Degrees West”. In: *CNES International Symposium on Space Dynamics*. Vol. 25. Oberpfaffenhofen, Germany: DLR GSOC, Nov. 1989, pp. 60–66 (cit. on p. 84).
- [42] S. D’Amico and O. Montenbruck. “Proximity Operations of Formation-Flying Spacecraft Using an Eccentricity/Inclination Vector Separation”. In: *Journal of Guidance, Control & Dynamics* 29.3 (2006), pp. 554–563. DOI: [10.2514/1.15114](https://doi.org/10.2514/1.15114) (cit. on pp. 84, 90, 91).
- [43] D.-W. Gim and K. T. Alfriend. “Satellite Relative Motion Using Differential Equinoctial Elements”. In: *Celestial Mechanics and Dynamical Astronomy* 92.4 (2005), pp. 295–336. DOI: [10.1007/s10569-004-1799-0](https://doi.org/10.1007/s10569-004-1799-0) (cit. on pp. 85, 86).
- [44] S. D’Amico. *Relative Orbital Elements as Integration Constants of Hill’s Equations*. TN 05-08. Oberpfaffenhofen, Germany: Deutsches Zentrum für Luft- und Raumfahrt (DLR), 2005 (cit. on pp. 85, 90).
- [45] H. Schaub. “Relative Orbit Geometry Through Classical Orbit Element Differences”. In: *Journal of Guidance, Control & Dynamics* 27.5 (2004), pp. 839–848. DOI: [10.2514/1.12595](https://doi.org/10.2514/1.12595) (cit. on pp. 85, 90).
- [46] G. Gaias, C. Colombo, and M. Lara. “Accurate Osculating/Mean Orbital Elements Conversions for Spaceborne Formation Flying”. In: (Feb. 2018). <https://www.researchgate.net>.

- [net/publication/340378956_Accurate_OsculatingMean_Orbital_Elements_Conversions_for_Spaceborne_Formation_Flying](https://net-publication/340378956_Accurate_OsculatingMean_Orbital_Elements_Conversions_for_Spaceborne_Formation_Flying) (cit. on p. 86).
- [47] T. Vincent Peters and R. Noomen. “Linear Cotangential Transfers and Safe Orbits for Elliptic Orbit Rendezvous”. In: *Journal of Guidance, Control & Dynamics* 44.4 (2021), pp. 732–748. DOI: [10.2514/1.G005152](https://doi.org/10.2514/1.G005152) (cit. on pp. 92, 93).
- [48] R. H. Lopes, I. Reid, and P. R. Hobson. “The two-dimensional Kolmogorov-Smirnov test”. In: (2007).
- [49] G. Schoups and J. A. Vrugt. “A formal likelihood function for parameter and predictive inference of hydrologic models with correlated, heteroscedastic, and non-Gaussian errors”. In: *Water Resources Research* 46.10 (2010).
- [50] B. D. Tapley, B. E. Schutz, and G. H. Born. *Statistical Orbit Determination*. 1st ed. Amsterdam, Netherlands: Elsevier, 2004.
- [51] K. T. Alfriend and Srinivas. *Spacecraft Formation Flying*. 1st ed. Oxford, United Kingdom: Elsevier, 2010.
- [52] R. H. Battin. *An Introduction to the Mathematics and Methods of Astrodynamics, Revised Edition*. 1st ed. Reston, Virginia: American Institute of Aeronautics and Astronautics, 1999.
- [53] D. Brouwer and G. M-Clemence. *Methods of Celestial Mechanics*. Brackley Square House, London: Academic Press, 1961.
- [54] H. Schaub and J. L. Junkins. *Analytical Mechanics of Space Systems*. Reston, VA: AIAA Education Series, Oct. 2003. DOI: [10.2514/4.861550](https://doi.org/10.2514/4.861550).
- [55] W. Fehse. *Automated Rendezvous and Docking of Spacecraft*. Cambridge Aerospace Series. Cambridge: Cambridge University Press, 2003. DOI: [10.1017/CBO9780511543388](https://doi.org/10.1017/CBO9780511543388).
- [56] P. K. S. Dennis D. McCarthy. *Time: From Earth Rotation to Atomic Physics*. Wiley-VCH, 2009. ISBN: 3527407804; 9783527407804.
- [57] K. Wakker. *Fundamentals of Astrodynamics*. Jan. 2015. ISBN: 978-94-6186-419-2.
- [58] A. H. Nayfeh. *Perturbation Methods*. Weinheim, Germany: Wiley-VCH, 2004.
- [59] W. M. Kaula. *Theory of Satellite Geodesy*. Mineola, New York: Dover Publications, 2013.
- [60] F. Tisserand. *Traité de Mécanique Céleste*. Vol. 1. Paris, 1889.

- [61] J. Sullivan, S. Grimberg, and S. D'Amico. "Comprehensive Survey and Assessment of Spacecraft Relative Motion Dynamics Models". In: *Journal of Guidance, Control & Dynamics* 40.8 (2017), pp. 1837–1859. DOI: [10.2514/1.G002309](https://doi.org/10.2514/1.G002309).
- [62] H. Schaub and K. T. Alfriend. "Hybrid Cartesian and Orbit Element Feedback Law for Formation Flying Spacecraft". In: *Journal of Guidance, Control & Dynamics* 25.2 (2002), pp. 387–393. DOI: [10.2514/2.4893](https://doi.org/10.2514/2.4893).
- [63] N. Capitaine. "The Celestial Pole Coordinates". In: *Celestial Mechanics and Dynamical Astronomy* 48 (1990), pp. 127–143.
- [64] D. D. McCarthy. *IERS Conventions (1992)*. 21. Paris, France: Central Bureau of IERS - Observatoire de Paris, 1996.
- [65] J. Williams. *LVLH Transformations*. <https://degenerateconic.com/uploads/2015/03/lvlh.pdf>. 2014.
- [66] H. Fiedler. *Analysis of TerraSAR-L Cartwheel Constellations*. <https://elib.dlr.de/22345/>. Oberpfaffenhofen, Germany: Deutsches Zentrum für Luft- und Raumfahrt (DLR), Nov. 2003.
- [67] G. W. Hill. "Researches in the Lunar Theory". In: *American Journal of Mathematics* 1.2 (1878), pp. 129–147. DOI: [10.2307/2369304](https://doi.org/10.2307/2369304).
- [68] W. H. Clohessy and R. S. Wiltshire. "Terminal Guidance System for Satellite Rendezvous". In: *Journal of the Aerospace Sciences* 27.9 (1960), pp. 653–658. DOI: [10.2514/8.8704](https://doi.org/10.2514/8.8704).
- [69] R. Broucke. "On the Matrizant of the Two-Body Problem". In: *Astronomy and Astrophysics* 6 (June 1970), p. 173.
- [70] J. Tschauner and P. Hempel. "Optimale Beschleunigungsprogramme für das Rendezvous-Manöver". In: *Astronautica Acta* 10 (1964), pp. 296–307.
- [71] T. Carter. "State Transition Matrices for Terminal Rendezvous Studies: Brief Survey and New Example". In: *Journal of Guidance Control and Dynamics* 21 (Jan. 1998), pp. 148–155. DOI: [10.2514/2.4211](https://doi.org/10.2514/2.4211).
- [72] O. Montenbruck, M. Kirschner, and S. D'Amico. "E/I-vector separation for safe switching of the GRACE formation". In: *Aerospace Science and Technology* 10 (2006), pp. 628–635. DOI: [10.1016/j.ast.2006.04.001](https://doi.org/10.1016/j.ast.2006.04.001).

- [73] G. Gaias, J.-S. Ardaens, and C. Colombo. “Precise line-of-sight modelling for angles-only relative navigation”. In: *Advances in Space Research* 67.11 (2021). Satellite Constellations and Formation Flying, pp. 3515–3526. DOI: [10.1016/j.asr.2020.05.048](https://doi.org/10.1016/j.asr.2020.05.048).
- [74] G. Gaias, C. Colombo, and M. Lara. “Analytical Framework for Precise Relative Motion in Low Earth Orbits”. In: *Journal of Guidance, Control, and Dynamics* 43.5 (2020), pp. 915–927. DOI: [10.2514/1.G004716](https://doi.org/10.2514/1.G004716).
- [75] D. Brouwer. “Solution of the problem of artificial satellite theory without drag”. In: *Astronomical Journal* 64.5 (Nov. 1959), p. 378. DOI: [10.1086/107958](https://doi.org/10.1086/107958).
- [76] R. H. Lyddane. “Small eccentricities or inclinations in the Brouwer theory of the artificial satellite”. In: *Astronomical Journal* 68 (Oct. 1963), p. 555. DOI: [10.1086/109179](https://doi.org/10.1086/109179).
- [77] A. Deprit. “Canonical transformations depending on a small parameter”. In: *Celestial Mechanics* 1.1 (Mar. 1969), pp. 12–30. DOI: [10.1007/BF01230629](https://doi.org/10.1007/BF01230629).
- [78] A. Deprit. “Delaunay Normalisations”. In: *Celestial Mechanics* 26.1 (Jan. 1982), pp. 9–21. DOI: [10.1007/BF01233178](https://doi.org/10.1007/BF01233178).
- [79] G. Hori. “Theory of General Perturbation with Unspecified Canonical Variable”. In: *Publications of the Astronomical Society of Japan* 18 (Jan. 1966), pp. 287–296.
- [80] Y. Chihabi and S. Ulrich. “Spacecraft Formation Guidance Law using a State Transition Matrix With Gravitational, Drag and Third-Body Perturbations”. In: Jan. 2020. DOI: [10.2514/6.2020-1460](https://doi.org/10.2514/6.2020-1460).
- [81] G. Gaias, J. Ardaens, and O. Montenbruck. “Model of J2 Perturbed Satellite Relative Motion with Time-Varying Differential Drag”. In: *Celestial Mechanics and Dynamical Astronomy* (2015).
- [82] A. Koenig, T. Guffanti, and S. D’Amico. “New State Transition Matrices for Relative Motion of Spacecraft Formations in Perturbed Orbits”. In: Sept. 2016. DOI: [10.2514/6.2016-5635](https://doi.org/10.2514/6.2016-5635).
- [83] A. Biria and R. Russell. “A Satellite Relative Motion Model Including J2 and J3 via Vinti’s Intermediary”. In: Feb. 2016.
- [84] K. Alfriend and H. Yan. “An Orbital Elements Based Approach to the Nonlinear Formation Flying Problem”. In: Toulouse, France, Feb. 2016.

- [85] Mathworks. *Convert complex diagonal form into real diagonal form*. 2022. URL: <https://www.mathworks.com/help/matlab/ref/cdf2rdf.html>.
- [86] M. R. Delgado. *Lecture notes: Basics of Orbital Mechanics I*. Apr. 2008.
- [87] F. G. Nievinski. *subtightplot*. <https://www.mathworks.com/matlabcentral/fileexchange/39664-subtightplot>. 2013.
- [88] J. C. Lansey. *linspecer*. <https://www.mathworks.com/matlabcentral/fileexchange/42673-beautiful-and-distinguishable-line-colors-colormap>. 2015.
- [89] Jan. *WindowAPI*. <https://www.mathworks.com/matlabcentral/fileexchange/31437-windowapi>. 2013.
- [90] T. Davis. *Arrow3*. <https://www.mathworks.com/matlabcentral/fileexchange/14056-arrow3>. 2022.
- [91] E. Duenisch. *latexTable*. <https://www.mathworks.com/matlabcentral/fileexchange/44274-latextable>. 2016.